



## International Scientific-Technical and Production Journal

«The Paton Welding Journal» is a journal for a wide range of experts from around the world in the field of welding and related technologies

### EDITORIAL BOARD

E.O. Paton Electric Welding Institute, Kyiv, Ukraine:

**I.V. Krivtsun** (*Editor-in-Chief*),

**S.V. Akhonin** (*Deputy Editor-in-Chief*),

**L.M. Lobanov** (*Deputy Editor-in-Chief*),

**O.M. Berdnikova, V.V. Knysh, V.M. Korzhuk,**

**Yu.M. Lankin, S.Yu. Maksimov, M.O. Pashchin,**

**V.D. Poznyakov, I.O. Ryabtsev,**

**V.V. Dmitrik, NTUU**

«Kharkiv Polytechnic Institute», Kharkiv, Ukraine;

**V.V. Kvasnitsky, NTUU**

«Igor Sikorsky Kyiv Polytechnic Institute»,

Kyiv, Ukraine;

**V.M. Uchanin, Karpenko Physico-Mechanical Institute,**

Lviv, Ukraine;

**Chunlin Dong, China-Ukraine Institute of Welding**

of Guangdong Academy of Sciences, P.R. China;

**A. Gumenyuk, Bundesanstalt für Materialforschung**

und –prüfung (BAM), Berlin, Germany;

**U. Reisgen, Welding and Joining Institute,**

Aachen, Germany

#### Founders

E.O. Paton Electric Welding Institute

International Association «Welding» (Publisher)

LLC «Scientific Journals»

*Translator:* I.M. Kutianova

*Editor:* N.G. Khomenko

*Electron galley:* D.I. Sereda, T.Yu. Snegiryova

#### Address

E.O. Paton Electric Welding Institute,

International Association «Welding»

11 Kazymyr Malevych Str. (former Bozhenko),

03150, Kyiv, Ukraine

Tel./Fax: (38044) 200 82 77

E-mail: journal@paton.kiev.ua;

<https://patonpublishinghouse.com/eng/journals/tpwj>

State Registration Certificate

24933-14873 PP from 13.08.2021

ISSN 0957-798X

DOI: <http://dx.doi.org/10.37434/tpwj>

#### Subscriptions

12 issues per year, back issues available.

\$384, subscriptions for the printed (hard copy) version,

air postage and packaging included.

\$312, subscriptions for the electronic version

(sending issues of Journal in pdf format

or providing access to IP addresses).

Institutions with current subscriptions on printed version

can purchase online access to the electronic versions

of any back issues that they have not subscribed to.

Issues of the Journal (more than two years old)

are available at a substantially reduced price.

All rights reserved.

This publication and each of the articles contained

herein are protected by copyright.

Permission to reproduce material contained in this

journal must be obtained in writing from the Publisher.

© E.O. Paton Electric Welding Institute of NASU, 2021

© International Association «Welding», 2021

© LLC «Scientific Journals», 2021

### CONTENTS

#### METALLURGY AND TECHNOLOGY OF WELDING AND SURFACING

*Babinets A.A. and Ryabtsev I.O.* Classification of methods of modification and microalloying of deposited metal (Review) ..... 2

*Maksymov S. Yu., Radzievska A.A., Vasyliiev D.V. and Fadeeva G.V.* Problems of wet underwater welding of duplex steels ..... 9

#### SOLID PHASE WELDING

*Poklyatskyi A.G., Motrunich S.I., Klochkov I.M. and Labur T.M.* Some advantages of welded joints of aluminium 1201 alloy produced by friction stir welding ..... 15

#### FRACTURE MECHANICS

*Dyadin V.P., Davydov Ye.O. and Dmytrienko R.I.* Influence of deformations from static loads on impact and fracture toughness of cylindrical shells ..... 20

#### MODELING OF PROCESSES

*Hubatyuk R.S., Rymar S.V., Prokofiev O.S., Kostin V.A., Didkovskiy O.V. and Antipin E.V.* Modeling of the process of induction heat treatment of welded joints from rail high-strength steels ..... 27

#### WELDING EQUIPMENT

*Korotynskiy O. Ye. and Skopyuk M.I.* Use of capacitive energy storages to create high-efficient multistation welding systems ..... 39

#### GENERAL PROBLEMS OF METALLURGY

*Gasik M.M. and Gasik M.I.* Chemical equilibrium in Fe–O–H system at high temperatures ..... 44

#### NONDESTRUCTIVE TESTING

*Vertiy O.O. and Uchanin V.M.* Three-dimensional visualization of the detected defects by eddy current computing tomography ..... 49

#### NEWS

Inverview with A.I. Panfilov, President of Apis Holding LLC ..... 56

The content of the journal includes articles received from authors from around the world and selectively includes translations into English of articles from the following journals, published by PWI in Ukrainianian:

- Automatic Welding (<https://patonpublishinghouse.com/eng/journals/as>);
- Technical Diagnostics & Nondestructive Testing (<https://patonpublishinghouse.com/eng/journals/tdnk>);
- Electrometallurgy Today (<https://patonpublishinghouse.com/eng/journals/sem>).

# CLASSIFICATION OF METHODS OF MODIFICATION AND MICROALLOYING OF DEPOSITED METAL (Review)

**A.A. Babinets and I.O. Ryabtsev**

E.O. Paton Electric Welding Institute of the NAS of Ukraine

11 Kazymyr Malevych Str., 03150, Kyiv, Ukraine. E-mail: [office@paton.kiev.ua](mailto:office@paton.kiev.ua)

A literature review of the main methods of modification and microalloying of deposited metal was made. It was shown that, in contrast to the «microalloying» term, the «modification» term should mean not only a method of introducing small additives of chemical elements or their compounds into the deposited metal but also various physical effects or technological processes aimed at achieving the same goal – refinement of micro- and macrostructure of metal, cleaning of grain boundaries and near-boundary zones, improving the complex of technological, mechanical and operational properties of steels and alloys. Examples of such physical effects are application of vibrations to a product in the process of surfacing; input of energy from a pulsed heat source; pulsed electrode or filler wire feed; application of sources with modulation of welding current; external electromagnetic effect, etc. The classification of modification methods, depending on the scheme of their implementation and impact on the properties of the deposited metal is given. The main advantages and disadvantages of methods of introducing modifying and microalloying additives into the deposited metal are shown. It was determined that from the considered methods of modification, the chemical method is the simplest and the most rational, which implies introducing modifiers into the deposited metal directly through the charge of flux-cored electrode wires. This method is technologically and economically simple and versatile, and can be used with minor changes in electric arc, electroslog and plasma surfacing. 33 Ref., 1 Table, 3 Figures.

*Keywords:* arc surfacing, deposited metal, flux-cored wire, modification, microalloying, metal structure, service properties

It is well-known that «microcontent» of chemical elements or their compounds in the metal or alloy can significantly influence the nature of metal solidification, shape and composition of nonmetallic inclusions, structure of grain boundaries and near-boundary regions, weldability, hardenability, thermal and wear resistance, etc., i.e. a whole range of technological and service properties [1].

One of the technologically and economically effective methods of controlling the metal «microcontent» at electric arc surfacing is its modification and microalloying. Investigation of this problem is rather widely described in literature as regards modification of steels and alloys, produced by casting methods, as well as welds. At the same time, information on application of different methods of modification and microalloying at surfacing is rather scattered. Therefore, the objective of this work, which consists in analysis of the main methods of modification and microalloying, which can be applied at different surfacing processes, as well as their main advantages and disadvantages, apparently, is quite urgent.

Despite the fact that the «modification» and «microalloying» terms often mean similar processes, which consist in addition of small amounts of certain elements to the metal, which change the metal structure and properties, this idea is not entirely accurate [2].

The process of metal modification has been known for a rather long time. In keeping with the data of [3], this process was first used to obtain high-quality cast iron with application of silicocalcium and ferrosilicon as modifiers. At the same time, there exist several thoughts at present about what exactly should be understood by «modification» term. So, in keeping with [2, 4], modification is a process of active regulation of initial crystallization and/or change of the degree of dispersity of the crystallizing phases, by adding to the melt small amounts of individual elements or their compounds. In work [5], modification means something more, namely any technological process of producing alloys with a fine-grained structure with the purpose of improving their mechanical, technological and service properties. By such processes the authors mean any chemical or physical methods of influencing the structure and properties of metals or alloys, namely addition of modifiers; application of different physical impacts (vibration, ultrasonic or electromagnetic stirring) or a combination of the above.

Unlike modification, microalloying is usually understood as a method of adding individual elements or their compounds with not higher than 0.1 % residual content, which make a significant impact on the processes running in the solid phase (on phase composition of the alloys, size of secondary austenitic grains, structure

and purity of the boundaries and near-boundary zones, etc.) [4]. In the opinion of the author of work [2], the «microalloying» term often includes the modification and deoxidation processes, differing by the mechanism of their impact on the structure and properties of steel and alloys. The role of small additives at microalloying is manifested predominantly as a result of their influence on the metal solid state (formation of interstitial or substitutional solid solution; sizes of secondary grains; dispersity, shape and distribution of nonmetallic inclusions; boundary structure and fine structure of the grains; lowering the negative impact of impurities, etc.).

Thus, the «modification» term should be understood as a totality of any chemical, physical or complex processes influencing the final structure and properties of the metal (alloy). The term «microalloying» means the method of influencing the structure and properties of the metal (alloy) only due to adding to its composition small amounts ( $\leq 0.1\%$ ) of elements or their compounds, which have a considerable influence on the processes running in the solid phase.

**Classification of the modification methods.** The methods of modification of the deposited metal can be divided into three main groups: chemical (adding modifiers); physical (application of external physical impact) and combined ones.

**1. Chemical methods of modification.** In this case a certain amount of chemical elements or their compounds are added to the deposited metal to achieve favourable changes of the metal structure and properties. Depending on their impact, the modifiers can be divided into four classes [5, 6]:

- modifiers of the 1<sup>st</sup> kind that improve wettability of one component of the alloy by another one, i.e. which lower the surface tension on their interface, and thus facilitate formation of the solid phase contacting the liquid one;

- modifiers of the 2<sup>nd</sup> kind that are the direct crystallization centers. They, however, can be so rather conditionally in the case when the melt temperature is so close to that of modifier solidification that it will be insufficient for melting of the modifiers added to the pool;

- modifiers of the 3<sup>rd</sup> kind (inoculators) that change the structure due to reduction of overheating of the crystallizing liquid metal. Higher cooling rate promotes increase of the crystallization rate and reduction of development of the liquation processes that is favorable for the structure;

- complex modifiers, which are a complex of two and more modifiers from one or different element classes from those given above. Depending on their type, the impact of such modifiers is usually manifested in a more intensive and complex manner, simultaneously affecting the mechanical, technological and service properties of the metal.

It should be also noted that the nature of action of modifiers of the 1<sup>st</sup> kind can change at formation

of modifier chemical compounds with other elements. The new chemical compound will in the long run have the role of an independent modifier already of the 2<sup>nd</sup> kind. These compounds can be surface-active under some conditions, and under other conditions they can be inactive, contrarily. So, for instance, boron, which usually is a modifier of the 1<sup>st</sup> kind, can form a more stable chemical compound with iron — FeB<sub>2</sub>, which is the crystallization center as a modifier of the 2<sup>nd</sup> kind [5]. The names of some chemical elements, or their compounds, which are often used for modification and microalloying, as well as their main physical properties are given in the Table [7, 8].

*1.1. Modifiers of the 1<sup>st</sup> kind.* Modifiers of such a type include additives, unlimitedly soluble in the liquid phase and slightly soluble in the solid phase (0.001–0.1 %). In their turn, these additives can be divided into two types: those, which do not change the surface properties of the crystallizing phase — «a», and those, which change the surface tension on melt-crystal interface — «b». Soluble impurities of type «a» can slow down the growth of the solid phase only due to the concentration barrier on the crystal-melt interface with no change taking place in the process energy characteristics [5].

Additives of «b» type are usually called surface-active. They selectively concentrate on the surface of

Physical properties of modifying chemical elements (compounds) [7, 8]

Modifier	Melting temperature, K	Boiling temperature, K	Density, g/cm <sup>3</sup>
Mg	923	1363	1.738
Ba	1002	2170	3.500
Sr	1042	1657	2.540
Ce	1071	3740	6.757
Ca	1115	1757	1.550
La	1194	3730	6.150
Pr	1204	3785	6.773
Y	1795	3611	4.470
SiO <sub>2</sub>	1983	2503	2.650
Zr	2125	4650	6.506
Al <sub>2</sub> O <sub>3</sub>	2345	3250	3.950
B	2349	4200	2.340
SiC	3003	3103	3.210
VC	3083	4173	5.770
WC	3143	6273	15.630
TiN	3203	N/D	5.400
ZrN	3253	Same	7.090
TiCN	3400	»	5.120
TiC	3533	4573	4.930
NbC	3763	4573	7.820
ZrC	3805	5373	6.730

crystals (dendrites). The surface-active substances can create a continuous adsorption layer. It means that with practical absence of solubility of the surface-active modifiers in the solid phase, a shell of the liquid enriched in modifiers forms around it [5].

Addition of modifiers of the 1<sup>st</sup> kind is accompanied by the change of surface tension and activation energy in opposite directions. It complicates their overall impact on crystallization and grain size. Macrograin refinement is the most characteristic effect for modifiers of the first kind. As increase of activation energy through additive adsorption on crystal faces promotes lowering of crystal growth rate, it causes coarsening of the grain dendrite structure. Thus, under the impact of modifiers of the 1<sup>st</sup> kind the macrograin is refined, but the micrograin is coarsened at the same time, i.e. an integrated impact on the macro- and microstructure is manifested [5].

*1.2. Modifiers of the 2<sup>nd</sup> kind.* Parameters of crystallization and macrostructure can be affected by hard particles added to the melt. Here, a number of researchers associate this influence exactly with the contact action on the process of nucleation of crystallization centers. It is accounted for by the fact that introduction to the melt of an insoluble additive with properties close to those of the crystallizing liquid, a significant lowering of the melt metastability range takes place. Such additives are called isomorphous with the crystallizing liquid, they have the crystalline lattice parameters close to those of this liquid, and it is believed that, similar to modifiers of the 1<sup>st</sup> kind, they ensure macrograin refinement. The content of this type of modifiers is usually limited to 0.1 % [5].

Proceeding from generalization of different works, the following conditions were formulated for selection of insoluble particles with the greatest modifying ability at surfacing [5]: use of refractory insoluble compounds; use of disperse particles with the large total interface; it is desirable for the particles to have metal properties (by the type of chemical bond); the most effective are particles of stable chemical compounds, which will form in the weld pool, as a result of interaction with one of the components or the alloy base.

*1.3. Modifiers of the 3<sup>rd</sup> kind (inoculators).* In order to increase the quality of the deposited metal at surfacing and welding, specially prepared powders of micro- and nanosized particles from refractory compounds of different elements are often used. When added to the weld pool, they are evenly distributed in the liquid metal volume and act as effective centers of metal pool crystallization. In keeping with the data of [5], addition of inoculants to the crystallizing melt, ensures an increase of homogeneity and dispersity of the cast structure, optimization of the shape and distribution of the nonmetallic inclusions, and reduction of the quantity of some defects that essentially increases the level and isotropy of the metal properties.

However, despite improvement of the macrostructure, application, for instance, of metal powder, cast shot and other similar additives as inoculators at electroslag surfacing can lead to greater contamination of steel by nonmetallic inclusions, mainly oxides. This is related to insufficiently mastered technology of introducing the inoculators, complexity of producing and storing them, as they require protection from oxidation during storage, transportation and addition to the liquid pool [5].

*1.4. Complex modifiers.* The main advantage of application of complex additives-modifiers is the fact that simultaneous action of two and more modifiers enhances the effect obtained at application of one modifier. This is related to the above process of crystallization center nucleation on insoluble impurities in the layer of the liquid phase with diffusion overcooling, due to addition of a soluble additive (especially surface-active) [5]. There are three types of complex modifiers: refining; strengthening and refining-strengthening. A feature of steel modification by complex modifiers is the fact that parallel to structure refinement, the nature and shape of nonmetallic inclusions also changes, level of grain boundary contamination by nonmetallic inclusions decreases, uniformity of distribution of structural components becomes higher, etc. [5].

**2. Physical methods of modification.** The main methods applied at surfacing, which can be regarded as this type of modification, and are aimed at metal structure refinement, are rather well known and covered in technical literature. This is, in particular, application of vibrations to the product during surfacing; input of energy from a pulsed heat source; pulsed feed of electrode or filler wire; application of sources with welding current modulation, and in a number of cases addition of separate heat sources which affect the HAZ near the line of the weld (deposited bead); external electromagnetic impact, etc. It is not rational to conduct a detailed review of each of the above-mentioned methods in this paper, so we will briefly focus on several processes, which allow making a rather significant influence on the structural state of steels and alloys and on their properties, respectively, and which can be used at surfacing.

*2.1. Low-frequency vibrations and mechanical stirring of the liquid pool.* Vibration is a method of forced mixing of the liquid pool. Vibration frequency usually is 1–30 Hz at variable amplitude, resulting in breaking up of large dendrites during solidification. Their fragments promote nucleation of new crystallization centers, leading to microstructure refinement and intensification of the processes of liquid pool degassing [9, 10].

*2.2. Electromagnetic stirring.* This method first became applied at continuous pouring of steel ingots, and then it began to be used in welding and surfacing. This method ensures breaking up of dendrites on the crystallization front and distribution of their fragments over the entire liquid pool volume, leads to lowering

and leveling of temperature in the pool volume and widening of the region of overcooled liquid metal. The number of crystallization centers grows in direct dependence on power, applied to the inductor, and, hence, on the speed of liquid phase movement [11, 12].

One of the examples of application of electromagnetic stirring is use of current-conducting mould (CCM) at electroslag surfacing [13]. In this case, slag pool rotation in the horizontal plane takes place in the mould, which is due to interaction of magnetic fields of the slag pool and the current-conducting section of the mould. Slag pool rotation leads to that the filler material particles fed into the slag pool, melt completely and the metal is better refined. In addition, pool rotation ensures a more fine-grained structure of the deposited metal.

**2.3. Ultrasonic treatment.** This method envisages an impact of high-frequency mechanical vibrations on the liquid pool. An alternating pressure is applied to the liquid, resulting in its rupture with formation of fine voids – ultrasonic cavitation. It may lead to breaking up of primary dendrites and phase components. Its fragmentation and even distribution of the fragments create additional crystallization centers and lead to macrograin refinement. The grain size decreases with increase of power applied to the pool, particularly after the cavitation threshold has been reached [14]. By some data [5], unlike electromagnetic stirring, at ultrasonic treatment not only volume crystallization and the associated undesirable phenomena do not develop, but, contrarily, the size of dendrite clusters decreases with grain refinement, as a result of shortening of the transition zone.

**3. Combined modification methods.** In this case, chemical additives-modifiers are applied simultaneously with physical impact and technological measures. It leads to enhancement of the effect of the modifiers and enables producing superfine and special structures. For instance, at addition of surface-active modifiers and application of ultrasonic treatment, the latter affects the nucleation energy in such a way that the modifying additive more is uniformly adsorbed on the nuclei of subcritical size and improves their resistance [15]. Selection of a rational method of physical impact and of the modifier in each specific case should be performed, proceeding from the objective of physical impact (increase of mechanical, technological, and service properties of the manufactured end products), as well as practical realization and cost-effectiveness of the method of impact.

**Technologies of adding modifiers at chemical modification processes.** At present exactly chemical methods of modification of the deposited metal and weld structure are quite widely used for surfacing and welding processes by adding powders of refractory chemical compounds to the weld pool. It ensures refinement of the metal structure and formation of new strengthening phases that promotes improvement of the metal service properties [16].

There exist a rather large number of methods of modifier addition to the weld pool: through electrode or filler flux-cored wires and strips; electrode coating; solid or flux-cored filler rods and wires, which are placed directly into the gap in welding; ceramic flux, etc.

Here, a partially unsolved problem still is preservation of ultradisperse particles in the weld pool, which actively dissociate during surfacing, as addition of modifiers directly into the weld pool through the flux or electrode wire is less effective than at casting, because of high temperature in the welding zone [17]. It is already widely known that the temperature in the arc column, through which the molten metal drop passes, may reach 5000–6000 K, the temperature of the drop proper reaching 2300–2700 K. Therefore, one of the methods to increase the effectiveness of deposited metal modification at arc surfacing is application of elements and compounds having a high melting temperature (2700 K) as modifiers.

Let us consider the main known methods of adding modifiers to the deposited metal, as well as their advantages and disadvantages.

**1. Addition of modifiers contained in flux-cored wire charge, directly through the arc.** Despite the above-mentioned disadvantages of the process of metal modification at passage of modifier additives directly through the welding arc, such a method is quite often applied, due to its relative simplicity and availability.

So, in [18] a complex master alloy was developed, which contains yttrium, cerium and rare-earth elements, and which was successfully applied in the charge of self-shielding flux-cored wires PP-AN155 and PP-AN156 for surfacing tools for hot deformation of metal (different forming and mill rolls, hot cutters, etc.) and flux-cored wire PP-AN163 for submerged-arc surfacing of propeller shafts and other parts. As shown by production testing, modification and microalloying of the deposited metal allowed increasing the tool resistance by 20–30 %.

In work [19] metal modification to improve its wear resistance was performed with success by adding potassium fluorozirconate to flux-cored wire charge. Steel modification by zirconium by adding to electrode wire composition powders of ferroalloy of Fe–Si–Zr alloying system was also applied with success in [20].

In the opinion of the authors of [21], when boron is used as modifier, its addition to the charge of flux-cored electrode wires looks the most promising, as application of solid wire requires increase of its boron and titanium content, which results in increase of the wire hardness and rigidity. Addition of boron microadditives to the deposited metal through the flux seems to be insufficiently reliable, because of low metallurgical activity of boron.

In works [22, 23] deposited metal modification was performed by adding to the charge flux-cored

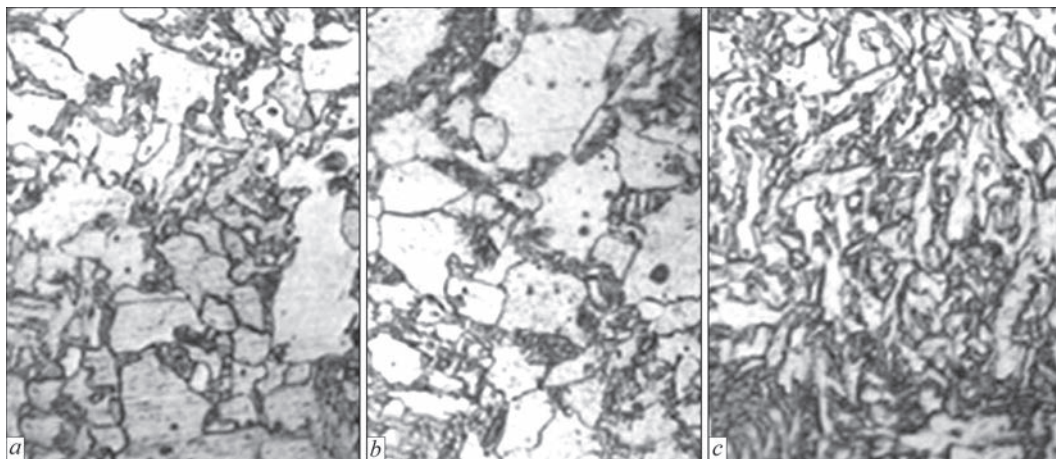


**Figure 1.** Microstructure ( $\times 400$ ) of the metal of welds made [17]: *a* — without modifier addition; *b* — with  $\text{TiO}_2$  addition,  $d_{av} = 8 \mu\text{m}$ ; *c* — with  $\text{TiO}_2$  addition,  $d_{av} = 4 \mu\text{m}$

electrode wires of titanium and tungsten carbide and boron nitride powders. In these cases, so-called microcoolers were used (see below), in order to enhance the modification effect.

As we can see, despite the negative influence of high temperatures in the arc gap, the method of modification by introducing modifiers into the charge of flux-cored electrode wires is quite successfully used. By the data of [24], the sizes of disperse particles of the refractory compounds should be equal to 50–300  $\mu\text{m}$ , in order to achieve a more tangible effect from addition of modifiers to the weld pool through the flux-cored wire charge. More over, in the opinion of the authors of [25], in order to guarantee the transition of modifier components from electrode materials into the deposited metal, such processes should be used, in which a low-power and short-term thermal cycle is realized and a weld of a small volume forms.

**2. Application of «microcoolers».** In order to reduce overheating and melting of modifying additives, penetrating into the arc zone, in work [22] it was proposed to apply the additives-modifiers in a mixture with cold macroparticles (microcoolers) from wire chips of  $2 \times 2 \text{ mm}$  size, which are fed into the mixture with modifiers in the form of filler material.

The same idea was realized in several works at nano-modification of welds [6], and deposited metal [26]. In order to preserve the activity of modifying nanoparticles and to ensure their attachment to macroparticles that have the role of microcoolers, mechanochemical treatment of the powder mixture of macro- and nanoparticles was performed in high-energy planetary mills. In particular, in work [26] nickel-based composite microgranules, containing nanoparticles (up to 100 nm size) of titanium carbonitride, were added to the charge of experimental flux-cored wires as a modifier.

More over, in keeping with the data of works [3, 17], reduction of the dimensions of additives-modifiers to the nanoscale allows improving their effectiveness. The smaller the sizes of the modifying particles,

and, hence, of the crystallization centers, the smaller is the weld metal grain, and the smaller are the stress intensity factors. Refinement of modifier particles increases the specific energy of the colliding particles and the probability of chemical interaction between them with formation of strong ties and more effective refinement of the metal structure (Figure 1).

**3. Application of additional electrode or filler wire.** The effectiveness of metal modification can be increased by introducing modifying additives to the low-temperature zone of the pool in the composition of additional electrode or filler flux-cored wire. Here, it is rational to use one flux-cored wire in multiarc welding (surfacing) process to change the produced joint quality characteristics [27].

So, in [16] it was demonstrated that metal modification was quite successfully performed using flux-cored filler wire, which consisted of low-carbon steel sheath and filler, containing granulated powder from nano- and microparticles of titanium nitride.

In work [28] a comparison was made of the results of titanium modification at two schemes of its addition in submerged-arc welding: standard, through the flux-cored wire charge through the arc column and with direct introduction of additional filler wire into the «cold» part of the weld pool. Investigations showed that as titanium is an effective deoxidizer, the probability of its oxidation is the highest in the arc column and in the drop, as well as in slag deoxidation reactions. Therefore, at titanium addition directly through the charge of flux-cored electrode wire a reduction of its content in the weld by 3.5 times was noted compared its content in the flux-cored wire. However, at application of wire of identical composition, but as a filler, titanium content in the weld decreased only by 1.3 times.

At the same time, application of additional filler wires and strips for deposited metal modification can be complicated by a number of factors. Introduction of electrode wires in front of the main electrode, as well as at a small distance from it, similar to addition-

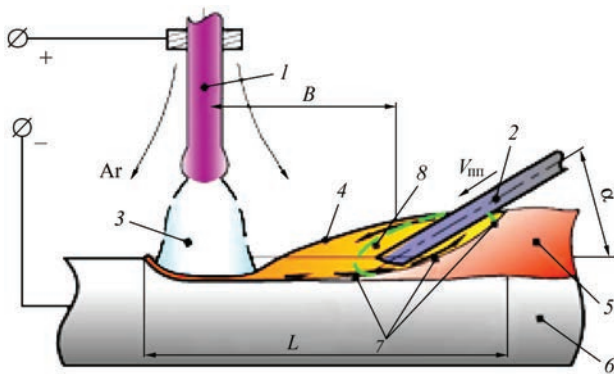


**Figure 2.** Scheme of adding modified flux-cored filler wire to the weld pool during electric arc surfacing [16]: 1, 2 — electrode and filler flux-cored wires; 3 — electric arc; 4 — weld pool; 5, 6 — deposited and base metals; 7 — deposited metal solidification front; 8 — overcooled zone of metal melt

al heating of the welding wire by current, still leads to considerable losses of the modifier, because of its melting and dissolution in the overheated melt. Application of electroneutral filler wire significantly limits its feed rate, exceeding which causes wire welding to the pool bottom, while application of several wires leads to pool overcooling and violation of the quality of deposited metal layer formation (Figure 2) [16].

In order to solve this problem, a comprehensive experimental study was performed in work [16], to determine the optimal parameters of introducing additional filler modifying wire into the weld pool: angle of inclination, feed rate, distance from electrode wire to filler wire edge, etc. Such an approach, however, requires considerable time and costs and needs to be improved.

Thus, the method of deposited metal modification through additional filler wire, fed into the weld pool tail part, allows increasing the content of modifiers in the deposited metal. At the same time, this method is complicated in terms of technology, involving considerable difficulties of ensuring a stable arc process and high quality of deposited metal formation and homogeneity of its structure.

**4. Application of additional fillers, placed directly on the workpiece, being welded or surfaced.** A method of laying filler rods or wires directly into the groove at welding is sometimes used to reduce the modifier losses. So, in [29, 30] cast rods or consumable electrodes of a specified length and diameter were used for weld modification, which were placed into the groove along the butt length directly before welding.

This method was upgraded in work [31], and a two-arc welding process was used for melting the modified master alloy and additional mixing of the weld pool. Such a schematic allows avoiding direct impact of the arc on modifying additives and shields them by a liquid interlayer (Figure 3).

In work [32] modifying additives (disperse powders of silicon carbide and aerosil) were used, which were located in a layer of alloying charge, applied di-

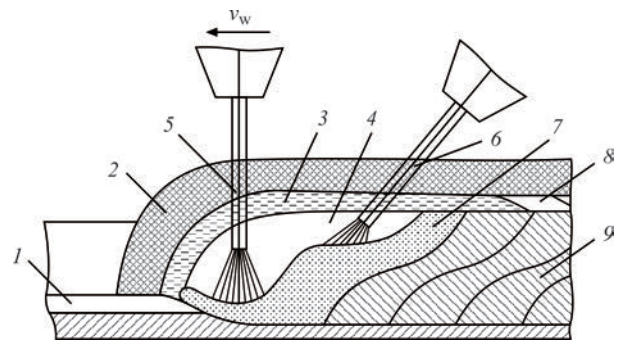


**Figure 3.** Scheme of two-wire submerged-arc welding with application of modified master alloy [31]: 1 — master alloy; 2 — flux; 3 — liquid slag; 4 — gas bubble; 5, 6 — electrode wires; 7 — liquid pool; 8 — solidified slag; 9 — weld metal

rectly on the processed surface. However, this method has a significant disadvantage: at its application sound formation of the deposited metal can be achieved only in a narrow range of surfacing modes. In order to solve this problem, the authors of [33] suggested additional superposition of an external magnetic field. Such an approach, however, complicates the surfacing process even more in terms of technology.

As we can see, the above-listed deposition methods allow in a certain way avoiding direct impact of the welding arc on modified filler wires or rods. They, however, are technologically quite complicated, and often cannot be applied for surfacing.

Thus, the simplest and most rational of the above-described methods is addition of modifiers directly through the charge of flux-cored electrode wires. This method is quite versatile and can be used with certain modifications at different electric arc, electroslag, plasma and other surfacing processes.

## Conclusions

1. Distinction between the terms «modification» and «microalloying» should be made. Modification is a set of any chemical or physical processes influencing the final structure and properties of metal (alloy), while microalloying is a method of influencing the structure and properties of the metal (alloy) only due to introducing into its composition small additives ( $\leq 0.1\%$ ) of elements or their compounds, having a significant impact on the processes running in the solid phase.

2. Modification and microalloying of steels and alloys are mostly used for refining their micro- and macrostructure; reduction of chemical, physical and structural inhomogeneity; favourable changes in the nature and shape of nonmetallic inclusions; enhancement of the set of technological, mechanical and service properties of steels.

3. In terms of technology and economy, the simplest and most rational method of metal modification at surfacing is addition of modifiers directly through the charge of flux-cored electrode wires. In order to increase the modification effectiveness in this case, it

is recommended to use modifiers with melting temperature above 2700 K and (or) additionally use special particles-microcoolers.

1. Manyak, N.A., Manyak, L.K. (2002) Influence of boron on structure and toughness of low-alloy steel. *Metall i Lityo Ukrainy*, **5–6**, 23–25 [in Russian].
2. Lyakishev, N.P. (2000) *Thesaurus on metallurgy*. Moscow, Internet Engineering [in Russian].
3. Bublikov, V.B. (2008) High-strength cast iron – 60 (Review). *Litejnoe Proizvodstvo*, **11**, 2–8 [in Russian].
4. Goldshtejn, Ya.E., Mizin, V.G. (1986) *Modification and microalloying of cast iron and steel*. Moscow, Metallurgiya [in Russian].
5. Zadiranov, A.N., Kats, A.M. (2008) *Theoretical principles of crystallization of metals and alloys*. Moscow, MGIU [in Russian].
6. Boldyrev, A.M., Grigorash, V.V. (2011) Problems of micro- and nanomodification of welds in welding of building metal structures. *Nanotekhnologii v Stroitelstve*, **3(3)**, 42–52 [in Russian].
7. Zubenko, L.N. (2015) Application of modifiers in composition of functional coatings. *Tekhnologii i Materialy*, **2**, 20–23 [in Russian].
8. Sheksheev, M.A., Mikhailitsyn, S.V., Sychkov, A.B. et al. (2018) Examination of influence of ultradisperse particles of tungsten monocarbide on structure of deposited metal. *Vestnik Yuzhno-Uralsky Gos. Un-ta, Series: Metallurgiya*, **18(4)**, 128–136 [in Russian].
9. Pulka, Ch.V., Shably, O.N., Senchishin, V.S. et al. (2012) Influence of vibration of parts on structure and properties of metal in surfacing. *The Paton Welding J.*, **1**, 23–25.
10. Lashchenko, G.I. (2016) Technological capabilities of vibration treatment of welded structures (Review). *Ibid.*, **7**, 26–31. DOI: <https://doi.org/10.15407/tpwj2016.07.05>
11. Razmyshlyayev, A.D., Ageeva, M.V. (2018) On mechanism of weld metal structure refinement in arc welding under action of magnetic fields (Review). *Ibid.*, **3**, 25–28. DOI: <https://doi.org/10.15407/tpwj2018.03.05>
12. Razmyshlyayev, A.D., Ageeva, M.V., Lavrova, E.V. (2019) Refinement of metal structure in arc surfacing under the effect of longitudinal magnetic field. *Ibid.*, **2**, 19–21. DOI: <https://doi.org/10.15407/tpwj2019.02.02>
13. Ryabtsev, I.A., Kuskov, Yu.M., Pereplyotchikov, E.F., Babynets, A.A. (2021) *Surfacing. Control of base metal penetration and formation of deposited layers*. Ed. by I.A. Ryabtsev. Kiev, Interservice [in Russian].
14. Kirian, V.I., Kajdalov, A.A., Novikova, D.P., Bogajchuk, I.L., Kesners, M. (2007) Improvement of welded joint structure under the impact of wideband ultrasonic vibrations during welding. *The Paton Welding J.*, **2**, 38–40.
15. Morozov, V.P. (2006) Peculiarities of process of primary structures formation of welds of different system aluminium alloys. *Izv. Vuzov, Mashinostroenie*, **9**, 51–64 [in Russian].
16. Antonov, A.A., Artemiev, A.A., Sokolov, G.N. et al. (2016) Development of method of consumable electrode arc surfacing with filler wire. *Sovremennye Problemy Teorii Mashin*, **4(2)**, 99–101 [in Russian].
17. Boldyrev, A.M., Orlov, A.S., Gushchin, D.A. (2016) New technology for producing of granulated filler material with nanomodifying additives for arc welding of steels. *Nanotekhnologii v Stroitelstve*, **8(6)**, 124–143 [in Russian].
18. Gladky, P.V., Mikaelyan, G.S. (2015) Microalloying and modification of wear-resistant deposited metal. In: *Surfacing. Technologies, materials, equipment*. Kiev, PWI [in Russian].
19. Zusin, V.Ya. (2011) Investigation of modification of metal deposited by flux-cored wire with aluminium sheath. *Vestnik Priazov. GTU. Series: Tekhnicheskije Nauki*, **23**, 180–183 [in Russian].
20. Shlepakov, V.N., Gavrilyuk, Yu.A., Naumejko, S.M. (2011) Development of flux-cored wire for arc welding of high-strength steel of bainite class. *The Paton Welding J.*, **11**, 15–18.
21. Fejnberg, L.I., Rybakov, A.A., Alimov, A.N., Rosert, R. (2007) Weld microalloying with titanium and boron in multiarc welding of large diameter gas and oil pipes. *Ibid.*, **5**, 12–16.
22. Litvinenko-Arkov, V.B., Sokolov, G.N., Kyazymov, F.A. (2012) Structure and properties of heat-resistant metal, deposited by flux-cored wires with TiCN nanoparticles. *Izv. Volgo-grad GTU*, **9**, 194–197 [in Russian].
23. Makarov, A.V., Kudryashov, A.E., Vladimirov, A.A., Titova, A.P. (2019) Application of deposited materials modifying with refractory components for restoration of rollers of billet continuous-casting machines. *Vestnik Bryansk GTU*, **8**, 41–48 [in Russian].
24. Golovko, V.V. (2018) Possibilities of nanomodification of dendrite structure of weld metal. *The Paton Welding J.*, **8**, 2–6. DOI: <https://doi.org/10.15407/tpwj2018.08.01>
25. Sokolov, G.N., Zorin, I.V., Artemiev, A.A. et al. (2014) Peculiarities of formation of structure and properties of deposited alloys under influence of refractory compound nanoparticles. *Fizika i Khimiya Obrabotki Materialov*, **2**, 38–47 [in Russian].
26. Sokolov, G.N., Artemiev, A.A., Dubtsov, Yu.N. et al. (2018) Influence of nitrogen and titanium carbonitride particles on structure and properties of Fe–Cr–Ni–Mo system metal deposited by flux-cored wire. *Omskij Nauchnyi Vestnik*, **2**, 15–19 [in Russian].
27. Yakovlev, D.S., Shakhmatov, M.V. (2015) Microalloying of welded joints by flux-cored wire. *Tekhnologii i Materialy*, **2**, 23–28 [in Russian].
28. Yakushin, B.F., Potapov, S.V., Kilyov, V.S. (2015) About direct modification of welding pool in submerged-arc welding. *ESU*, **12–5**, 126–133 [in Russian].
29. Babu, N., Talari, M., Pan, D., Sun, Z., Wei, J., Sivaprasad, K. (2012) Microstructural characterization and grain refinement of AA6082 gas tungsten arc welds by scandium modified fillers. *Materials Chemistry and Physics*, **137/2**, 543–551.
30. Kuznetsov, V.D., Stepanov, D.V. (2015) Structure and properties of weld metal modified by nanooxides. *The Paton Welding J.*, **11**, 10–16. DOI: <https://doi.org/10.15407/tpwj2015.11.01>
31. Alyoshin, N.P., Grigorieva, M.V., Kobernik, N.V. et al. (2018) Modification of weld metal with tungsten carbide nanosized particles in twin-arc submerged-arc welding. *Khimiya Vysokikh Energij*, **52(5)**, 426–431 [in Russian].
32. Peremitko, V.V. (2014) Wear-resistant arc surfacing over the layer of alloying charge. *The Paton Welding J.*, **8**, 54–57. DOI: <https://doi.org/10.15407/tpwj2014.08.09>
33. Peremitko, V.V., Nosov, D.G. (2015) Optimization of modes of submerged arc surfacing over the layer of alloying charge of caterpillar machine running gear parts. *Ibid.*, **5–6**, 44–46. DOI: <https://doi.org/10.15407/tpwj2015.06.10>

Received 21.07.2021

## PROBLEMS OF WET UNDERWATER WELDING OF DUPLEX STEELS

S.Yu. Maksymov, A.A. Radzievska, D.V. Vasyliiev and G.V. Fadeeva

E.O. Paton Electric Welding Institute of the NAS of Ukraine

11 Kazymyr Malevych Str., 03150, Kyiv, Ukraine. E-mail: office@paton.kiev.ua

The article considers the problem of welding duplex steels: state-of-the-art of the problem and prospects for further development. Welds made in air and under water using coated electrodes, are characterized by a similar structure and properties. Intensive cooling provided by the water environment does not increase the content of ferrite in the weld and HAZ as compared to its content in the joints made in the air. Butt joints produced under water at an unstable arc burning are characterized by a tendency to cold crack formation in the weld metal, but in the HAZ cracks were not detected. In the article the analysis of hardness distribution in the studied joints was presented, which did not reveal significant differences between the values determined in the welds made in air and in water. The size of austenitic phases in dry welding was larger than in wet welding under the same conditions of heat input. In wet welding, the share of  $\gamma$ -phase increased significantly at increase in input energy from 27.31 to 39.46 % for the weld center and from 35.01 to 44.9 % for the weld metal adjacent to the fusion line. All the studied variants of chemical composition of the weld metal were insensitive to local corrosion due to high values of PREN. The weld metal adjacent to the fusion line showed optimal resistance to local corrosion, and the weld metal also showed better resistance to local corrosion than did the heat-affected-zone. 17 Ref., 1 Table, 8 Figures.

*Keywords:* duplex steels, underwater welding, welded joint, formation, structure, corrosion, service properties, welding consumables

From the start of 1900s, duplex and superduplex stainless steels have an important role in oil and gas industry, in transportation, construction and processing industry [1]. By now the sphere of their application expanded to metal structures that operate in water environment, in particular, at construction of navy and nuclear power units, pipelines for sulphur trioxide, oil and sea water, due to a favourable combination of high mechanical strength and general and local corrosion resistance and cracking resistance, caused by interaction of stresses and hydrogen, the source of which is the acid environment of liquid hydrocarbons, as well as lower cost due to lower nickel content [2].

Modern duplex stainless steels usually contain 4.5–7.5 % nickel and 20–25 % chromium at a low level of carbon and have a two-phase ferrite-austenite microstructure. As one can see from the diagram of phase transformation of Fe–Cr–Ni system [3] (Figure 1), when Cr/Ni equivalent ratios are higher than 1.75, just the ferrite phase evolves from the liquid up to complete crystallization. During the further cooling process ferrite partially transforms into austenite, when the temperature drops to that of  $\delta \rightarrow \gamma$  transformation, which is determined by the chemical composition. During ferrite transformation into austenite with cooling, the austenite morphology can be consistently manifested in the form of grain-boundary amorphous structures, Widmanstatten

side plates or intragranular side plates, acicular, as well as fine intragranular precipitates [4]. With the start of transformation, austenite first appears on the boundary of the grains due to its maximum free energy. Transformation of intragranular austenite requires the greatest driving force, and takes place at the lowest possible temperature. The temperature of transformation of austenite of Widmanstatten side plate is between two of the above-mentioned temperatures. The degree of transformation and

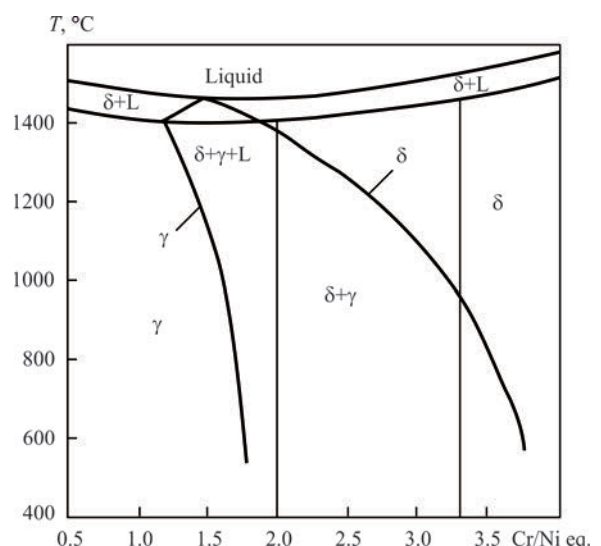


**Figure 1.** Diagram of pseudobinary phase transformation of Fe–Cr–Ni system [3]

S.Yu. Maksymov — <https://orcid.org/0000-0002-5788-0753>

© S.Yu. Maksymov, A.A. Radzievska, D.V. Vasyliiev and G.V. Fadeeva, 2021

final morphology of austenite are determined by chemical composition and cooling rate. The higher the content of austenite stabilizers, the greater is the degree of its transformation. The higher the cooling rate, the more acicular and fine precipitates are present in ferrite.

Mechanical properties and corrosion resistance of duplex steel welded joints depend on ferrite and austenite fraction in the structure, morphology and size of ferrite and austenite grains, type, morphology and distribution of intermetallic phases, which can precipitate from ferrite. Standard duplex and superduplex steels cover a whole range of microstructures, the properties of these alloys depend mainly on the balance of the two phases — ferrite and austenite. Any form of heat treatment, including thermal cycles of welding, influences the morphology of these steels, and, consequently, the mechanical and corrosion properties of the HAZ in welded joints [5]. So, at heating from approximately 600 up to 1000 °C, the superduplex stainless steels are prone to formation of intermetallic phases (for instance,  $\sigma$ -phase,  $\chi$ -phase and R-phase) [6]. Reheating can also cause formation of secondary austenite and nitride precipitation. Presence of these phases considerably impairs the corrosion resistance and impact toughness.

The value of heat input and cooling rate have an essential influence on the microstructure and secondary phase formation in the HAZ. During welding, the HAZ is brought to a temperature, at which the material is practically completely ferritic. Austenite reformation starts at cooling. The degree of ferrite transformation into austenite depends on the steel composition and welding conditions. A higher content of nickel and nitrogen and slower cooling facilitate this transformation. At rapid cooling a high content of ferrite can be recorded in the HAZ, resulting in lowering of the joint strength and corrosion resistance. Ferrite content in the metal of the weld and HAZ should be within 25–70 %, so as to ensure optimum mechanical properties and corrosion resistance [7]. In order to achieve the required balanced microstructure, it is necessary to strictly control the filler metal composition and cooling rate. In the opinion of the authors of work [8], the filler metal composition has a stronger influence on the final ratio of ferrite/austenite than does the

cooling rate. Cold cracking susceptibility in the welded joints of duplex steels depends on ferrite content in their structure, heat input and hydrogen content in the shielding gas. It was noted that it becomes higher, if the ferrite content in the weld is more than 50 %. On the other hand, hydrogen addition to the shielding gas (Ar) led to reduction of cracking. The shape of edge preparation can also promote cold cracking due to unfavourable distribution of residual stresses after welding [9, 10].

Despite the broad application of duplex steels, the effect of water environment on the structure and properties of welded joints is little studied so far. There are no results of extensive research or reports on duplex steels behaviour at underwater welding and properties of the produced joints. The most unfavourable factors for underwater welding of duplex steel are believed to be increased cooling rate and hydrostatic pressure, and there also exists the risk of increased content of hydrogen in the ferritic phase [11, 12]. Here, most of the problems are associated with the HAZ and not with the weld.

At wet welding, the factors affecting the welding quality, are more complex than at dry welding, and the welding process is also more complicated. Most of the accessible results of the conducted experiments have been obtained at application of manual welding with industrial electrode materials, used in air, as specialized electrode materials for wet underwater welding of duplex steels have not been developed so far [13]. Here, the susceptibility to formation of cold cracks and pores, influence of the thermal cycle of welding directly in the water environment on the structure and properties of weld metal were assessed.

So, works [12, 14] give the results of determination of cold cracking resistance of 2205 UNS-S31803 stainless steel, using Tekken sample (1.4462). Welding was performed with Bohler FOX CN 22/9N (EN 1600 – E 22 9 3 N L R 3 2) electrodes of 4 mm diameter at the depth of 0.5 m. Tested samples had undercuts, lacks-of-fusion and incorrect shape. During underwater welding, it was noted that the arc was unstable, leading to sputtering, and uncontrolled increase of welding parameters that exceed the admissible heat input for duplex steels. The results of metallographic investigations revealed internal defects in the weld metal, namely pores and cracks, which formed in the root pass (Figure 2). HAZ was very narrow, and it could not be identified up to  $\times 50$  magnification. Base metal had a typical two-phase structure, which consists of a ferrite matrix (35–50 %) and austenite grains, arranged in bands; average ferrite content was equal to approximately 48 %. The weld structure consisted of precipitates of ferrite and acicular austenite normal to the fusion line (Figure 3, a); ferrite amount was in the range from 52 to 56 %. Difference in ferrite content between the base metal and weld can be the result



Figure 2. Cross-section of an underwater weld [11]

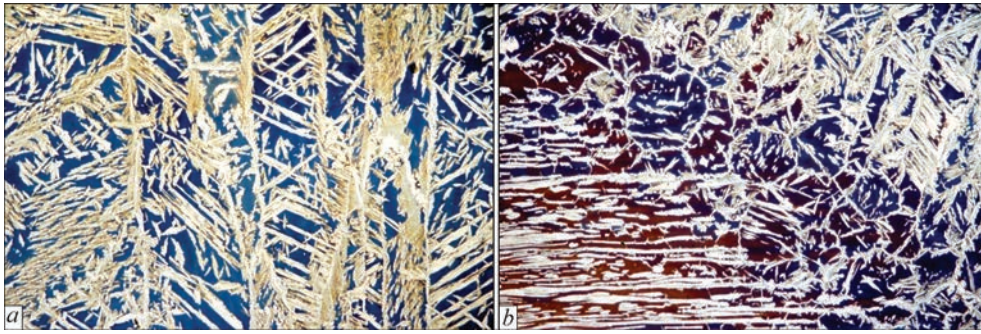


Figure 3. Microstructure ( $\times 100$ ) of weld metal (a) and HAZ (b) [11]

of chemical composition of metal, deposited with FOX CN 22/9N electrodes, characterized by a higher content of nickel. The HAZ overheated zone (Figure 3, b) was characterized by a higher content of ferrite, which, however, did not exceed the limit value of 70 % and was in the range from 54 to 69 %, while the transition zone contained local purely ferritic bands.

Hardness measurement was conducted along a line located 2 mm below the control weld surface. Hardness distribution in the joint cross-section along the measurement line is characteristic for duplex steels: base metal hardness was not higher than *HV* 5–270, hardness of weld metal and HAZ was approximately the same, and did not exceed critical values. This leads to the conclusion that no processes of secondary phase precipitation occurred under the impact of the thermal cycle of welding. It should be added that accurate hardness measurement was made difficult by a very narrow HAZ.

Investigations of samples of S32101 steel joints, made with E2209-T0-4 flux-cored wire at the depths of 20 and 60 m with welding mode variation (see Table), demonstrated a certain correlation of porosity and weld metal microstructure [15, 16]. The appearance of the deposited metal and its X-ray pattern are given in Figure 4. Metal porosity in welds made at the depth of 60 m was 6 to 14 % that is almost two times higher than in welding at 20 m depth (Figure 5). The authors attribute it mainly to increase of hydrostatic pressure.

Comparing experiments No.1 with No.2 and No.5 with No.6 (see Table), it is easy to see that at both the water depths porosity increases with voltage rise, and increase rates are 21 and 67 %, respectively. Similarly, comparing No.3 with No.4 and No.6 with No.8, at

lowering of welding speed porosity decreases by 31 and 20 %, respectively. However, at lowering of welding current porosity increases by 46 % at 20 m depth, and decreases by 17 % at 60 m depth. Reduction of weld porosity at 60 m depth can be associated with a higher heat input that leaves more time for the dissolved gas to escape, despite the higher hydrostatic pressure. Changes in welding parameters which can give more time for hydrogen removal, promote reduction of porosity.

Cr/Ni ratio in the welding wire was equal to 2.56, and it corresponds to the type of completely ferritic crystallization. Initial solidification of the melt pool includes epitaxial growth of ferrite from base metal on the fusion boundary. The temperature gradient determines the initial direction of dendrite growth and promotes formation of coarse columnar ferritic structure.

Microstructure of the metal of welds made at the depth of 20 and 60 m, differs significantly by distribu-

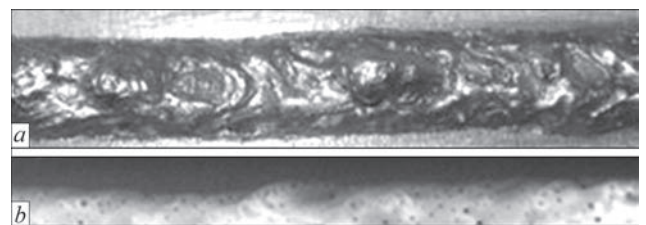


Figure 4. Appearance of the weld (a) and its X-ray pattern (b) [16]

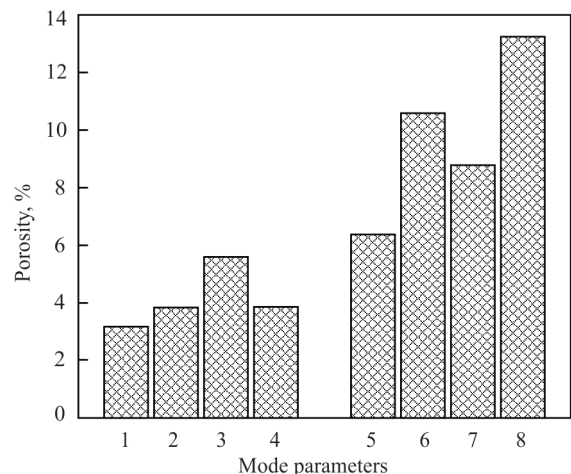


Figure 5. Weld porosity at different welding parameters (1–8 — experiment numbers (see table); 1–4 — 20 m depth; 5–6 — 60 m depth [16])

Welding mode parameters [16]

Number	<i>U</i> , V	<i>I</i> , A	<i>V</i> , mm/s	<i>H</i> , m	<i>Q</i> , kJ/mm	$\delta$ , %
1	27	275	8.5	20	874	3.16
2	33	275	8.5	20	1068	3.81
3	33	225	8.5	20	874	5.58
4	33	225	5.5	20	1350	3.86
5	27	275	5.5	60	1350	6.36
6	33	275	5.5	60	1650	10.59
7	33	225	5.5	60	1350	8.78
8	33	275	8.5	60	1068	13.23

tion and morphology of the austenitic phase. Any causes for reduction of the actually input amount of heat will stimulate initiation and growth of intragranular austenite due to relative increase of the cooling rate. Continuous network of austenite and fine particles develops in ferrite grains in the form of intragranular precipitates. The size of microstructural components of the weld metal can be reduced by increasing the welding speed.

When welding is performed with the same heat input, the microstructure and mechanical properties of the welds can differ. In other words, changing the input heat amount by changing the voltage or current can have different results. So, comparison of welds made in mode 1 and 3 (see Table) having the same heat input, shows that the high current promotes microstructure refinement. A similar result was obtained at welding in modes No.5 and No.7.

The authors explain the cause for the above phenomenon by a greater impact of the arc on the weld pool that causes a stronger convective motion, which leads to improvement of heat removal conditions.

The influence of welding parameters on the porosity and microstructure is of a complex and nonlinear nature. However, the diffusivity and solubility of hydrogen in ferrite and austenite differ significantly. The ferrite grain boundaries absorb hydrogen. Meanwhile, hydrogen atoms located on fine grain boundaries can diffuse easier, than those in larger grains. More over, increase of the heat input can extent the time of staying at a high temperature, and gas can easily leave the melt pool. As regards porosity and microstructure ratio, the welding parameters should be considered together.

Comparative studies of the structure of metal and HAZ at dry welding in the chamber and directly in the water environment [17] (Figure 6), showed that the

width of the high-temperature region, which is heated above 1000 °C, somewhat decreases, and is equal to 30–70 μm. At the same time the austenite grain size also becomes smaller. The authors attribute it to shortening of the recrystallization time and increase of the amount of  $\gamma$ -phase, as well as limitations of diffusion of stabilizing elements from the weld metal. Farther from the fusion line, the volume fraction of austenite becomes smaller, more intensively at wet welding than at the dry process: from 35.01 to 25.39 % and from 51.61 to 32.29 %, respectively.

In the weld metal the previous transformation austenite (PTA) and grain boundary (GBA) austenite precipitated rapidly along the ferrite grain boundaries (Figure 6, weld section adjacent to the fusion line). A large amount of austenite precipitates in the form of Widmanstatten austenite (WA), which grows into the ferrite grains, and particles of intragranular austenite (IGA) of an acicular morphology are observed in the ferrite grains (Figure 6, weld metal in the center and near the fusion line). Compared to dry welding, the volume fraction of these structural components becomes smaller. A higher cooling rate shortened the transformation time.  $\gamma$ -stabilizers, such as N, Ni, and Mn had less time for diffusion that restrained the nucleation and growth of the austenite grains.

Microstructural studies of the HAZ high-temperature zone revealed appearance of pits on the boundaries of  $\alpha$ - $\alpha$  and  $\alpha$ - $\gamma$  grains, as well as inside the ferrite grains that is indicative of precipitation of chromium-enriched nitrides in these areas after welding. The probability of their formation at wet welding becomes higher. With increase of the heat input, the volume fraction of chromium nitrides decreases as a result of cooling rate lowering.

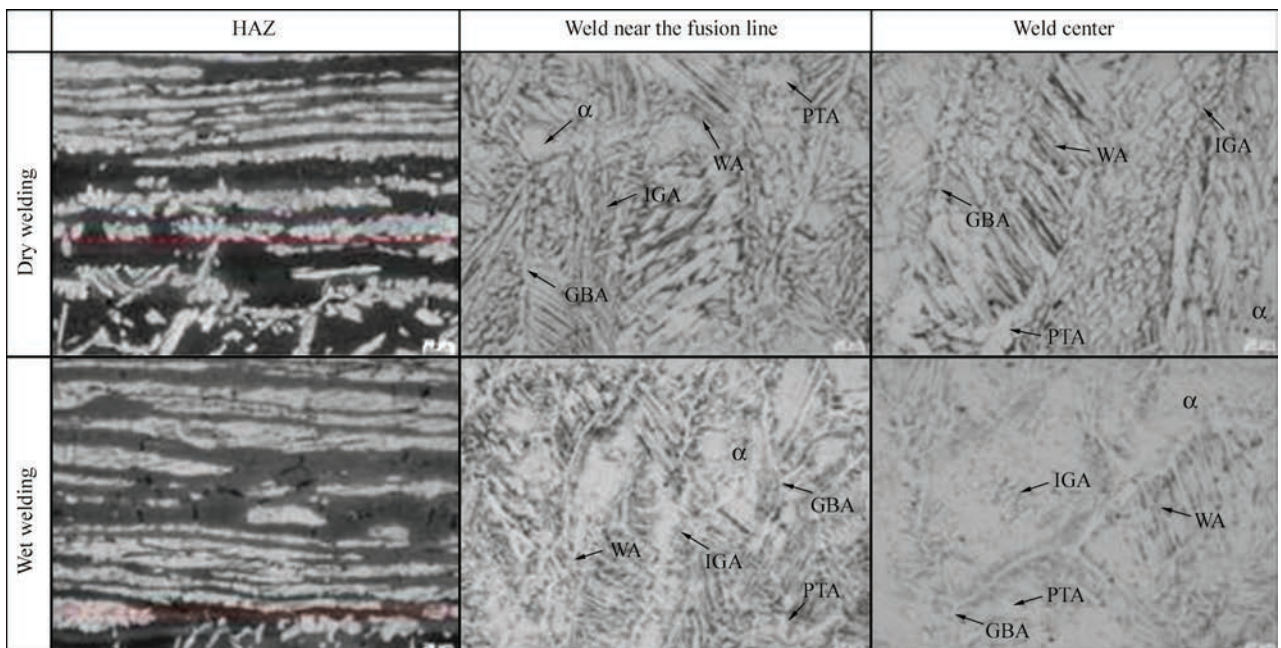
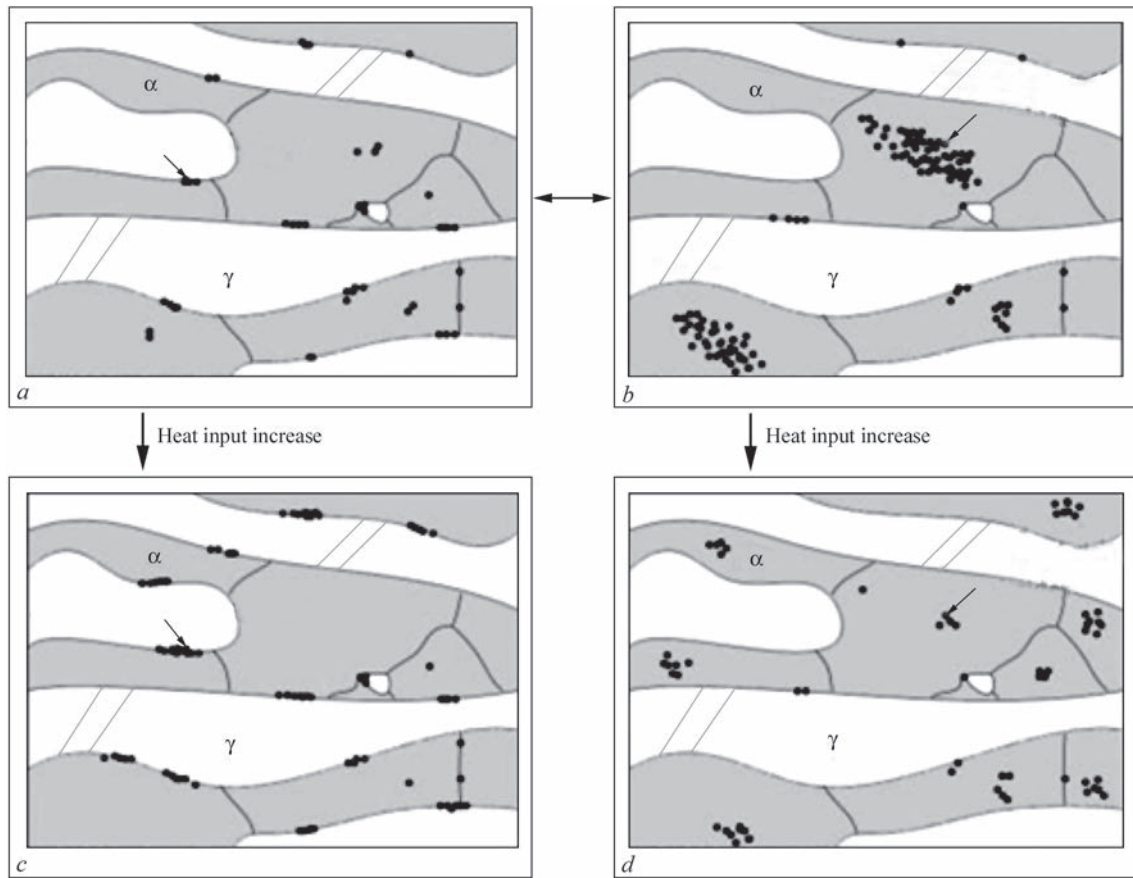


Figure 6. Microstructure of welded joint zones [17]



**Figure 7.** Schematic diagrams of distribution of chromium-enriched nitrides in the HAZ low-temperature zone [17]. The arrows show chromium-enriched nitrides inside the  $\alpha$ -phase and on  $\alpha/\gamma$  boundary

A longer stay at increased temperature promotes nitride precipitation, which occurs on  $\gamma/\alpha$  and  $\alpha/\alpha$  interface, due to a high coherence of these boundaries. In addition, a small amount of chromium nitrides appeared in  $\alpha$ -phase. A large amount of heat allowed enough time for nitrogen atoms for diffusion that prevents oversaturated nitride deposition. The obtained results are schematically presented in the diagram in Figure 7.

Precipitation of chromium nitrides leads to depletion of the adjacent areas in chromium that had a strong impact on local corrosion resistance. Figure 8 shows the graphs of  $I_r/I_a$  values for the base metal and low-temperature region of the HAZ for different heat inputs. Base metal demonstrated the highest density of activation current  $I_a$  and the lowest density of reactivation current  $I_r$  ( $1.83 \cdot 10^{-2}$  and  $4.25 \cdot 10^{-6}$ , respectively). The degree of activation was the highest at the value of  $I_r/I_a = 2.32 \cdot 10^{-4}$ . As BM was exposed to a series of thermal cycles, it demonstrated a balanced microstructure. Austenite was uniformly distributed in the ferrite matrix and no harmful secondary phases (such as carbides, nitrides,  $\sigma$  or  $\chi$  phases) were revealed. This is indicative of the fact that the base metal demonstrated better resistance to local corrosion that did the HAZ metal.

It should be noted that  $I_r/I_a$  values gradually increased at dry welding from  $2.60 \cdot 10^{-3}$  at minimum heat input (726 J/mm) to  $6.67 \cdot 10^{-3}$  at maximum heat input (1383.3 J/mm) (Figure 8). In the latter case, the metal was ex-

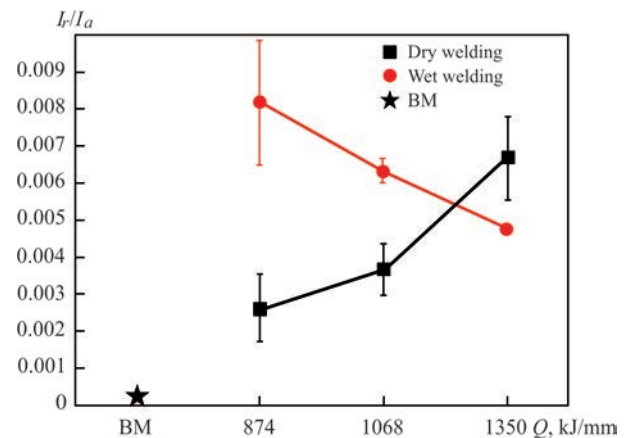


**Figure 8.**  $I_r/I_a$  values for base metal and HAZ low-temperature region for different heat inputs [17]

posed to heat treatment for a longer time and the nitrides also had more time for precipitation on  $\gamma/\alpha$  and  $\alpha/\alpha$  boundaries, owing to high coherence. Thus, at dry welding the degree of nitride precipitation and sensitivity to local corrosion increased with heat input increase. At wet welding  $I_r/I_a$  values gradually decreased from  $8.18 \cdot 10^{-3}$  at minimum heat input to  $4.78 \cdot 10^{-3}$  at maximum heat input that is indicative of increase of local corrosion resistance with heat input increase. Dissolution of part of austenite led to higher nitrogen content in ferrite of the HAZ metal. Chromium nitrides were deposited from a ferrite mixture as the high cooling rate led to decrease of

nitrogen solubility. Here, the probability of their deposition decreased, because of the high cooling rate and short ageing time. Thus, at wet welding the volume fraction of chromium nitrides in  $\alpha$ -phase decreased with increase of the heat input that promotes lowering of the sensitivity to local corrosion. As a result, the metal of the weld HAZ at wet welding becomes less sensitive to local corrosion at maximum heat input than at dry welding.

## Conclusions

1. At present general purpose electrodes and flux-cored wires are used for wet underwater welding of duplex steels, because of absence of specialized welding consumables.

2. Destabilization of the arcing process in the water environment leads to cold cracking in the weld metal. No cracks were revealed in the HAZ.

3. Welds made in air and under the water using coated electrodes, were characterized by a similar structure. Intensive cooling that is ensured by the water environment, did not lead to increase of ferrite content in the weld or HAZ, compared to its content in the joints made in air.

4. Analysis of hardness distribution in the studied joints did not reveal any significant differences in welds made in air and in water. Hardness values, determined in the HAZ, were limited by a range falling between the values of base metal hardness and deposited metal hardness.

5. Size of austenite phases at dry welding was larger than at wet welding under the same heat input conditions. At wet welding the  $\gamma/\alpha$  ratio increased considerably at increase of the heat input: from 27.31 to 39.46 % for the weld center and from 35.01 to 44.9 % for weld metal adjacent to the fusion line.

6. All the studied variants of weld metal composition were insensitive to local corrosion, because of the high PREN values. The weld metal adjacent to the fusion line, showed optimum resistance to local corrosion, and the weld metal demonstrated better local corrosion resistance than did the HAZ. Local corrosion resistance of the HAZ low-temperature zone increased with increase of the heat input at wet welding, while a reverse tendency was observed in the case of dry welding. The HAZ high-temperature zone at dry welding demonstrated an improved local corrosion resistance, compared to that for welded joints made by wet welding under the same heat input conditions.

7. Further studies will be related to stabilization of the arcing process, and determination of the impact of different conditions of the welding process on the possi-

bility of cold crack formation, for instance, effect of water type (fresh, sea), or change of the geometry of welded joint edge preparation and development of specialized electrode materials for wet welding of duplex steels.

- Charles, J. (2007) Duplex stainless steels, a review after DSS'07 held in Grado. In: *Proc. of the Duplex Stainless Steel Conf., Maastricht. The Netherlands, 18–20 June 2007*.
- Labanowski, J., Fydrych, D., Rogalski, G., Samson, K. (2011) Underwater welding of duplex stainless steel. *Solid State Phenomena*, **183**, 101–106.
- Kacar, R. (2004) Effect of solidification mode and morphology of microstructure on the hydrogen content of duplex stainless steel weld metal. *Mater. Design*, **25**(1), 1–9.
- Lage, M.A., Assis, K.S., Mattos, O.R. (2015) Hydrogen influence on fracture toughness of the weld metal in super duplex stainless steel (UNS S32750) welded with two different heat input. *Int. J. Hydrogen Energ.*, **40**(47), 17000–17008.
- Farrell, J. (1996) *Hyperbaric welding of duplex stainless steel pipelines offshore*: Ph. D. Thesis School of Industrial and Manufacturing Science. Cranfield University.
- Karlsson, L. (1999) Intermetallic phase precipitation in duplex stainless steels and weld metals metallurgy, influence on properties and welding aspects. *Weld. World*, **43**, 20–41.
- Labanowski, J. (1997) Duplex steels — new material for chemical processing industry. *Engineering and Chemical Equipment*, **2**, 3–10.
- Muthupandi, V., Bala Srinivasan, P., Seshadri, S.K., Sundaresan, S. (2003) Effect of weld metal chemistry and heat input on the structure and properties of duplex stainless steel welds. *Materials Sci. and Eng.*, **358**, 9–16.
- Shinozaki, K., Ke, L., North, T.H. (1992) Hydrogen cracking in duplex stainless steel weld metal. *Welding J.*, **11**, 387–396.
- Prokop-Strzelczyńska, K., Rogalski, G. (2016) Cold cracking susceptibility of joints made of ferritic austenitic duplex steel 2205 during underwater welding. *Biuletyn Instytutu Spawalnictwa w Gliwicach*, **2**(16), 35–42.
- Labanowski, J., Prokop-Strzelczyńska, K., Rogalski, G., Fydrych, D. (2016) The effect of wet underwater welding on cold cracking susceptibility of duplex stainless steel. *Advances in Materials Sci.*, **16**(2), 68–77.
- Kralj, S., Garasic I., Kozuh, Z. (2009) Underwater wet welding of duplex steel. *Welding in the World*, **53**, 35–40.
- Yu Hu, Yonghua SHI, Kun Sun, Xiaoqin Shen (2019) Microstructure evolution and mechanical performance of underwater local dry welded DSS metals at various simulated water depths. *J. of Materials Processing Tech.*, **264**, 366–376.
- Prokop-Strzelczyńska, K. (2016) Cold cracking susceptibility of joints made of ferritic-austenitic duplex steel 2205 during underwater wet welding. *Biuletyn Instytutu Spawalnictwa w Gliwicach*, **16**(2), 35–42.
- Shi, Y., Hu, Y., Li, Z. et al. (2016) Research on porosity of underwater wet FCAW duplex stainless steel. *China Welding*, **25**(2), 27–33.
- Shi, Y., Hu, Y., Yi, Y. et al. (2017) Porosity and microstructure of underwater wet FCAW of duplex stainless steel. *Metallography, Microstructure, and Analysis*, **6**, 383–389.
- Kun Sun, Min Zeng, Yonghua SHI et al. (2018) Microstructure and corrosion behavior of S32101 stainless steel underwater dry and wet welded joints. *J. of Materials Processing Technology*, **256**, 190–201.

Received 07.07.2021

## SOME ADVANTAGES OF WELDED JOINTS OF ALUMINIUM 1201 ALLOY PRODUCED BY FRICTION STIR WELDING

**A.G. Poklyatskyi, S.I. Motrunich, I.M. Klochkov and T.M. Labur**

E.O. Paton Electric Welding Institute of the NAS of Ukraine

11 Kazymyr Malevykh Str., 03150, Kyiv, Ukraine. E-mail: [office@paton.kiev.ua](mailto:office@paton.kiev.ua)

The paper analyzes the structural features, characteristics of strength and resistance to initiation and propagation of in-service cracks of butt joints on 1201 aluminium alloy of 2 mm thickness, produced by friction stir welding (FSW) and argon-arc welding with nonconsumable electrode (argon TIG). It is shown that in FSW as a result of intensive plastic deformation of metal in the weld nugget, a fine-grained structure with a grain size of 5–6  $\mu\text{m}$  is formed. In the zone of thermomechanical impact, deformed extended grains are observed, oriented in the direction of movement of plasticized metal, as well as small equiaxial grains, the size of which varies within 4–12  $\mu\text{m}$ , whereas at argon TIG welding of this alloy the weld metal has a characteristic cast structure with large (0.20–0.25 mm) dendrites. The absence of beads and reinforcements in the welds produced by FSW, allows avoiding high levels of stress concentration in the places of transition from the weld to base material, which negatively affect the service and life characteristics of welded joints. The peculiarities of formation of permanent joints in the solid phase during FSW also help to reduce the degree of metal softening in the welding zone and increase their ultimate strength, and resistance to initiation and propagation of operational cracks. 15 Ref., 7 Figures.

*Keywords: microstructure, hardness, ultimate strength, resistance to initiation and propagation of in-service cracks*

For the last twenty years friction stir welding (FSW) has been widely applied in many countries of the world for integration of flat and three-dimensional panels, which are used in manufacture of the hulls of ships, ferries, bodies of railway cars, etc. [1–5]. Such a process of producing permanent joints in the solid phase has become applied in car-making, electrical engineering, construction, as well as in aerospace engineering, including fuel tanks for liquid hydrogen and liquid oxygen [2, 6–9]. In our countries heat-hardenable 1201 alloy of Al–Cu–Mn alloying system is used for fabrication of welded structures exposed to low temperature in service. This alloy contains 5.8–6.8 % Cu and 0.2–0.4 % Mn. It has high (>425 MPa) strength and preserves its ductility to –253 °C. In addition, presence of manganese and titanium in the alloy ensures its rather high heat resistance. Satisfactory weldability of the alloy allows its wide application to restore the welded structures, operating for a long time at up to 200 °C temperatures, and at up to 300 °C temperatures for a short time. However, in fusion welding, melting of a certain volume of the materials being joined and welding wire in a common weld pool and their subsequent solidification, considerable structural transformations take place in the metal of the weld and adjacent areas and defects appear quite often in

the form of pores, oxide film macroinclusions, and hot cracks. As a result, the strength of welded joints of 1201 alloy produced by fusion welding does not exceed 70 % of that of the base metal in most of the cases [10, 11].

At FSW weld formation occurs in the solid phase, as a result of heating due to friction of a certain volume of the materials being joined up to a plastic state and its stirring by a special tool in a closed space, limited by the substrate and working surfaces of the tool shoulder and pin. That is, the process of permanent joint formation takes place without application of an arc discharge and without metal melting and crystallization, and here there is no need to additionally apply filler wire or shielding gas. Due to that the FSW process has several advantages, compared to fusion welding. Among them, we should note formation of a fine-crystalline weld structure, less pronounced softening of the joined materials, preservation of their chemical composition, absence of defects, characteristic for fusion welding and improvement of mechanical properties of welded joints [12, 13].

The objective of this work is determination of the advantages of FSW process, compared to argon TIG welding, when producing butt joints of sheet aluminium alloy 1201.

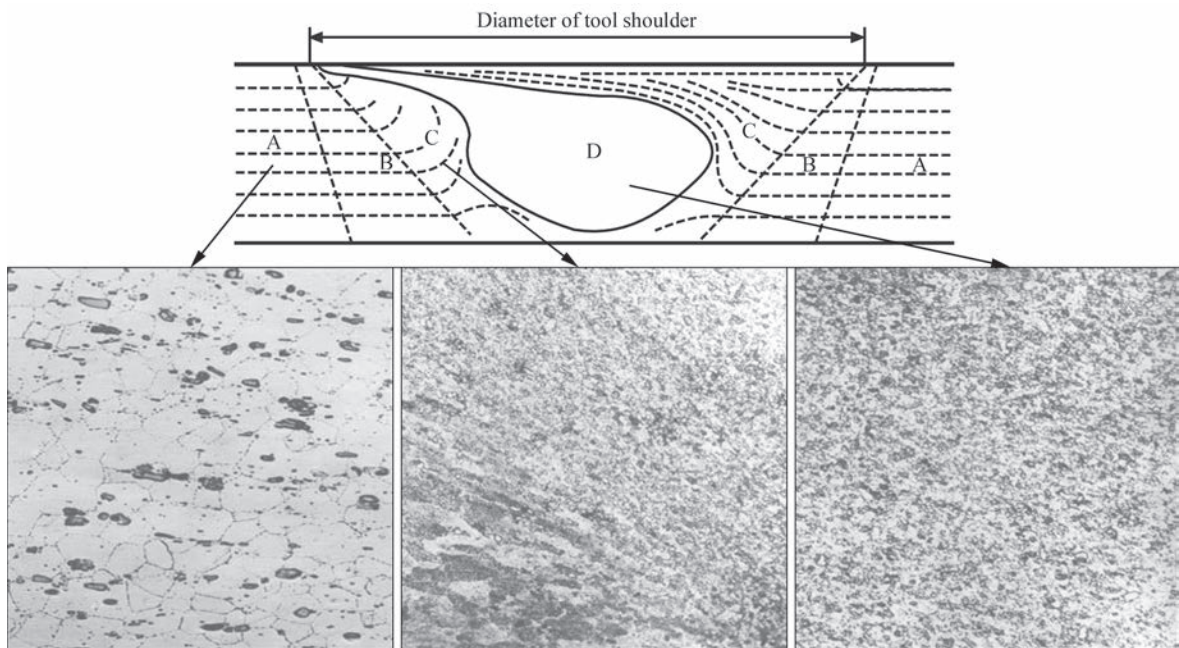


**Figure 1.** Schematic representation of characteristic zones in FSW joint and metal microstructure ( $\times 400$ ) in these zones of a butt joint of 2 mm 1201 alloy

Sheets of 2 mm 1201 aluminium alloy were used for investigations. Butt joints were produced by non-consumable electrode argon-arc welding with 20 m/h speed at 145 A current in MW-450 welding machine («Fronius», Austria), using 1.6 mm Sv1201 filler wire. FSW was performed in a laboratory unit developed at PWI, using a special tool with a conical pin and shoulder diameter of 12 mm [14], the rotation speed of which was 1420 rpm, and linear displacement speed was 14 m/h. The produced welded joints were used to prepare sections to study the structural features of welds and samples with 15 mm width of the working part, in order to determine their ultimate strength at uniaxial tension, in keeping with GOST 6996–66. Argon TIG welded samples were tested both with the beads removed to base material level, and with additionally cleaned weld reinforcement. Mechanical testing of the samples was performed in an all-purpose servohydraulic complex MTS 318.25. Fracture resistance characteristics of base material and welded joints were determined on Kan samples [15] with a sharp notch ( $R = 0.1$  mm), which ensures crack initiation at a relatively low energy level, using an all-purpose testing machine RU-5. The notch was placed so that its tip coincided with the weld axis. The ultimate strength at simultaneous stretching and bending of the sample and specific work of crack propagation were determined, using «load-deformation» diagrams, obtained during testing. Metal hardness was measured on face surface of scraped joints. The degree of metal softening in the welding zone was assessed in ROCKWELL instrument at the load of

$P = 600$  N. Structural features of welded joints were evaluated using optical electron microscope MIM-8.

Performed research revealed that the features of FSW process lead to formation of a specific structure of welded joints (Figure 1). They are divided into the central part of the weld (nugget), formed mainly in the zone of action of the working surfaces of the tool pin (D); zone of thermomechanical impact, adjacent to it, where the metal was exposed to thermal and mechanical impact as a result of the tool rotation and linear displacement (C), as well as HAZ (B), where structural changes of the base metal (A) are due only to temperature change, similar to fusion welding.

Microstructural analysis of the transverse sections of the produced butt welded joints of 2 mm 1201 alloy is indicative of the fact that a fine-crystalline structure forms in the weld nugget as a result of intensive plastic deformation, with grain size of 5–6  $\mu\text{m}$ . Here, the size of grains and intermetallic inclusions is 5–7 times smaller than in the base material, so that the volume fraction of their boundaries becomes much greater. In the thermomechanical impact zone deformed extended grains which are oriented in the direction of plasticized metal movement, and fine equiaxed grains, the size of which varies in the range of 4–12  $\mu\text{m}$ , are observed, whereas in nonconsumable electrode argon-arc welding of this alloy using Sv1201 filler wire, the weld forms a characteristic cast metal structure with rather large (0.20–0.25 mm) dendrites, as a result of molten metal crystallization (Figure 2). In the zone of weld fusion with the base material, the impact of high-temperature heating of metal leads to partial melting of structural components of the grain

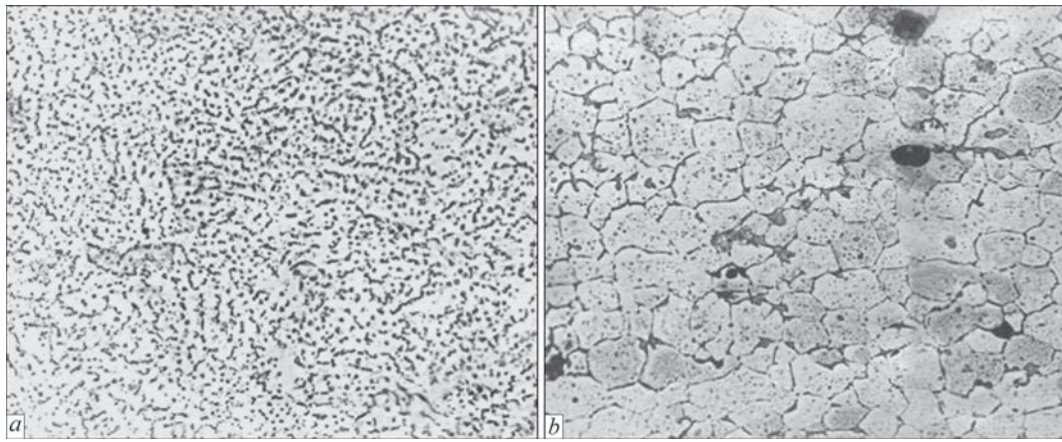


**Figure 2.** Microstructure ( $\times 400$ ) of weld metal (*a*) and zone of its fusion with base material (*b*) obtained at argon TIG welding of 2 mm 1201 alloy using Sv1201 filler wire

boundaries at permanent joint formation. It results in formation of a coarse continuous net of brittle fine-grained interlayers, which have a negative effect on the mechanical properties of such joints.

The microstructure of welded joint surface, shown in Figure 3, can provide a visual illustration of structural transformations in the FSW metal, as a result of its intensive plastic deformation. It clearly shows the change of grain sizes in the metal being welded near the tool shoulder edge on the interface of the HAZ (on the left) with the thermomechanical impact zone (on the right). In the areas, which directly interacted with the tool working surfaces (thermomechanical impact

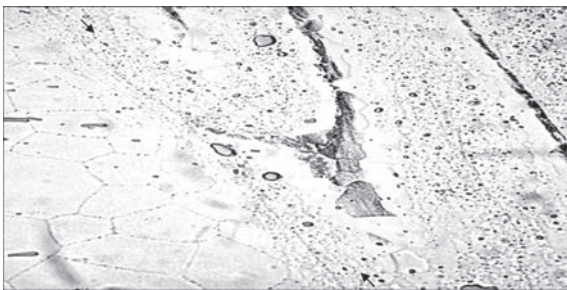


**Figure 3.** Microstructure ( $\times 500$ ) of the surface of 2 mm 1201 alloy welded joint on the interface of the HAZ (left) and thermomechanical impact zone (right) of FSW joint

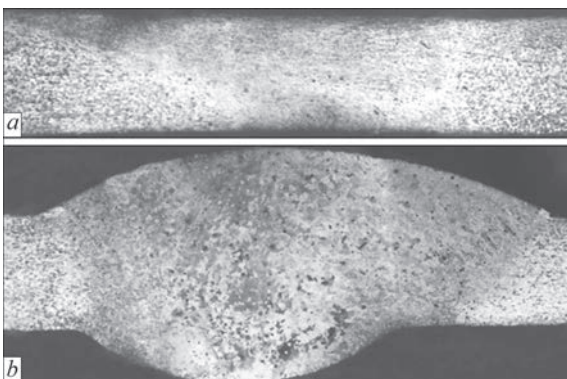


**Figure 4.** Cross-sections of welds of 2 mm 1201 alloy, produced by FSW (*a*) and argon TIG welding (*b*)

zone and weld) a pronounced refinement of welded metal grains takes place.

Performed studies showed that FSW welds differ favourably by their shape and dimensions from those made by fusion welding, due to permanent joint formation on a backing without a groove and without filler wire application (Figure 4). Absence of beads or reinforcements in such welds allows avoiding the high levels of stress concentration in the points of weld to base metal transition, which have an adverse

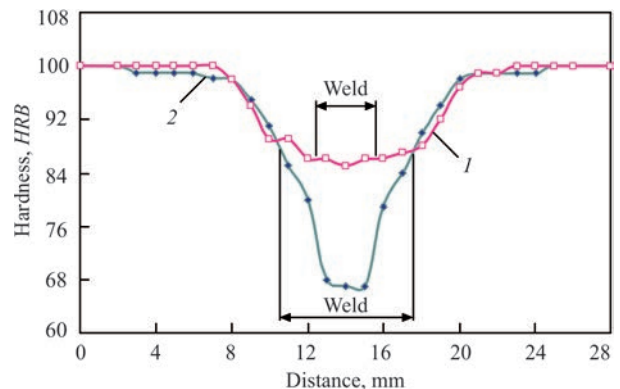


**Figure 5.** Hardness distribution in welded joints of 2 mm 1201 alloy produced by FSW (*1*) and argon TIG welding (*2*)

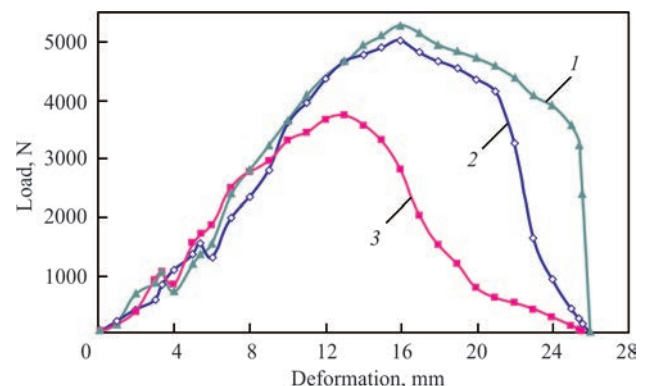


**Figure 6.** «Load-deformation» diagrams recorded at simultaneous stretching and bending of Kan samples with a sharp notch from BM (*a*) and welded joints of 2 mm 1201 alloy produced by FSW (*2*) and argon TIG welding (*3*)

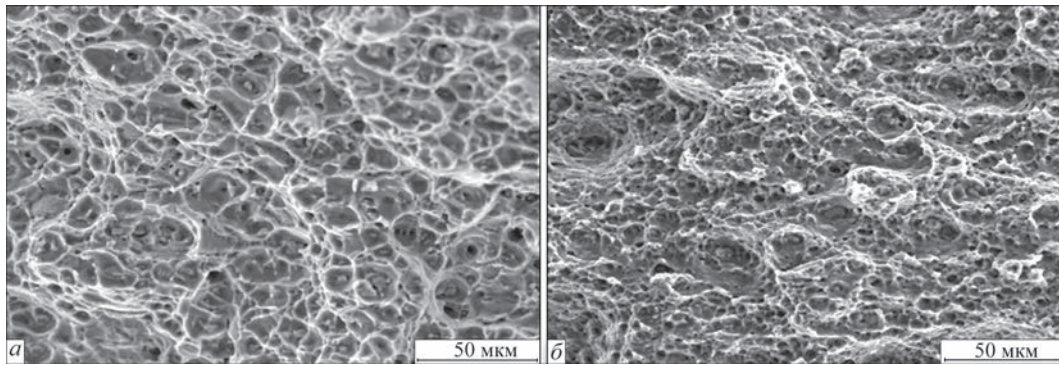


**Figure 7.** Fractograms of fracture surfaces of samples of FSW welded joints on 2 mm 1201 alloy in the weld metal (*a*) and in the weld to base material transition zone (*b*) ( $\times 500$ )

effect on the service and life characteristics of the welded joints.

Moreover, it was shown as a result of the performed studies that the features of formation of solid-phase permanent joints at FSW also promote lowering of the degree of metal softening in the welding zone and improvement of its mechanical properties. So, measurement of metal hardness in the weld formation zone showed that it is much higher at FSW than at argon TIG welding (Figure 5). Solid phase welded joints have minimum metal hardness on the level of *HRB* 85–86 in the weld and zones of its mating with the base material, whereas at argon TIG of 2101 alloy using Sv1201 filler wire the minimal metal hardness in the weld central part is on the level of *HRB* 67–68, and in the zone of fusion with the base material it is on the level of *HRB* 87–88.

The ultimate strength of samples of 1201 alloy welded joints with reinforcement, produced by argon TIG, using Sv1201 filler wire, is on the level of 296 MPa. Fracture of such samples at static tension takes place in the zone of the weld fusion with the base material, where a network of brittle fine-grained interlayers forms during welding. Samples with removed weld reinforcement fail at stretching in the weld central part, where metal hardness is minimal, and have the strength on the level of 241 MPa. As filler wire is not used at FSW, the welded joints have no weld reinforcement. However, due to lower metal softening in the welding and forming zone in the welds and in the adjacent areas of the deformed fine-grained structure of the welds, the ultimate strength of samples of such welded joints at uniaxial tension is on the level of 303 MPa. Here, their fracture takes place in the zone of thermomechanical impact in the area of weld transition to base material.

Curves, obtained at simultaneous tension and bending of Kan samples with a sharp notch, are indicative of susceptibility of 1201 alloy to rapid initiation and propagation of cracks (Figure 6). At testing of argon TIG welded joint samples, the crack initiating

near the stress raiser tip in the form of a sharp notch propagates through the weld metal, whereas in friction stir welded samples after initiation in the weld, it shifts to the zone of weld transition to base material. Here, the presented diagrams demonstrate that the rate of crack initiation and nature of its propagation in FSW samples, are approximately the same as those in the base metal. However, fracture of such samples occurs at loads, close to those in the base metal, or much higher, than that in fusion welded samples. Minimum value of specific work of crack propagation in the base metal is on the level of 2.7 J/cm<sup>2</sup>, indicating that crack propagation proceeds more readily in it than in welds produced in the solid phase and by melting, for which these values are 3.8 and 3.5 J/cm<sup>2</sup>, respectively.

Analysis of fractograms of fracture surface on samples of FSW joints reveals the tough mode of their fracture (Figure 7). In the weld central part, near the notch tip, shallow pits without any flat areas of the relief are clearly visible. Propagation of the main crack through the metal of such a weld will require high-energy consumption and will be accompanied by considerable plastic deformation. Therefore, at testing such samples, the crack shifts into the zone of weld transition to base material, where the fractogram of fracture of this region shows pits limited by sharp ridges, that is indicative of quasicleavage mechanism, which requires lower energy consumption.

## Conclusions

1. Intensive plastic deformation of metal at FSW of 1201 alloy results in formation of a fine-crystalline structure with 5–6  $\mu\text{m}$  grain size in the weld nugget. Deformed extended grains oriented in the direction of plasticized metal displacement and fine equiaxed grains, the size of which varies within 4–12  $\mu\text{m}$ , are observed in the thermomechanical impact zone, while at argon TIG welding of this alloy the weld forms a characteristic cast structure of the metal with grain sizes of 0.20–0.25 mm. In the zone of the weld fusion with the base material partial melting of the structur-

al components of grain boundaries takes place, and a continuous net of brittle fine-grained interlayers is formed, which have an adverse effect on the joint mechanical properties.

2. Owing to formation of permanent joints on a backing without a groove and without application of filler wire, FSW welds have no beads or reinforcement that allows avoiding high levels of stress concentration in the places of transition from the weld to base material, which have a negative impact on the service and life characteristics of the welded joints.

3. FSW process runs in the solid phase that ensures considerable lowering of metal softening in the welding zone and improvement of mechanical properties of 1201 alloy welded joints. Hardness of FSW weld metal is on the level of *HRB* 85–86 that is 25 % higher than at argon TIG welding. Ultimate strength of samples of such joints at uniaxial tension is on the level of 303 MPa, while for samples without weld reinforcement, obtained at argon TIG welding, this value is just 241 MPa. Fracture resistance values at simultaneous stretching and bending of samples of FSW welded joints are indicative of their higher resistance to crack initiation and propagation in operation, than of those produced by fusion processes.

1. Lahti, K. (2003) FSW — possibilities in shipbuilding. *Svet-saren*, **1**, 6–8.
2. Kallee, S., Nicholas, D. (1998) Causing a stir in the future. *Welding and Joining*, **2**, 18–21.
3. Okamura, H., Aota, K., Ezumi, M. (2000) Friction stir welding of aluminium alloy and application to structure. *J. of Japan Institute of Light Metals*, **4**, 166–172.
4. Mori, H., Noda, M., Tominaga, T. (2007) Current state on application of friction stir welding for rolling stock. *Ibid.*, **11**, 506–510.
5. Kallee, S.W., Davenport, J., Nicholas, E.D. (2002) Railway manufacturers implement friction stir welding. *Welding J.*, **10**, 47–50.
6. Arbegast, W.J. (2006) Friction stir welding after a decade of development. *Ibid.*, **3**, 28–35.
7. Johnsen, M.R. (1999) Friction stir welding takes off at Boeing. *Ibid.*, **2**, 35–39.
8. Kallee, S., Nicholas, E., Thomas, W. (2002) Friction stir in aerospace — the industrial way. Pt II. *Bulletin TWI*, **9–10**, 13–18.
9. Takehisa, H. (2006) Friction stir welding technology of aluminium alloys for aircraft. *J. of Japan Institute of Light Metals*, **3**, 178–183.
10. Beletsky, V.M., Krivov, G.A. (2005) *Aluminium alloys. Composition, properties, technology, application*: Refer. Book. Ed. by I.N. Fridlyander. Kiev, KOMINTEKH. ISBN 966-8550-25-0 [in Russian].
11. Mashin, V.S., Poklyatsky, A.G., Fedorchuk, V.E. (2005) Mechanical properties of aluminium alloys in consumable and nonconsumable electrode arc welding. *The Paton Welding J.*, **9**, 39–45.
12. Defalco, J. (2006) Friction stir welding vs. fusion welding. *Welding J.*, **3**, 42–44.
13. Pietras, A., Zadroga, L., Lomozik, M. (2004) Characteristics of welds formed by pressure welding incorporating stirring of the weld material (FSW). *Welding Int.*, **1**, 5–10.
14. Ishchenko, A.Ya., Poklyatsky, A.G. (2010) *Tool for friction stir welding of aluminium alloys*. Pat. 54096 Ukraine, Int. Cl. B23K 20/12; u201005315; Fill. 30.04.2010; Publ. 25.10.2010 [in Ukrainian].
15. Poklyatsky, A.G. (2011) Resistance of welds on thin-sheet aluminium alloys to initiation and propagation of service cracks. *The Paton Welding J.*, **10**, 5–9.

Received 08.07.2021

### SCIENTIFIC & TECHNICAL COMPLEX «THE E.O. PATON ELECTRIC WELDING INSTITUTE»



Ultrasonic testing of wind turbine hub

STC «The E.O. Paton Electric Welding Institute» works in various areas of industry (such as machinery/engineering, shipbuilding, trunk pipelines, nuclear power plants, etc.) with structures that are working under difficult condition (that includes variable amplitude loading, very high and low temperatures, different aggressive environment).

STC has comprehensive solution to problems related to:

- design and modelling of various construction;
- integrity and strength analysis;
- non-destructive testing, microstructure analysis, mechanical testing;
- risk analysis and incidents investigation;
- modeling of thermohydraulic processes;
- repair and coating of elements and structures;
- improving fatigue life of welded joints;
- extension of economic life of current equipment.

# INFLUENCE OF DEFORMATIONS FROM STATIC LOADS ON IMPACT AND FRACTURE TOUGHNESS OF CYLINDRICAL SHELLS

V.P. Dyadin, Ye.O. Davydov and R.I. Dmytrienko

E.O. Paton Electric Welding Institute of the NAS of Ukraine

11 Kazymyr Malevych Str., 03150, Kyiv, Ukraine. E-mail: [office@paton.kiev.ua](mailto:office@paton.kiev.ua)

The work is a study of the effect of accumulation of plastic deformation in the base metal of the pipeline from the action of inner pressure on the change of impact toughness of the Charpy specimens cut out in the longitudinal and circumferential directions. The studies in this direction are carried out on the specimen made from electrically-welded straight seam pipe of 630×8 from 17G1S steel. The obtained test results allow correcting the requirements to the specific work of impact specimens taking into account its possible reduction depending on the predicted plastic deformation of the structural element and anisotropic properties of the material. 17 Ref., 4 Tables, 10 Figures.

*Keywords:* plastic deformation, ageing, impact toughness, heat-affected zone, brittle-ductile transition temperature, fracture toughness characteristics

Various processes can develop in pipelines in operation, including strain ageing. Its development, on the one hand, leads to adverse consequences, which lower the ductility and toughness values of pipeline and pressure vessel metal, and on the other hand — ageing is used as a variant of treatment, which allows improvement of structural strength of steel products [1].

Direct evaluation of the impact of strain ageing on the change of structural material properties involves a number of difficulties, associated with absence of reliable witness-specimens. Application of the results of collateral testing, performed earlier, does not allow guaranteeing the correctness of the conclusions, because of a considerable scatter of the metal rolled stock properties, characteristic for mass production structural steels. So, works [2–4] report absence of reliable data that is one of the main causes for contradictions between the results of different studies. Further complications during such evaluations are also related to that the maximum possible changes between the metal properties during natural strain ageing after operation should be determined not so much by time, as by the magnitude of the accumulated plastic deformation.

A feature of plastic deformations in pipelines is their local nature that complicates their direct determination, and they can reach 7 and more percent [5]. Moreover, plastic deformations may accumulate in the areas of mechanical damage, corrosion defects, corrugations, etc. Plastic deformation increases the

rate of corrosion processes in the areas of accumulation of plastic damage of metal.

Change of local mechanical, ductile and corrosion properties of metal of various purpose pipelines, is the main practical result of their strain ageing.

Of all the mechanical characteristics the most dangerous, as a result of strain ageing, is the change of structural steel susceptibility to brittle and ductile fracture, which are measured in terms of the values of impact toughness (*KCV*), critical brittleness temperature ( $T_{cr}$ ) and nominal breaking stress.

Allowing for the negative impact of plastic deformation accumulation on structural strength is quite widely covered in works [6–11].

Research performed at PWI shows that in the presence of cracklike defects in the pipeline, the structural steel toughness is determined by the steel resistance to initiation and propagation of a ductile crack up to formation of a ductile zone or through thickness defect. At the initial stage the material ability to resist initiation of ductile crack extension is characterized by deformation criterion  $\delta_i$  (value of critical crack tip opening displacement at the moment of ductile crack initiation). The second stage is related to stable growth of the crack, and it is characterized by the tangent of the opening angle of a stable propagating crack (COA) [12, 13].

It is known from local and foreign publications that the current requirements to the value of impact toughness of a Charpy specimen correlate quite well

with the resistance of structural steels and their joints to possible fractures, which, in their turn, are characterized using different criteria of fracture mechanics. Thus, impact toughness values of a Charpy specimen indirectly characterize the resistance of structural materials and their joints to possible defect growth.

Approaches developed at PWI for determination of  $\delta_i$  (mm),  $K_{1c}^{(t)}$  (kgf/mm<sup>3/2</sup>), and COA (tgα) characteristics by the results of impact testing of standard Charpy specimens 10 mm thick (GOST 9454–78) and of their strength allow considerably simplifying such assessment [12–17]:

$$\delta_i = 0.05 KCV_{\max} / \sigma_{0.2}; \tag{1}$$

$$K_{1c}^{(t)} = (A \cdot E \cdot KCV^{(t)} / (1 - \nu^2))^{0.5}; \tag{2}$$

$$\text{tg}\alpha = 0.5 \frac{\sigma_t}{\sigma_{0.2}} \varepsilon_t (1 + \varepsilon_t), \tag{3}$$

where  $K_{1c}^{(t)}$  is the crack resistance characteristic at propagation of a through-thickness crack in a structural element of thickness  $t$  for temperature  $T$ ;  $A$  is the correlation factor;  $KCV^{(t)}$  is the Charpy specimen impact toughness (J/cm<sup>2</sup>) at corrected temperature  $T'$ , taking into account the thickness;  $KCV_{\max}$  is the specific work of destruction of the Charpy specimen on the «upper shelf» (at completely ductile fracture):  $T' = T + \Delta T$ , where  $\Delta T$  is temperature shift at limitation of the thickness of structural elements ( $5 \text{ mm} < t < 10 \text{ mm}$ );  $\varepsilon_t$  is the deformation, which corresponds to tensile strength of the material  $\sigma_t$ ;  $\sigma_{0.2}$  is the yield limit (kgf/mm<sup>2</sup>);  $E$  is the modulus of elasticity, (kgf/mm<sup>2</sup>).

Dependence (3) has certain physical meaning, the essence of which is in that the opening angle of a growing stable crack (tgα) will decrease with low-

ering of the ductile properties of the material. Consequently, it will lead to greater length of the extending crack in the case of reduction of the uniform component of metal plastic deformation  $\varepsilon_t$ .

Influence of plastic deformation on the change of  $KCV_{\max}$  characteristics of specimens cut out in the transverse direction to that of deformation, and  $\sigma_{0.2}$ ,  $\sigma_t$  was studied earlier [6], in the case of 09G2S steel. As follows from work [6], prior deformation of metal greatly lowers the value of impact toughness  $KCV_{\max}$  on the upper shelf and increases the brittle-ductile transition temperature ( $T_{\text{bdt}}$ ) at a slight change of tensile strength  $\sigma_t$  of the studied steels.

In order to perform a more detailed study of the possible impact of accumulated residual deformation in the pipeline on the change of impact toughness of Charpy specimens in the longitudinal and circumferential directions, a full-scale specimen was prepared from a 630×8 mm pipe under PWI laboratory conditions. By its design the specimen consisted of a pipe section and two flat covers (made in-house) of the dimensions, which allowed applying static loading by hydraulic pressure up to fracture. In order to ensure satisfactory conditions for specimen welding and to prevent fracture from appearance of a zone of irreversible deformations during testing, the cover was fitted by welded-on coils of the same diameter, as that of the pipe. For this purpose, one coil 100–120 mm wide was cut from each of the end faces (A and B) of the pipe (Figure 1).

The main objective of conducting hydraulic testing was development of deformed sections in the full-scale specimen metal in the pipe, as a result of testing, for their further study.

Characterization of the specimen components:

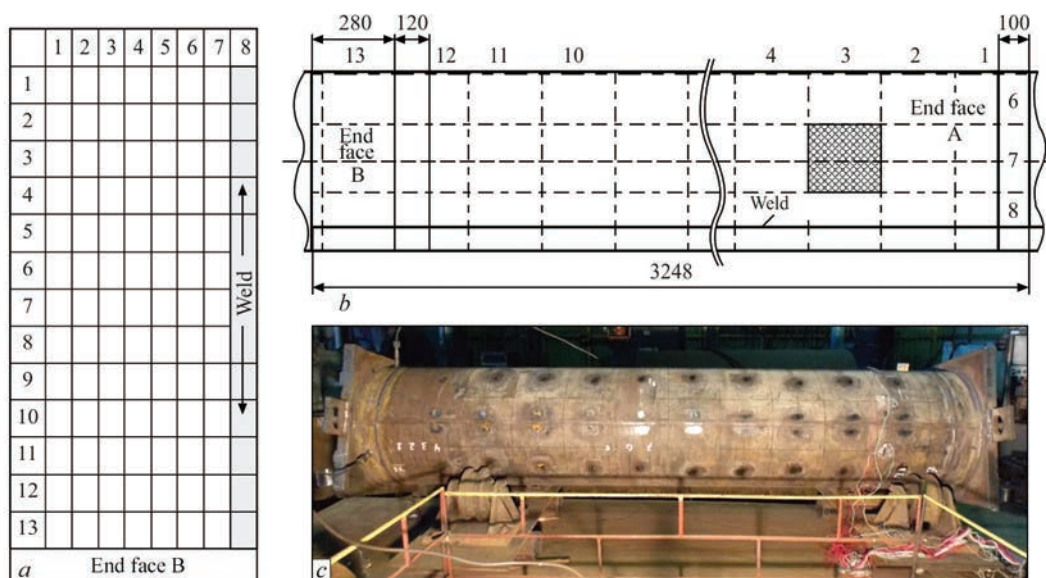


Figure 1. System of marking the measured points (a, b); marked full-scale specimen (c)



Figure 2. General view of the cover

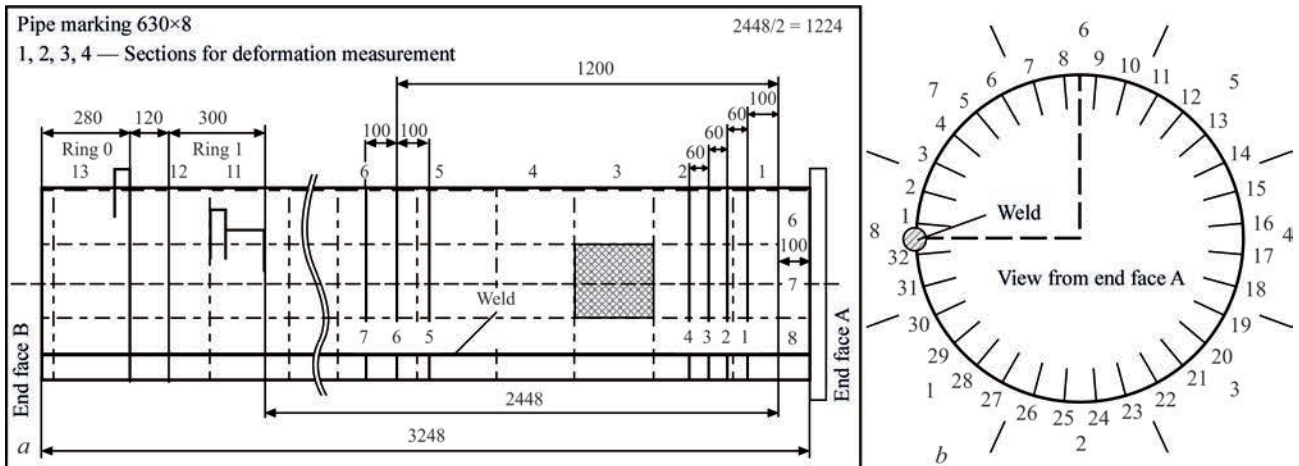


Figure 3. Marking for measurement of residual deformations: *a* — sections 1–7; *b* — points 1–32 for marking the measured bases

- electrically welded straight seam 630×8 pipe to GOST 10705 and GOST 10701 after service; inner and outer surfaces had corrosion damage, wall thickness measured by TUZ-3 thickness meter was 6.9–7.6 mm, length was 2970 mm, and material was 17G1S;

- flat welded cover (2 units) made in-house from sheet steel St20 50 mm thick with 30 mm thick stiffeners in the quantity of 6 pcs (Figure 2).

To study the changes of geometrical parameters (residual deformation), a system of marking the points and sections was applied on the pipe surface in the ini-

tial state, in which the measurements were taken. The end faces of the full-scale specimen were marked as A and B. The pipe surface was divided into 8 longitudinal bands and 13 rings, at the intersection of which cylindrical sectors of 247.78×247.78 mm size were formed (Figure 3). A ring («ring 0») was cut out of the pipe before specimen welding to study the pipe metal in undeformed state.

In order to reach maximum deformations, the pipe specimen was brought to destruction by hydraulic testing (Figure 4).

After completion of testing for plastic deformation, measurements of the full-scale specimen were taken by nondestructive testing methods (Table 1).

Metal from the specimen middle part, where maximum plastic deformation was observed, was used to make specimens for destructive kinds of testing (see Table 1, specimen fragment is shown by black drawing).

Investigations were conducted on specimens, made in the axial and circumferential directions. Figure 5 shows specimen layout and notch position.

Specimens were cut out of an undeformed fragment of the pipe («ring 0») and deformed fragment of the pipe, shown in Table 1.

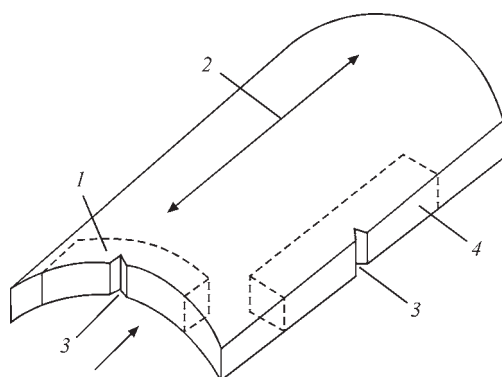
24 Charpy specimens were made for each direction of the above-mentioned fragments. Specimens for the wrought case were subjected to natural ageing for 40 days.



Figure 4. General view of the site of fracture in a pipe reference specimen after hydraulic loading by pressure 13.25 MPa

**Table 1.** Distribution of residual deformation (%) in the circumferential direction after hydraulic loading of the pipe in the zone of cross-sections 1–4 and 5–7 ( $l_0 = 61.00$  mm)

Sector	Area	Points	(← End face A) Sections (End face B →)						
			1	2	3	4	5	6	7
8	1	1–2	2.85	3.03	3.74	3.69	3.36	4.39	4.51
	2	2–3	3.13	3.39	3.70	3.62	3.61	4.23	4.02
7	3	3–4	3.13	3.75	3.23	3.85	T 3.56	P 3.51	4.13
	4	4–5	2.85	3.03	3.64	3.84	3.43	3.67	4.11
	5	5–6	2.90	2.77	2.69	3.07	3.03	3.36	3.30
6	6	6–7	3.03	3.02	3.39	2.84	3.23	3.82	P 3.64
	7	7–8	3.33	3.15	3.84	4.31	3.92	3.80	3.75
	8	8–9	3.13	3.15	3.16	3.13	2.87	3.92	3.41
	9	9–10	2.56	2.49	2.44	2.33	3.20	3.20	2.97
5	10	10–11	2.49	2.41	2.36	2.31	3.07	3.00	2.84
	11	11–12	1.93	2.84	2.80	3.03	2.54	2.49	2.90
	12	12–13	1.90	2.08	2.05	2.28	2.03	2.59	2.25
	13	13–14	1.49	1.77	1.61	1.75	1.54	2.16	2.28
4	14	14–15	1.92	1.26	1.72	1.66	1.64	2.59	2.77
	15	15–16	2.00	1.89	2.56	2.49	2.66	2.80	2.80
	16	16–17	2.33	2.28	2.69	2.69	2.67	2.67	3.18
3	17	17–18	0.97	1.16	1.77	1.70	1.57	2.33	1.46
	18	18–19	0.77	0.67	0.69	0.72	0.67	1.41	0.80
	19	19–20	1.69	1.90	2.10	2.26	1.92	2.67	2.56
	20	20–21	2.11	2.87	3.36	3.26	2.49	2.41	2.72
2	21	21–22	2.44	2.31	2.66	2.34	2.90	P 3.05	P 3.03
	22	22–23	1.92	2.28	1.87	1.59	K 2.66	K 2.87	2.80
	23	23–24	1.92	2.07	2.48	2.70	2.33	H 2.05	2.02
	24	24–25	2.44	3.05	3.46	4.39	2.54	H 3.18	2.97
1	25	25–26	2.74	3.34	3.69	3.57	3.79	3.74	3.64
	26	26–27	2.98	3.15	2.82	3.13	H 3.43	H 4.30	3.38
	27	27–28	2.54	2.26	2.89	3.52	H 2.28	H 3.43	3.05
8	28	28–29	2.92	3.64	3.21	3.59	3.33	4.21	3.90
	29	29–30	3.36	3.13	3.03	3.43	3.38	3.79	3.64
8	30	30–31	2.82	2.74	2.77	2.80	2.52	2.70	2.69
	31	31–32	2.80	3.07	3.69	3.62	3.46	3.95	3.67
Average	%		2.41	2.57	2.76	2.88	2.76	3.16	3.06



**Figure 5.** Location of specimens and position of the notch in Charpy impact specimen (KCV) in the pipe: 1 — general view of welded specimens cut out in the circumferential direction; 2 — direction of pipe longitudinal axis; 3 — orientation of V-shaped notch; 4 — general view of impact specimens, cut out in the axial direction. Size of axial specimens  $10.0 \times 6.9 \pm 0.1$  mm — treated; for transverse specimens —  $10.0 \times 7.1$  mm — untreated

Figure 6 shows the general view of the specimens made in the axial and circumferential directions.

Impact out-of-plane bending tests were conducted in the temperature range from  $-60$  to  $40$  °C.

Results of testing specimens, made from an undeformed pipe fragment («ring 0»), are shown in Table 2 and in Figure 7.



**Figure 6.** General view of impact specimens for the circumferential and axial directions

**Table 2.** Results of testing Charpy impact specimens, made from an undeformed pipe fragment

Number	Circumferential direction					Axial direction				
	$B$ , mm	$H_1$ , mm	$F$ , mm <sup>2</sup>	$t$ , °C	KCV, J/cm <sup>2</sup>	$B$ , mm	$H_1$ , mm	$F$ , mm <sup>2</sup>	$t$ , °C	KCV, J/cm <sup>2</sup>
1	7.46	8.25	61.55	-40	38.18	6.94	8.12	56.35	-40	47.03
2	7.46	8.25	61.55	-40	28.76	6.94	8.23	57.12	-40	66.88
3	7.38	8.28	61.11	-40	24.87	6.94	8.20	56.91	-40	41.29
4	7.44	8.14	60.56	-20	28.90	6.94	8.22	57.05	-20	72.22
5	7.42	8.35	61.96	-20	27.76	6.94	8.22	57.05	-20	67.84
6	7.43	8.30	61.67	-20	30.16	6.94	8.20	56.91	-20	70.64
7	7.38	8.35	61.62	0	55.66	6.94	8.24	57.19	0	111.38
8	7.40	8.35	61.79	0	44.51	6.94	8.20	56.91	0	119.84
9	7.42	8.32	61.73	0	40.01	6.94	8.28	57.46	0	126.35
10	7.45	8.16	60.79	+20	66.13	6.94	8.18	56.77	+20	150.26
11	7.44	8.29	61.68	+20	67.93	6.94	8.16	56.63	+20	138.27
12	7.45	8.27	61.61	+20	65.25	6.94	8.24	57.19	+20	130.09
13	7.49	8.23	61.64	+40	66.52	6.94	8.20	56.91	+40	140.92
14	7.42	8.15	60.47	+40	66.81	6.94	8.28	57.46	+40	129.66
15	7.47	8.36	62.45	+40	67.09	6.94	8.30	57.60	+40	126.91
16	7.40	8.32	61.57	-60	14.34	6.94	8.18	56.77	-60	45.80
17	7.48	8.24	61.64	-60	18.30	6.94	8.18	56.77	-60	13.48
18	7.46	8.30	61.92	-60	9.50	6.94	8.12	56.35	-60	29.94

**Table 3.** Results on mechanical properties of an undeformed pipe fragment

Characteristics	Undeformed fragment («ring 0»)	
	In the axial direction	In the circumferential direction
Yield limit $\sigma_{0.2}$ , MPa	410–410	490–494
Tensile strength $\sigma_t$ , MPa	568–581	591–593
Relative elongation $\delta_5$ , %	24.9–26.9	21.3–22.3

Table 3 gives the results of tensile mechanical testing of specimens made from an undeformed pipe fragment.

As is easily seen from Figure 7, the pipe wall metal has a considerable anisotropy of impact toughness properties in the circumferential and axial directions, that is indicative of low resistance of this material to crack growth in the axial direction.

In addition, a considerable difference of brittle-ductile transition temperatures is observed for the

axial and circumferential directions determined by 30 J/cm<sup>2</sup> criterion.

So, for the axial direction this temperature is approximately -48 °C, while for the circumferential direction it is -15 °C.

Considering that the temperature of brittle-ductile transition ( $T_{bdt}$ ) at plastic deformation of metal shows a tendency to grow, with accumulation of plastic deformations of metal it may lead to  $T_{bdt}$  shifting to the plus temperature region in individual pipe areas. Consequently, it may lead to considerable decrease of service properties of pipe metal.

In order to solve this problem, Table 4 and Figure 8 give the results of testing Charpy impact specimens, made from a fragment of a pipe ring, which was exposed to plastic deformation of approximately 3.5 % (see Table 1).

Figures 9, 10 give comparative graphs of the results of testing Charpy impact specimens, made from undeformed and deformed (3.5 %) pipe fragments.

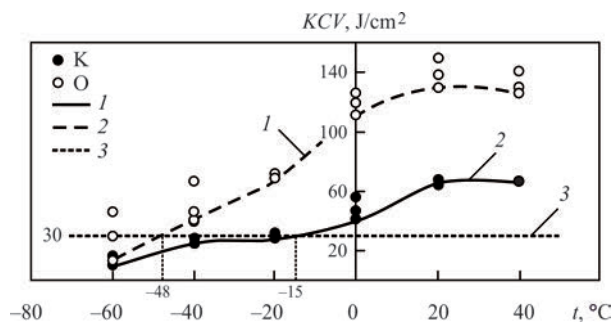


**Figure 7.** Temperature dependence of impact toughness of Charpy specimens oriented in the circumferential (K) and axial (O) directions for undeformed pipe metal: 1 — curve by minimum values for circumferential specimens; 2 — curve by minimum values for axial specimens; 3 — 30 J/cm<sup>2</sup> level

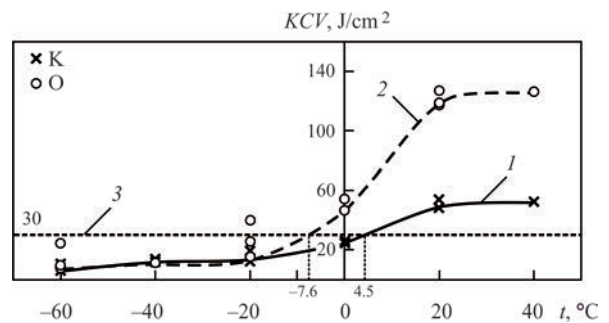


**Figure 8.** Temperature dependence of impact toughness of Charpy specimens oriented in the circumferential (K) and axial (O) directions for deformed pipe metal: 1 — curve by minimum values for circumferential specimens; 2 — curve by minimum values for axial specimens; 3 — 30 J/cm<sup>2</sup> level

**Table 4.** Results of testing impact specimens made from pipe specimen fragment deformed by 3.5 %

Number	Circumferential direction					Axial direction				
	<i>B</i> , mm	<i>H</i> <sub>1</sub> , mm	<i>F</i> , mm <sup>2</sup>	<i>t</i> , °C	<i>KCV</i> , J/cm <sup>2</sup>	<i>B</i> , mm	<i>H</i> <sub>1</sub> , mm	<i>F</i> , mm <sup>2</sup>	<i>t</i> , °C	<i>KCV</i> , J/cm <sup>2</sup>
1	7.1	8.0	56.80	-60	7.75	6.88	8.06	55.45	-60	24.71
2	7.1	8.06	57.23	-60	7.71	6.86	8.0	54.88	-60	10.71
3	7.1	8.0	56.80	-60	5.35	6.87	8.03	55.17	-60	6.58
4	7.0	7.92	55.44	-40	12.03	6.85	7.95	54.46	-40	11.70
5	7.15	8.03	57.41	-40	13.83	6.86	8.07	55.36	-40	10.46
6	7.1	8.15	57.87	-40	12.37	6.86	8.07	55.36	-40	11.51
7	7.0	7.9	55.30	-20	13.29	6.86	8.05	55.22	-20	40.02
8	7.1	7.9	56.09	-20	24.43	6.86	8.12	55.70	-20	13.20
9	7.0	8.06	56.42	-20	19.14	6.86	8.06	55.29	-20	25.14
10	7.05	7.93	55.91	0	25.04	6.86	8.13	55.77	0	54.15
11	7.1	7.95	56.45	0	26.40	6.86	8.08	55.43	0	46.91
12	7.0	8.02	56.14	0	26.18	6.87	8.0	54.96	0	47.31
13	7.1	8.2	58.22	+20	48.78	6.88	8.1	55.73	+20	117.89
14	7.1	8.06	57.23	+20	54.69	6.88	7.91	54.42	+20	119.44
15	7.1	8.1	57.51	+20	49.21	6.85	8.05	55.14	+20	127.49
16	7.1	8.06	57.23	+40	52.25	6.86	8.03	55.09	+40	127.25
17	7.1	8.0	56.80	+40	52.64	6.86	8.07	55.36	+40	125.72
18	7.0	8.04	56.28	+40	53.13	6.88	8.16	56.14	+40	127.18

As one can see from Figures 9 and 10, after deformation of pipe metal by 3.5 % in the circumferential direction a considerable shift of brittle-ductile transition temperatures determined by 30 J/cm<sup>2</sup> criterion, is observed for the axial and circumferential directions. In this case, the shift of brittle-ductile transition temperatures for the axial and circumferential directions was assessed by minimum values of impact toughness of Charpy specimens. It should be also noted that specimens cut out in the axial direction are more sensitive to the effect of pipe metal plastic deformation in the circumferential direction (3.5 % of plastic deformation) on the general change of brittle-ductile transition temperature, than those cut out in the circumferential direction. So, the given graphs of the dependence of impact toughness of Charpy specimens on testing temperature show that the total shift of brittle-ductile transition temperatures is equal to 40 °C for the axial direction and about 20 °C for the circumferential di-

rection. At the same time, the brittle-ductile transition temperature, which was determined on the specimens in the circumferential direction, is much higher than that for specimens in the axial direction. Moreover, in the ductile condition a drop of impact toughness of the Charpy specimens is observed for the circumferential direction at pipe deformation by 3.5 % during hydraulic loading, that is absent in specimens in the axial direction (see Figures 9, 10).

The latter case completely confirms the validity of the proposed approach to lowering of the characteristics of brittle and tough fracture resistance of pipeline metal under the impact of strain ageing.

From the above results it should be noted that testing of Charpy specimens cut out in the direction of pipeline axis, leads to considerable error in assessment of pipeline material resistance to brittle and quasibrittle fracture. So, at assessment of transition temperature by specimens of 30 J/cm<sup>2</sup> impact toughness

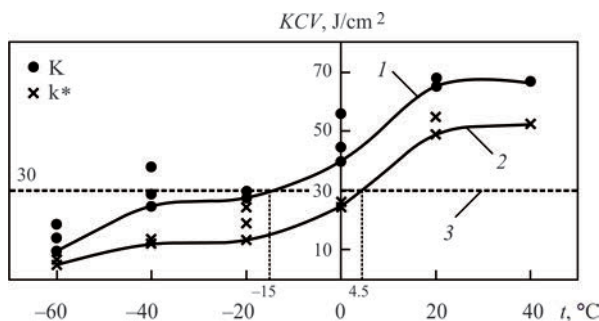


**Figure 9.** Temperature dependence of impact toughness of Charpy specimens oriented in the circumferential direction for undeformed (K) and deformed (K\*) pipe metal: 1 — curve by minimum values for specimens for undeformed metal; 2 — for deformed metal; 3 — 30 J/cm<sup>2</sup>

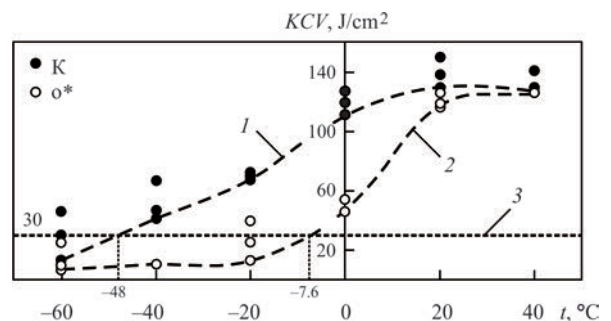


**Figure 10.** Temperature dependence of impact toughness of Charpy specimens oriented in the axial direction for undeformed (O) and deformed (o\*) pipe metal: 1 — curve by minimum values for specimens for undeformed metal; 2 — for deformed metal; 3 — 30 J/cm<sup>2</sup> level

for an undeformed pipe, the error is more than 40 °C. More over, the ductile fracture resistance ( $KCV_{max}$ ) of the material in the axial and circumferential directions differs by almost two times that only worsens the assessment (see Figures 7, 8).

The same tendency is also in place for pipe deformation by 3.5 % in the circumferential direction, where at assessment of the transition temperature by impact toughness specimens at 30 J/cm<sup>2</sup>, the error is more than 12 °C at more than two times decrease of material ductile fracture resistance ( $KCV_{max}$ ). In this case, increase of  $\sigma_{0.2}$  yield limit is not even taken into account.

Obtained conclusions can be useful for assessment of the welded joint HAZ resistance to brittle and quasi-brittle fracture in pipelines.

**Conclusions**

1. Plastic deformation of pipeline wall can significantly lower the ductile fracture resistance characteristics ( $\delta_p, tg\alpha, KCV, \epsilon_p, T_{bdt}$ ) even at relatively low values of plastic deformation in its local regions. So, for instance, for 17G1S steel 7.0 mm thick the error is more than 12 °C, at assessment of transition temperature by impact toughness specimens at 30 J/cm<sup>2</sup> for a pipe with 3.5 % deformation.

2. Determination of the temperature of brittle-ductile transition by minimum values of impact toughness of Charpy specimens for axial direction does not correspond to the real state and is seriously underestimated, compared to specimens made in the circumferential direction. So, for instance, for 17G1S steel 7.0 mm thick, at assessment of transition temperature by impact toughness specimens at 30 J/cm<sup>2</sup> for an undeformed pipe, the error is more than 30 °C.

3. Obtained conclusions can be useful for assessment of welded joint resistance to brittle and quasi-brittle fracture of pipelines.

1. Babich, V.K., Gul, Yu.P., Dolzhenkov, I.E. (1972) *Strain ageing of steel*. Moscow, Metallurgiya [in Russian].

2. Paton, B.E., Semenov, S.E., Rybakov, A.A. et al. (2000) Ageing and procedure of evaluation of the state of metal of the main pipelines in service. *The Paton Welding J.*, **7**, 2–10.

3. Girenko, V.S., Semenov, S.E., Goncharenko, L.V. (2001) Strain ageing of pipe steels. *Tekh. Diagnost. i Nerazrush. Kontrol*, **3**, 32–35.

4. Pashkov, Yu.I., Anisimov, Yu.I., Lanchakov, G.A. et al. (1996) Prediction of residual strength limit of main gas and oil pipelines taking into account the operating time. *Stroitelstvo Truboprovodov*, **2**, 2–5 [in Russian].

5. Pashkov, Yu.N. (1996) *Crack resistance of welded pipes for gas pipelines*: Syn. of Thesis for Dr. of Tech. Sci. Degree. Moscow [in Russian].

6. Dyadin, V.P. (2007) Influence of pre-deformation on impact toughness of Charpy sample in fracture. *The Paton Welding J.*, **1**, 22–26.

7. Zolotarevsky, V.S. (1998) *Mechanical properties of metals*. Moscow, MISIS [in Russian].

8. Mochernyuk, N.P., Krasnevsky, S.M., Lazarevich, G.I. et al. (1991) Influence of operating time of main gas pipeline and working gas pressure on physical-mechanical characteristics of pipe steel 19G. *Gazovaya Promyshlennost*, **3**, 34–36 [in Russian].

9. Gumerov, A.G. (1998) *Defectiveness of oil pipelines and methods of their repair*. Moscow, Nedra [in Russian].

10. (1967) *Structure and mechanical properties of metals*. Moscow, Metallurgiya [in Russian].

11. Gafarov, N.A., Goncharov, A.A., Kushnarenko, V.M. (1998) *Corrosion and protection of hydrogen sulfide-containing oil and gas fields*. Moscow, Nedra [in Russian].

12. Girenko, V.S., Dyadin, V.P. (1990) Correlation of crack resistance characteristics of materials and welded joints with results of standard mechanical tests. *Avtomatch. Svarka*, **6**, 1–4 [in Russian].

13. Siratori, M., Miesi, T., Mitsushima, H. (1986) *Computational fracture mechanics*. Moscow, Mir [in Russian].

14. Phaal, R., Madnald, K.A., Brown, P.A. (1993) *Correlations between fracture toughness and Charpy impact energy*. Doc. 5605/7/93.

15. Girenko, V.S., Dyadin, V.P. (1985) Dependencies between impact toughness and fracture mechanics criteria  $\delta_{ic}, K_{Ic}$  of structural steels and their welded joints. *Avtomatch. Svarka*, **9**, 14–22 [in Russian].

16. Dyadin, V.P. (2010) Evaluation of temperature shift depending upon the specimen thickness by the force and deformation criteria of fracture mechanics. *The Paton Welding J.*, **4**, 14–21.

17. Troitskii, V.A., Dyadin, V.P. (2011) Selection of control sections of the main pipelines for diagnostic examination. *Tekh. Diagnost. i Nerazrush. Kontrol*, **3**, 5–11 [in Russian].

Received 25.06.2021

**SEPTEMBER 9, 2013** Las Vegas High Roller amusement ride of 168 m was opened in the USA. The observation wheel is the fantastic fulfillment of achievements of machine-building and design as well as world record-holder in height. New amusement ride is equipped with 28 cabins of 6 meters diameter, each of which can include up to 40 people. External rim of «High Roller» wheel was welded from two tubular steel beam of inch thickness, then they were joined in groups of four on four beams forming rim section. Each of these elements then were joined and as a result an external wheel rim was obtained. Supporting structures were designed and constructed in the same way in order to carry tremendous load of the wheel.



**SEPTEMBER 10, 1957** Plasma cutter was patented. Plasma cutting was invented in 1954 in a laboratory of Linde department of Union Carbide Company. Young scientist Robert Gage found that TIG arc passed through small diameter nozzle significantly rises its intensity and temperature. Passing through this focused arc sufficiently large gas flow, he discovered that such arc can be used for metal cutting. Arc temperature, reaching more than 24000 K, melts metal and intensive air flow blows out molten metal for cutting. Since gas in arc was in overheated state, called plasma, this process was named plasma cutting.



## MODELING OF THE PROCESS OF INDUCTION HEAT TREATMENT OF WELDED JOINTS FROM RAIL HIGH-STRENGTH STEELS

**R.S. Hubatyuk, S.V. Rymar, O.S. Prokofiev, V.A. Kostin, O.V. Didkovskiy and E.V. Antipin**

E.O. Paton Electric Welding Institute of the NAS of Ukraine

11 Kazymyr Malevych Str., 03150, Kyiv, Ukraine. E-mail: [office@paton.kiev.ua](mailto:office@paton.kiev.ua)

The selection of technological parameters of the heat treatment process, which provides the necessary structural and phase transformations of rail welded joint, is a very expensive process that requires a large number of experiments with a significant consumption of power, time, labor and financial resources. The paper proposes the method of mathematical and physical modeling of thermal processes to determine the optimal parameters of heat treatment of rail welded joint on model specimens based on the theory of similarity, taking into account the interrelated properties and physical phenomena with the original study. The solutions obtained during realization of this method provide a considerable reduction of resources at determination of optimum modes of heating of products from high-strength carbon steels, in particular, rails. Based on the scale factors of criteria of electromagnetic and thermal similarity, a mathematical model of the induction system for numerical calculation of propagation of electromagnetic and thermal fields was developed. The finite element method was used, which represents a tool for combining integral characteristics with the values of vector characteristics of the studied electromagnetic fields. The dependence of physical properties of materials on temperature was taken into account. In the course of parametric study, the parameters and configuration of the «inductor–product» system were determined and the space-time distribution of the temperature field during heat treatment modeling was determined. The obtained data of numerical calculation should be used during physical modeling of optimization of the modes of heat treatment of the sample and will significantly reduce the number of experiments to determine the effect of thermal heating on phase transformations and mechanical properties of steel in the zone of welded joint. 18 Ref., 2 Tables, 9 Figures.

*Key words:* induction heating, heat treatment, welded joint of railway rails, mathematical modeling, similarity theory

At present, laying of continuous tracks is performed at construction and reconstruction of the main railways. This is due to the general tendency of increase of rolling stock speed, particularly for high-speed passenger trains, increased traffic intensity and traffic density. In order to ensure a higher reliability and operational durability of the rails, new generation high-strength rail steels with higher carbon content are used, when laying the continuous tracks [1].

At construction of the railway tracks, high-strength rails are joined by welding their end faces. The joints are mostly made by flash-butt welding process developed at PWI [2], or automatic electric arc fusion welding. World experience shows that in the removed defective rails the weld is the region, where up to 30 % of defects are observed. Although defects in the weld are not predominant, they deserve close attention at control of the rail track quality. Inhomogeneity of the metal microstructure is found in the welded joint zone, and unfavourable residual stresses are observed, which create the conditions for formation of internal

defects, weakening the rail section with the weld. The HAZ of the rail welded joint has different sections, characterized by the presence of soft metal layers on the rail rolling surface and layer of lower ductility and toughness, more prone to brittle fracture, compared to the rail base metal.

Higher carbon content cardinaly changes the steel weldability. In terms of one of the main indices of steel weldability, namely carbon equivalent  $C_e$ , the rail steel is close to the high-strength medium-alloyed steels with 0.30–0.45 % carbon content. The values of carbon equivalent for these steels are approximately the same:  $C_e = 0.8–1.0$  %. It points to the fact that by the weldability criterion the current high-strength rail steels belong to satisfactory ones, i.e. to those which require special welding modes and technological measures, without which it is impossible to ensure the integrity and quality of the welded joint [1].

One of such measures is heat treatment (HT) of the rail welded joint, which minimizes the consequences of the high-temperature heating of metal during weld-

R.S. Hubatyuk — <https://orcid.org/0000-0002-0851-743X>, S.V. Rymar — <https://orcid.org/0000-0003-0490-4608>,

O.S. Prokofiev — <https://orcid.org/0000-0003-4643-6611>, V.A. Kostin — <https://orcid.org/0000-0002-2677-4667>,

O.V. Didkovskiy — <https://orcid.org/0000-0001-5268-5599>, E.V. Antipin — <https://orcid.org/0000-0003-3297-5382>

© R.S. Hubatyuk, S.V. Rymar, O.S. Prokofiev, V.A. Kostin, O.V. Didkovskiy and E.V. Antipin, 2021

ing, refines its microstructure, increases the welded joint strength, and relieves residual stresses. HT application has a positive impact on the service life of the rail butt joint [3].

**Purpose and objectives of the study.** The purpose and objectives of the study is development of a mathematical model for numerical modeling of the process of high-frequency induction heating of a model sample from high-carbon high-strength rail steel with a welded joint with determination of the parameters and configuration of «inductor–product» system for further performance of a real induction HT of a model sample, as well as determination of space-time distribution of the temperature field during HT performance.

Here, in order to shorten the time for calculation, it is rational to divide the mathematical modeling process into two stages: first — modeling of the process of high-frequency induction heating of «inductor–product» system; second — modeling of the structure of phase transformations and properties of the weld metal in the product, depending on the thermal cycle.

The following objectives were defined, in order reach the purpose:

- develop the concept of physical modeling of induction HT of welded joints of high-strength railway rails on model samples;
- using the physical model as a basis, develop a mathematical model for numerical calculation of induction heating of a model sample with the welded joint from high-strength rail steel;
- develop a mock-up and perform experimental studies on physical modeling of induction heating of a model sample.

**Analysis of published data and problem definition.** Analysis of application of computational models of induction heating systems shows wider application of numerical modeling methods when solving the problems of optimization of technological parameters of HT process. Numerical modeling of induction systems enabled studying not only individual aspects of electromagnetic and thermal field propagation, but also the accompanying phenomena and processes, such as stress-strain state and structural transformations of metal, and developing multiphysics models, taking into account the inextricable connection between these processes and physical phenomena.

In work [4] at development of a mathematical model of an induction heating system methods of induction system analysis are proposed, which enable consistently taking into account the nonlinear dependencies of thermophysical properties of the metal being heated, and in [5] the method of parametric optimization with distributed parameters was used.

However, here the transformations in steel when exceeding the temperature of magnetic transformation points are ignored, that introduces an error at calculation of energy characteristics of the studied induction system.

In [6, 7] at development of a numerical model of induction heating of bodies of different cross-section with inhibition of the edge and end effects, a more uniform temperature field in the billet is achieved through application of the technological measures of changing the number of inductor sections, current frequency, different designs of magnetic concentrators, regulation of the speed of billet movement, etc. Here, the dependence of the billet magnetic permeability either on temperature, or on the magnetic field intensity is not taken into account.

Induction heating models from works [8, 9] use temperature-dependent  $B-H$  curves, nonlinear dependencies of the material thermophysical properties and change of phase transformation during sample heat treatment at rapid heating and cooling. Used as the model sample material is base metal of the studied object, homogeneous over the entire cross-section, which was not subjected either to thermal or to mechanical impact before that. Modeling is performed on samples in keeping with the normative standards or samples of an arbitrary shape and geometrical dimensions without indicating the criteria for selection of a particular parameter that influences the accuracy of the obtained results at transition from physical modeling on model samples to real objects and real technological process.

In view of the fact that the modern technologies of induction HT are not always optimal and do not allow fully obtaining the required characteristics of metal in the zone of rail welded joints [1], it becomes necessary to perform further investigations and study the features of phase transformations in the rail welded joint after HT. Performance of high-quality HT requires refining the modes and optimizing the parameters, influencing the heating processes, conducting a large scope of costly research on the effect of heating rates, soaking and cooling time on the features of structure formation in the welded joint zone. Solving this kind of problems requires an integrated approach that includes rational application of mathematical and physical modeling methods for investigations, and determination of key parameters of HT process. It is urgent and rational to solve such a problem first by modeling on small model samples of rail steel welded joints. For this purpose it is necessary to develop on the base of the theory of similarity the mathematical model of HT process of model samples, taking into account the interrelated properties and physical phe-

nomena with the studied original. A small model sample can be used to optimize the heating modes and to study the properties of the treated weld metal, which is followed by transition to refining the modes of HT of a butt welded joint of a real rail [10]. The proposed approach enables greatly reducing the resources used at determination of optimum modes of heating products from high-strength carbon steels, in particular, rails. Developed models of induction HT process will allow optimizing the inductor design to ensure the required temperature field in the zone of the welded joint of the object being heated, and it allows a more effective performance of HT process.

**Methodology and methods of investigation of the induction system.** At induction heating the electromagnetic and thermal processes are interrelated, and they are described by nonlinear differential equations, which cannot be solved analytically. This kind of problems can be solved only by numerical methods. The finite element method is extensively used for modeling the induction heating systems. This method is a tool for correlating the integral characteristics with the values of vector characteristics of the studied fields. The problem of induction heating modeling belongs to multiphysics problems that involve interrelated calculations of propagation of the electromagnetic and thermal fields [11].

At temperature variation in a broad range it is important to take into account also the change of physical properties of the materials, as it has a significant impact on the electromagnetic and thermal characteristics of «inductor-product» system. For correct solution by mathematical modeling of the process of induction HT, and in order to solve the interrelated problems of propagation of the electromagnetic and thermal fields it is rational to use multiphysics software packages of finite element analysis, for instance Comsol Multiphysics.

The object of study is «inductor-product» induction system, which consists of a cylindrical multiturn inductor that covers a cylindrical sample in the form of a solid rod from high-strength rail steel with increased carbon equivalent that has a transverse welded joint.

*Introduced simplifications.* The complex shape of the rail cross-section and different weight and size parameters of the rail main parts do not allow performing mathematical modeling of the process of induction HT in the two-dimensional or axisymmetric definition of the problem, but only in 3D formulation that requires considerable computational resources and quite considerable computer time. In order to obtain a faster evaluation result of mathematical and physical modeling of the process of induction heating

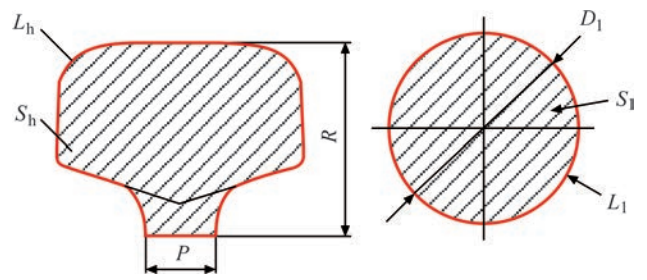


**Figure 1.** Transverse sections of the rail head and the solid cylindrical rod, which replaces it

of the rail butt welded joint, it was proposed to reduce the rail cross-section to a simpler form and to separately study induction heating of the main rail elements — head, web and foot. Here, these elements are replaced by simple figures: solid (for the head) and hollow (for the web and foot) cylindrical rods with equal parameters, surface areas and weights of the rail and rod elements. More over, in order to simplify physical modeling of the heating, these simple figures can be further reduced, by applying the similarity theory [12, 13].

As an example, let us consider the rail head, which is the most prone to dynamic loads, wear of the rolling surface and is susceptible to initiation of defects and cracks in the transverse weld zone. The head contains layers of hardened, transition and base metal.

The cross-section of the rail head in Figure 1 is presented in the form of a solid cylindrical rod of diameter  $D_1$ , perimeter  $L_1$  and area  $S_1$ , which are equal to the perimeter of the heating zone under the inductor of head  $L_h$  and head area  $S_h$ . Such a geometrical transformation allows preserving the weight and size parameters of the head and the rod, and ensures correct results of physical modeling. In the site of the anticipated axial section  $P$  of the rail a condition is accepted that the temperature of this region is the same as that of the head surface and no heat removal occurs in this direction.

The criteria of geometrical, and electrodynamic similarity and similarity of thermal processes allow determination of the parameters of the mathematical and physical model, geometrical dimensions of a cylindrical sample with a transverse welded joint, and frequency of inductor supply current. The geometrical parameters of the inductor are determined when solving this problem.

To simplify further physical modeling of induction heating, we will reduce the overall dimensions of the cylindrical full-scale rod shown in Figure 1, to a model rod, introducing scale factors into consideration [13, 14].

*Scale factors, similarity of electromagnetic processes.* For induction system under consideration, we will assume the scales of magnetic induction  $m_B$ , mag-

netic permeability  $m_\mu$  of steel, magnetic field intensity  $m_h$  and specific electric resistance  $m_\rho$  of full-scale 1 and model 2 rods to be equal to a unity that is valid in the case of using steel with the same electrophysical characteristics:

$$\begin{aligned} m_B &= \frac{B_1}{B_2} = 1, & m_\mu &= \frac{\mu}{\mu_2} = 1, \\ m_H &= \frac{H_1}{H_2} = 1, & m_\rho &= \frac{\rho_1}{\rho_2} = 1, \end{aligned} \quad (1)$$

where  $B_1, B_2; \mu_1, \mu_2; H_1, H_2; \rho_1, \rho_2$  are the magnetic induction, magnetic permeability, magnetic field intensity and specific electric resistance in the full-scale and modeled rods, respectively, which are accordingly equal to each other.

We will assume the following main linear  $l$  geometrical dimensions: diameters of full-scale and model cylindrical rods  $d_1, d_2$ ; length of magnetic lines of force in the rods under the inductor  $l_1, l_2$  (close to inductor length in the considered models); depth of penetration of magnetic fluxes and induced currents in the rod  $\Delta_1, \Delta_2$ . The scale of linear dimensions  $m_l$ , equal to the ratio of the mentioned geometrical dimensions, will be equal to:

$$m_l = \frac{d_1}{d_2} = \frac{\Delta_1}{\Delta_2} = \frac{l_1}{l_2}. \quad (2)$$

Depth of penetration of the induced currents in the full-scale and model rods for steel is [15]:

$$\Delta_{1,2} = \frac{1}{k_R} \sqrt{\frac{2\rho}{\pi f_{1,2} \mu_0 \mu_r}}, \quad (3)$$

where  $k_R \approx 1.4$  is the coefficient of reduction of penetration depth for a ferromagnetic medium;  $f_1, f_2$  are the frequencies of induced currents in the full-scale and model rods;  $\mu_0 = 4\pi \cdot 10^{-7}$  H/m is the magnetic constant;  $\mu_r$  is the relative value of the steel magnetic permeability. For nonferromagnetic steel, which lost its magnetic properties, when its temperature rose above the Curie point (approximately 740 °C),  $k_R = 1$  and  $\mu_r = 1$ .

Having divided  $\Delta_1$  by  $\Delta_2$ , using expressions (1)–(3), we will have:

$$m_l = \frac{\Delta_1}{\Delta_2} = \sqrt{\frac{f_2}{f_1}} = \frac{1}{\sqrt{m_f}}, \quad (4)$$

where  $m_f$  is the scale of current frequency.

$$m_l = \frac{f_1}{f_2} = \frac{1}{m_f^2}, \quad (5)$$

Time is inversely proportional to frequency  $t \sim 1/f$ . Thus, the time scale per one period of current oscillation  $m_t$ , allowing for expression (5), will be equal to:

$$m_t = \frac{t_1}{t_2} \sim \frac{f_2}{f_1} = \frac{1}{m_f} = m_l^2. \quad (6)$$

In keeping with the law of electromagnetic induction, the voltage in the full-scale and model cylindrical rods (in the first approximation) is:

$$U_{1,2} = 2\pi f_{1,2} B_{1,2} S_{1,2}, \quad (7)$$

where  $S_1, S_2$  are the cross-sectional areas through which the magnetic flux passes in the rods. At high frequencies

$$S_{1,2} = \pi k_d d_{1,2} \Delta_{1,2}, \quad (8)$$

where  $k_d$  is the coefficient of reduction of the rod diameter, approximately by the depth of the magnetic flux penetration. This coefficient is the same for both the rods.

The voltage scale  $m_U$ , allowing for expressions (1), (2), (5), (7) and (8), is equal to:

$$m_U = \frac{U_1}{U_2} \approx \frac{f_1 d_1 \Delta_1}{f_2 d_2 \Delta_2} = m_f m_l m_l, \quad (9)$$

that corresponds to  $m_B$  scale.

Electric resistance of rod regions, through which the current flows is:

$$R_{1,2} = \rho \pi k_d \frac{d_{1,2}}{S_{1,2}}, \quad (10)$$

where  $S_1, S_2$  are the cross-sectional areas, through which current passes in the rods. At high frequencies:

$$S'_1 \approx \Delta_{1,2} l_{1,2}. \quad (11)$$

Scale of electric resistance  $m_R$ , allowing for expressions (2), (10) and (11), is equal to:

$$m_R = \frac{R_1}{R_2} \approx \frac{d_1 \Delta_2 l_2}{d_2 \Delta_1 l_1} = \frac{m_l}{m_l m_l} = \frac{1}{m_l}. \quad (12)$$

In keeping with Ohm's law the current is:

$$I_{1,2} = \frac{U_{1,2}}{R_{1,2}}. \quad (13)$$

Current scale  $m_I$ , taking into account expressions (9), (12) and (13), is equal to:

$$m_I = \frac{I_1}{I_2} = \frac{m_U}{m_R} = m_l. \quad (14)$$

Current density is:

$$J_{1,2} = \frac{I_{1,2}}{S'_{1,2}}. \quad (15)$$

Scale of current density  $m_j$ , taking into account expressions (2), (11), (14) and (15) is equal to:

$$m_j = \frac{J_1}{J_2} \approx \frac{I_1 \Delta_1 I_1'}{I_2 \Delta_1 I_1'} = \frac{m_I}{m_I m_l} = \frac{1}{m_l}. \quad (16)$$

Full and active power is:

$$S_{1,2} = U_{1,2} I_{1,2}; \quad P_{1,2} = I_{1,2}^2 R_{1,2}. \quad (17)$$

The scales of full  $m_s$  and active power  $m_p$  taking into account expressions (9), (12), (14) and (17), are equal to:

$$m_s = \frac{S_1}{S_2} = m_U m_I = m_l; \quad (18)$$

$$m_p = \frac{P_1}{P_2} = m_I^2 m_R = \frac{m_U^2}{m_R} = m_l.$$

Energy per one period of current oscillation is proportional to power and time  $W \sim Pt$ , its scale being  $m_w$ :

$$m_w = \frac{W_1}{W_2} \sim \frac{P_1 t_1}{P_2 t_2} = m_p m_t = m_l^3. \quad (19)$$

Flux linkage  $\Psi$  is:

$$\Psi_{1,2} = w \Phi_{1,2} = w B_{1,2} S_{1,2}, \quad (20)$$

where  $w$  is the number of turns, for rods  $w = 1$ ;  $\Phi_1, \Phi_2$  are the magnetic fluxes in the rods. Here, the scale of flux linkage  $m_\Psi$  and of magnetic fluxes  $m_\Phi$  from expressions (1), (8) and (20) is as follows:

$$m_\Psi = \frac{\Psi_1}{\Psi_2} = \frac{d_1 \Delta_1}{d_2 \Delta_2} = m_l m_l = m_l^2; \quad L_{1,2} = \frac{\Psi_{1,2}}{I_{1,2}}. \quad (21)$$

Inductance is:

$$L_{1,2} = \frac{\Psi_{1,2}}{I_{1,2}}. \quad (22)$$

Scale of inductance  $m_L$  taking into account expressions (1), (14), (20) and (22), is equal to:

$$m_L = \frac{L_1}{L_2} = \frac{\Psi_1 I_2}{\Psi_2 I_1} = \frac{m_\Psi}{m_I} = m_l. \quad (23)$$

Inductive (reactive) resistance is:

$$X_{1,2} = 2\pi f_{1,2} L_{1,2}. \quad (24)$$

Scale of inductive resistance  $m_x$ , taking into account expressions (5), (23) and (24), is equal to:

$$m_x = \frac{X_1}{X_2} = \frac{f_1 L_1}{f_2 L_2} = m_f m_l = \frac{1}{m_l}. \quad (25)$$

Scale of full resistance  $m_z$ , allowing for expressions (23) and (25) is:

$$m_z = \frac{Z_1}{Z_2} = \sqrt{m_R^2 + m_X^2} = \frac{1}{m_l}. \quad (26)$$

*Similarity of thermal processes.* Fourier criterion [16] for nonstationary thermal processes has the following form:

$$Fo = \frac{at'}{l^2}, \quad (27)$$

where  $a$  is the heat conductivity coefficient:

$$a = \frac{\lambda'}{\gamma c}, \quad (28)$$

where  $\lambda$  is the heat conductivity;  $\gamma$  is the density;  $c$  is the heat content ( $a, \lambda, \gamma$  and  $c$  are the same for the full-scale and model rods);  $t'$  is the heating (or cooling) time.

$$m_t' = \frac{t_1'}{t_2'} = \left( \frac{l_1}{l_2} \right) = m_l^2. \quad (29)$$

The rate of heating  $v$  of the rod sections is directly proportional to temperature  $T$  and is inversely proportional to time  $t'$ ,  $v \sim T/t'$ . As the temperatures should be the same, the scale of the rate for thermal processes of the rod heating  $m_v$ , is as follows, allowing for expression (29):

$$m_v = \frac{v_1}{v_2} \sim \frac{t_2'}{t_1'} = \frac{1}{m_t'} = \frac{1}{m_l^2}. \quad (30)$$

*Model scaling.* For a full-scale sample the current frequency of the thyristor frequency converter is  $f_1 = 2.4$  kHz, for a model sample the thyristor frequency converter has current frequency  $f_2 = 130$  kHz. The scale coefficient of frequency by formula (5) is  $m_f = 18.462 \cdot 10^{-3}$ , while the scale coefficient of linear dimensions by formula (4) is  $m_l = 7.36$ .

The depths of penetration of induced currents in the full-scale and model rods by formula (3) (at  $\rho_{850^\circ\text{C}} \approx 7.76 \cdot 10^{-7}$  Ohm·m) are  $\Delta_1 = 9.05$  mm,  $\Delta_2 = 1.23$  mm in the case, when the steel has lost its magnetic properties.

The full-scale sample diameter is  $d_1 = 62.7$  mm. We will use the scale factor of linear dimensions to determine the model sample diameter  $d_2 = d_1/m_l \approx 8.5$  mm.

In Table 1 we will give the values of scale factor for the model rod, and in Table 2 — the initial data for

**Table 1.** Values of induction system scale factors

Parameter	Transition factor	Scale factor
Linear dimensions $l$	$m_l = 1/\sqrt{m_f}$	7.360
Current frequency $f$	$m_f = 1/m_l^2$	$18.46 \cdot 10^{-3}$
Current period $T$	$m_T = m_l^2$	54.200
Current $I$	$m_I = m_l$	7.360
Electric resistance $R$	$m_R = 1/m_l$	0.135
Current density $J$	$m_J = 1/m_l$	0.135
Power $S$	$m_S = m_l$	7.360
Power $P$	$m_P = m_l$	7.360
Energy $W$	$m_W = m_l^3$	398.680
Flux linkage $\Psi$	$m_\Psi = m_l^2$	54.20
Inductance $L$	$m_L = m_l$	7.360
Reactance $X$	$m_X = 1/m_l$	7.360
Impedance $Z$	$m_Z = 1/m_l$	0.135

numerical modeling of this «inductor–rod» induction system.

The computational domain of the studied model of the induction system is shown in Figure 2. It contains a three-turn water-cooled inductor  $\Omega_1$ , from a copper conductor in the form of a round tube with an internal rectangular concentrator of the magnetic field and is a source of variable magnetic field of specified frequency. The product being heated is a sample in the form of a solid cylindrical rod  $\Omega_2$  from high-carbon ferromagnetic rail steel with simulation of the welded joint HAZ  $\Omega_3$  in its center and of ambient air  $\Omega_4$ . From the viewpoint of axial symmetry, the mathematical model is represented in a two-dimensional cylindrical axisymmetric system of coordinates  $rOz$ . The electromagnetic problem was considered in the frequency domain, and the thermal nonstationary problem — in the time domain. The following physical processes were taken into account at modeling: joulean heating of sample metal due to eddy currents generated in it, thermal conductivity in the metal volume, heat losses for radiation and convection.

The process of induction heating is described by a nonlinear interdependent system of Maxwell and

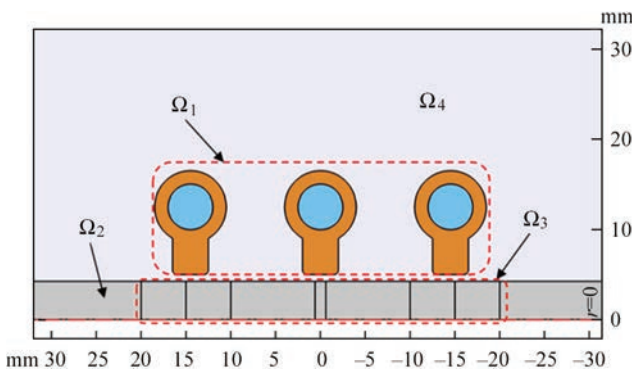


**Figure 2.** Axisymmetric model of the induction system

**Table 2.** Initial data for numerical modeling of «inductor–rod» system

Parameter	High-carbon steel (0.8 % C)
Sample length, mm	110
Sample diameter, mm	8.5
Ambient temperature, °C	20
Initial sample temperature, °C	20
Supply current frequency, kHz	130
Inductor current, A	200
Specified temperature of zone heating, °C	850...900
Outer diameter of the inductor, mm	28–33*
Inner diameter of the inductor, mm	8.75–10.75*
Inductor width, mm	28–38*
Distance between inductor windings, mm	7–10*
Tube diameter, mm	6

\*Initial values for parametric investigation of the inductor geometrical dimensions.

Fourier equations for the electromagnetic and thermal fields with the respective boundary conditions [16].

In order to solve the electromagnetic part of the calculation, the system of Maxwell equations is presented in the differential form:

$$\begin{aligned} \operatorname{rot} \vec{H} &= \vec{J} + \frac{\partial \vec{D}}{\partial t}; & \operatorname{rot} \vec{E} &= -\frac{\partial \vec{B}}{\partial t}; \\ \operatorname{div} \vec{D} &= \rho_e; & \operatorname{div} \vec{B} &= 0, \end{aligned} \quad (31)$$

where  $\vec{H}$ ,  $\vec{E}$  are the vectors of magnetic and electric field intensities;  $\vec{D}$ ,  $\vec{B}$  are the vectors of electric and magnetic induction;  $\vec{J}$  is the vector of conduction current density;  $\vec{J} = \sigma \vec{E}$ ;  $\sigma$  is the specific electric conductivity;  $\rho_e$  is the density of extraneous electric charge.

Density of bias current  $\frac{\partial \vec{D}}{\partial t}$  does not have any noticeable influence up to megahertz frequency range, as the conduction current density is much higher than that of bias current, so that it can be ignored, and then the equation becomes:

$$\operatorname{rot} \vec{H} = \vec{J}. \quad (32)$$

The system of equations (31) was complemented by material equations for establishing a connection between the magnetic field intensity and magnetic induction, electric bias and electric field intensity, characterizing the electric and magnetic properties of the environment:

$$\bar{B} = \mu_0 \mu_r \bar{H}; \quad \bar{D} = \varepsilon_0 \varepsilon_r \bar{E}, \quad (33)$$

where  $\varepsilon_0$  is the absolute dielectric permeability of the material;  $\varepsilon_r$  is the relative dielectric permeability of the material.

Numerical calculation of the electromagnetic fields of the induction system by finite element method is performed, using the representation of the distribution of vectors  $\bar{H}$ ,  $\bar{E}$  in the form of potential functions, and the equations are written using the vector magnetic potential  $\bar{A}$  and scalar electric potential  $\bar{V}$  which are defined as follows:

$$\bar{B} = \text{rot} \bar{A}; \quad \bar{E} = -\frac{\partial \bar{A}}{\partial t} - \text{grad} \bar{V}. \quad (34)$$

As in the axisymmetric model the currents are directed normal to the geometrical model plane, the vector magnetic potential  $\bar{A}_\varphi$  has a single component  $(0, \varphi, 0)$ , unlike  $\bar{H}$ ,  $\bar{B}$  fields, which have two components  $(r, z)$  in this plane.

Proceeding from the system of Maxwell equations, and allowing for the assumptions made and the connections for the conducting sections (of the inductor and steel rod) the differential equations will be written in the following form:

$$\begin{aligned} \nabla \left( \frac{\nabla}{\mu_0 \bar{A}} \right) &= \bar{J}_0; \\ j\omega \sigma(T) \bar{A} + \nabla \times \left( \frac{\nabla}{(\mu_0 \mu_r(T))} \bar{A} \right) &= 0, \end{aligned} \quad (35)$$

where  $\nabla$  is the nabla operator;  $\bar{J}_0$  is the vector of current density;  $j = \sqrt{-1}$  is the imaginary unit;  $\omega$  is the angle frequency of the field,  $\omega = 2\pi f$ . Here,  $\sigma$  and  $\mu_r$  depend on temperature  $T$ .

For correct calculation of the induction system parameters, it is necessary to take into account the dependence of electrophysical properties of steel on temperature  $T$ , as well as the loss of magnetic properties by it after reaching the temperature of the Curie point —  $T_k$  that will change the depth of penetration of the magnetic field and eddy currents into steel, resonance frequency and quality factor of the induction system.

In order to determine the magnetic permeability  $\mu$  of the steel sample with carbon content in the range of 0.5–1.0 %, depending on magnetic field intensity  $\bar{H}_0$  and temperature, an approximation function of the following form was adopted [18]:

$$\mu(H_0, T) = \begin{cases} 1 + \frac{\alpha' H_0^{\beta'} - 1}{\left[ 1 + \left( \frac{T}{T_k - T} \right)^{\chi'} \right]^{\delta'}}, & \text{if } T < T_k; \\ 1, & \text{if } T \geq T_k, \end{cases} \quad (36)$$

where  $\alpha' = 3 \cdot 10^5$ ;  $\beta' = -0.85$ ;  $\chi' = 1.9$ ;  $\delta' = 0.16$  are the approximation factors.

At modeling of the process of induction heating, the following was assigned as the boundary conditions of the electromagnetic part of the problem: on axis of symmetry  $0z$  the Neumann condition  $\frac{\partial \bar{H}}{\partial t} = 0$  — absence of the tangential component of the magnetic field intensity; Dirichlet condition  $\bar{A}_\varphi = 0$  — presence of magnetic insulation on the outer boundaries, when the field is localized within the calculated region. The condition of constant temperature (30 °C) in the inductor turns due to cooling was accepted in a similar way.

In order to solve the nonstationary thermal problem in the time domain [16], Fourier equation, describing the temperature field distribution, was used:

$$\gamma c(T) \frac{\partial T}{\partial t} - \nabla \lambda \nabla T = Q, \quad (37)$$

where  $Q$  is the specific power of the heat sources.

Considering the nonlinear nature of the dependencies of physical parameters  $\gamma$ ,  $c$ ,  $\lambda$ , and  $\sigma$  on temperature  $T$ , in equation (37) they were assigned by the interpolation functions based on reference data for the high-carbon steel.

Calculation of specific power of inner heat sources links the electromagnetic problem to the thermal problem through determination of ohmic losses from the induced eddy currents in the sample that has a non-zero resistance, and non-zero density, according to Joule–Lentz law:

$$P = \frac{1}{n} \sum_{i=1}^n \frac{\bar{J}_i}{\sigma}, \quad (38)$$

where  $P$  is the evolving volumetric power;  $\bar{J}_i$  is the total current density in integration point  $i$ .

In order to take into account thermal losses from convection and radiation from the side and end faces of the rod, the following expression was given:

$$q = -\bar{n}(-k \nabla T) = k(T - T_0) + \varepsilon \delta (T^4 - T_0^4). \quad (39)$$

where  $\bar{n}$  is the unit outward normal vector;  $k$  is the convective heat transfer coefficient;  $T_0$  is the ambient

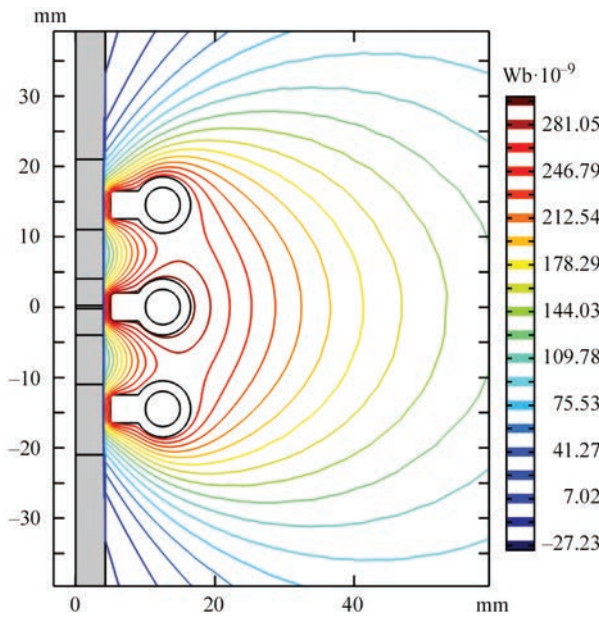


**Figure 3.** Distribution of force lines of the magnetic field of induction system

temperature;  $\varepsilon$  is the Stephan–Boltzmann constant;  $\delta$  is the emissivity.

For correct accounting for the surface effect in the conductors and product, the computational grid cells were taken to be rectangular and very fine in the thin layer along the depth of magnetic field and eddy current penetration. In other areas the grid cells have the form of triangles.

**Results of studying mathematical modeling of an induction system of heat treatment process.**

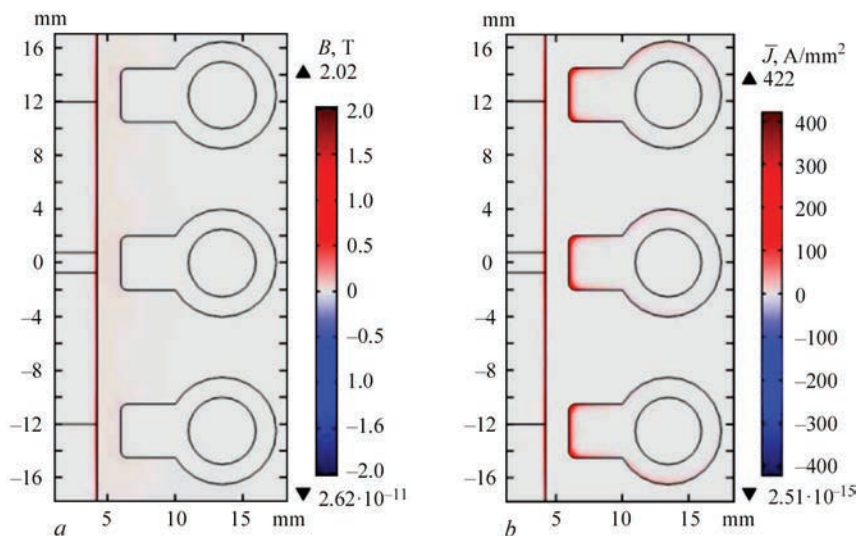
A distribution of the electromagnetic field of an induction system was derived as a result of solving the problem in the frequency domain (Figure 3). Due to the ring effect the lines of force of the magnetic field gather near the inductor inner surface and the rod outer surface with a high intensity of the magnetic field. Similarly, the current is concentrated in this area on

the inner surface of the inductor conductors, namely on the edges of the rectangular concentrators of the magnetic field near the rod, and in the rod — on the surface under the inductor.

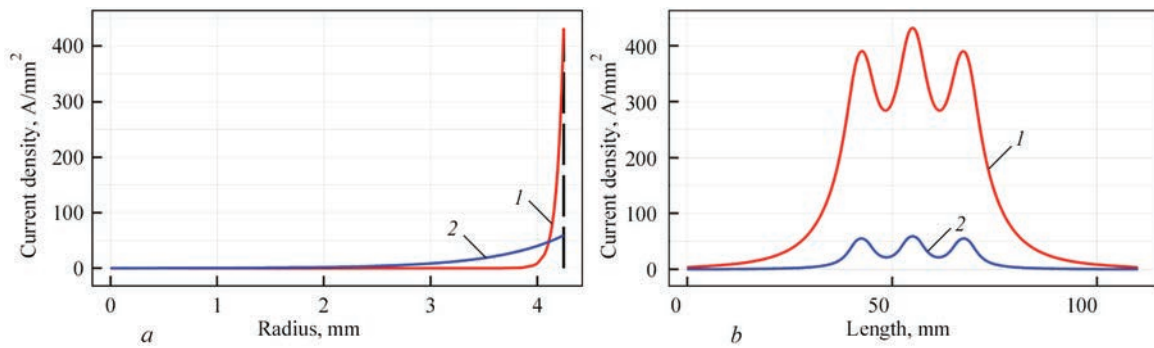
Figure 4, *a* shows the distribution of magnetic induction,  $\vec{B}$ , and Figure 4, *b* — distribution of current density,  $\vec{J}$ . The presented figures clearly show the ring effect and skin-effect in the inductor and rod conductors.

Figure 5, *a* shows the distribution of current density in the rod cross-section from its center to the side surface in its magnetic and non-magnetic state (temperature above the Curie point). On the rod surface in the magnetic state the current density is maximum and reaches the value of 422 A/mm<sup>2</sup>. Closer to the rod center the current density drops abruptly and at the depth of 0.02 mm its value is equal to 313 A/mm<sup>2</sup>; at the depth of 0.04 mm it is 234 A/mm<sup>2</sup>; at the depth of 0.1 mm — 96 A/mm<sup>2</sup>, and at the depth of 0.4 mm — just 2 A/mm<sup>2</sup>. In the nonmagnetic state the current density is the highest on the rod surface and equal to 49 A/mm<sup>2</sup>, at 4 mm distance from the rod center it is 30 A/mm<sup>2</sup>, at 3 mm distance — 8 A/mm<sup>2</sup>, and at 2 mm distance — 1 A/mm<sup>2</sup>. Current density distribution in the axial direction on the rod surface is shown in Figure 5, *b*. Its peak values are determined under the rectangular concentrators of the magnetic field of inductor turns, where the distance to the rod surface is the shortest.

During modeling the energy parameters of the induction system were studied, depending on inductor current frequency  $f = 0.05\text{--}130.0$  kHz. Figure 6, *a* shows the calculated dependencies of the total  $S_1$ , reactive  $Q_1$  and active  $P_1 = P \cdot R$  power of the inductor, active power in a model rod  $P_2 = Q$  and power factor  $\cos\varphi = P_1/S_1$  (Figure 6, *b*). The active power release is enhanced with increase of current frequency that is



**Figure 4.** Distribution of induction system energy characteristics: *a* — magnetic induction; *b* — current density



**Figure 5.** Distribution of current density in a model sample: *a* — in the rod cross-section from its center to the surface in its magnetic (1) and nonmagnetic (2) state; *b* — in the axial direction on the rod surface

related to reduction of the skin layer and increase of active resistance in the current passage path.

At calculation of the processes in the time domain the electromagnetic and thermal calculations were conducted sequentially, with refining of temperature-dependent parameters at each iteration step. In the electromagnetic part of the calculation, the most important parameter, which is transferred to the thermal part of the calculation, is the electric power, which evolves in the product and is responsible for heating. The ultimate goal of the calculation is obtaining a favorable distribution of the temperature field in the product at heat treatment of the sample with minimizing the thermal impact on the base metal beyond the welded joint. The welded joint proper consists of several different zones: fusion line (white band), zones of the coarse and fine grain, and softening zone. The metal in these zones has different structural components and different mechanical characteristics, which differ from the zone of base metal, which is not exposed to the thermal impact of welding. During modeling of heat treatment of metal in the welded joint zone, its heating was performed up to temperature somewhat higher than the structural transformation point  $A_{c3}$ , close to 850–900 °C, at which the required structural

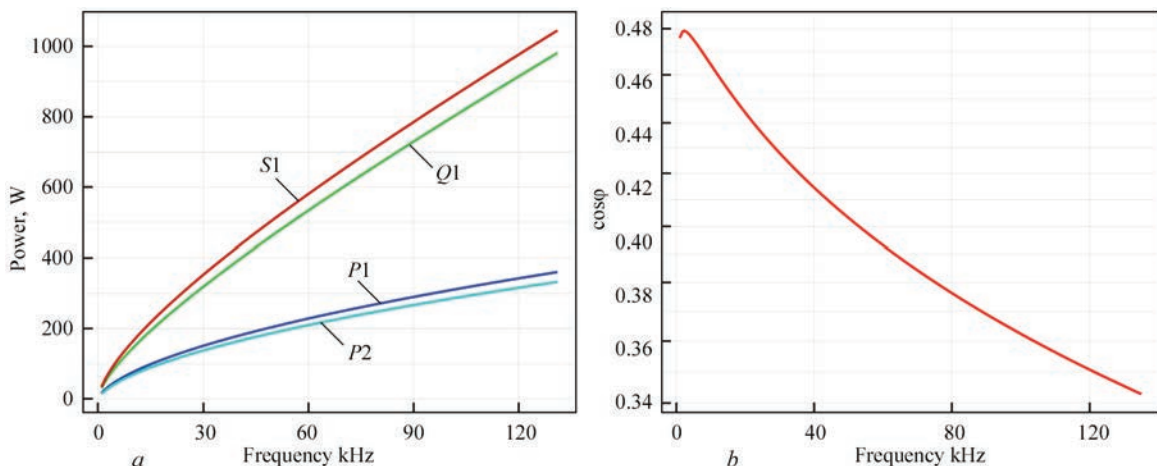
transformations of metal in the welded joint zone take place, to ensure a uniform structure of the metal.

During parametric solution of the problem, in order to obtain the required temperature field, the geometrical design parameters of the inductor — its width of 33 mm, interaxial distance of 8 mm, inner diameter of 9.75 mm and outer diameter of 30 mm were determined.

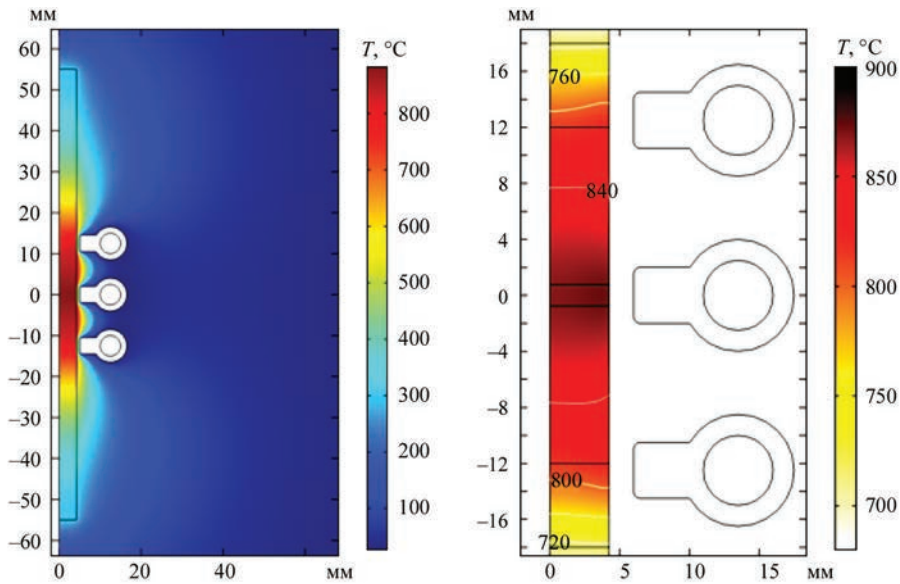
Figure 7 shows the distribution of the induction system temperature field at the end of the heating cycle. These geometrical parameters of the inductor provide the required temperature field and heating temperature above that of the start of phase transformations in the area of the sample welded joint that will allow achieving the required structural transformations in the joint metal.

Figure 8, *b* shows the location of points for temperature monitoring, when solving the thermal problem in different zones of the welded joint and the rod base metal zone.

In Figure 9 the graphs of temperature variation with time in these points were plotted. One can see that the process of sample heating can be divided into two characteristic regions. The first is the region of heating the ferromagnetic metal to magnetic transformation point (Curie point), where the most intensive



**Figure 6.** Energy parameters of induction system, depending on inductor current frequency: *a* —  $S_1$ ,  $Q$ ,  $P_1$  and  $P_2$ ; *b* — power factor  $\cos\varphi$



**Figure 7.** Temperature field distribution in the sample longitudinal section

heating takes place due to absorption of the electromagnetic energy by a thin skin-layer and high density of induced current flowing in it, with considerable evolution of thermal power and temperature propagation to the deep layers due to heat conductivity. In the second region a lowering of heating intensity is observed, because of the metal losing its magnetic properties and of an increase in the depth of current penetration at lowering of its density with reduction of the released thermal power and lowering of heating intensity.

**Physical modeling of the process of induction heat treatment of a model sample.** The parameters determined from earlier performed mathematical

modeling were used to conduct experiments on physical modeling of the process of induction HT. Physical modeling was performed on a sample of 8.5 mm diameter and 110 mm length, which was cut out of the railway rail head from high-strength rail steel K76F with a welded joint, located in the sample center (Figure 8, a).

Induction heating of the model sample was conducted using the developed low-power laboratory mock-up of a high-frequency power source based on a bridge inverter. The resonant oscillating circuit of the laboratory mock-up operates by the series type of RLC-circuit connection, where the model sample is the load. The copper three-turn water-cooled inductor with a magnetic field concentrator is placed above the welded joint zone. A battery of compensation capacitors and a matching transformer are connected. The power of the laboratory mock-up of the high-frequency current source for induction HT is equal to 2 kW, current frequency is 130 kHz. Rogowsky belt and digital oscilloscope Siglent SDS 1102CLM+ were used to control the inductor current, frequency, shape and amplitude of inductor voltage. To monitor the temperature change in the model sample, two reference points were defined: the first was thermocouple 1 (Figure 8) in the sample central part on its surface, to determine the maximum temperature of sample heating, and the second was thermocouple 2 at the end of welded joint HAZ to monitor the temperature field propagation in keeping with mathematical modeling. Used as sensors for temperature monitoring, were chromel-alumel thermocouples of K type of 0.75 mm diameter, which were welded-on in the specified points on the sample surface by capacitor-discharge welding. Conversion of the signal from thermocouple sensors in real time was performed by ADC L-Card E20-10

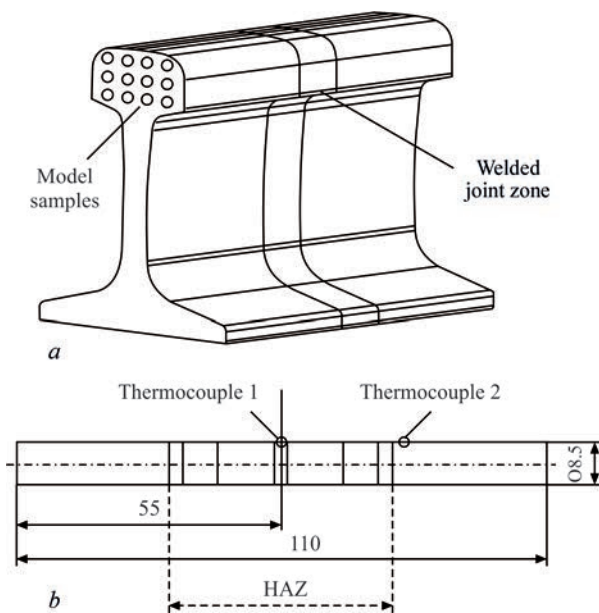


**Figure 8.** Sample for physical modeling of induction HT: a — illustration of the scheme of cutting out model samples from a welded joint of railway rail; b — layout of points for model sample temperature monitoring

and galvanic decoupling block Promsad PSA0101, as well as special software for computer visualization of the derived data.

The thermal cycle of the induction heating process was determined, when conducting the experiments on physical modeling of induction HT of an experimental model sample from high-strength rail steel (Figure 9). At physical modeling the sample maximum temperature in the first reference point was equal to 882 °C for 180 s of the heating process, and in the second reference point it was 578 °C for 180 s. When comparing the calculated and experimental thermal cycles the largest error was close to 10 %. The calculation data obtained with application of the finite element method and measurement data at physical modeling of the thermal cycles lead to the conclusion that the calculated temperature change in the mathematical model agrees well with the experimental data. This allows using it for the next modeling step: determination of structural transformations in the welded joint metal under the impact of technological parameters of heat treatment that enables optimizing the technological processes of induction heat treatment of welded butt joints of railway rails.

**Results of investigations at induction system modeling.** Analysis of the presented results shows the correct solution of the problem, allowing for the physical processes and phenomena during modeling of the induction heating process. The developed mathematical model for numerical modeling of the process of high-frequency induction heating of a model sample of welded joint on high-carbon, high-strength rail steel, derived on the base of the similarity theory, allows establishing the parameters and configuration of «inductor–product» system for performance of induction HT of a sample, and determination of the space-time distribution of the temperature field during performance of its HT. Then the results of the first part of the modeling problem should be transferred to the second part, where modeling of the kinetics of phase transformations and weld metal properties will be performed, depending on the process thermal cycle, which will allow determination of the range of optimally required parameters of HT process. After numerical calculation, the obtained data will be used during physical modeling, with optimization of the modes of sample HT, and it will help significantly reduce the number of the conducted experiments on determination of the thermal cycle impact on the features of phase transformation kinetics and mechanical properties in the welded joint zone. At achievement of satisfactory results on a model sample, it is necessary to go over to investigation of the process of induction heating at HT of the metal of weld and near-weld zone

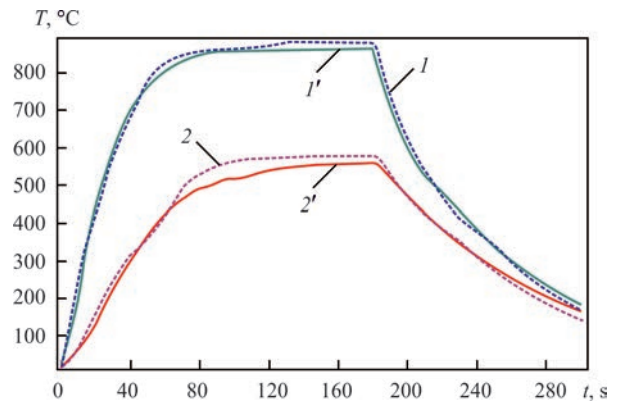


**Figure 9.** Change of temperatures in time in reference points of the model sample: 1, 2 — thermal cycle during physical modeling; 1', 2' — calculated data from mathematical modeling

of a real product — the rail, while performing recalculation of the parameters by the similarity theory, following the established HT modes and refining them, as well as correcting the inductor configuration.

### Conclusions

1. To simplify physical modeling of induction heating, the theory of similarity of the electromagnetic processes was used to reduce the overall dimensions of a model cylindrical rod using the scale factors.
2. The developed mathematical model for numerical modeling of the process of high-frequency induction heating of a welded joint sample from high-carbon high-strength rail steel allows determination of optimum geometrical and energy parameters of «inductor–product» system.
3. The numerical solution of an axisymmetric problem, taking into account the main nonlinear dependencies of the induction model, allows modeling the space-time distribution of the temperature field.
4. Proceeding from determination of the main energy parameters of «inductor–product» system, a parametric search for optimum geometrical parameters of the inductor was performed, and the required distribution of the temperature field in the zone of the sample welded joint was obtained.
5. When modeling of thermal heating of a welded joint sample was performed, the temperature field of the sample with the weld was determined that allows modeling the change of the space-time structural-phase state of the metal during heat treatment.
6. The proposed mathematical and physical models of model sample heating can be used, when solving the problem of optimization of induction heat treatment of welded joints of railway rails. Use of these data at determination of key parameters of the heat treatment process on model samples allows going over to heat treatment of welded joints of the real

railway rails in the welded joint zone, based on the similarity theory.

- Gubatyuk, R.S. (2019) Heat treatment of welded joints of high-strength railway rails (Review). *The Paton Welding J.*, **2**, 41–48. doi: <https://doi.org/10.15407/tpwj2019.02.07>
- Kuchuk-Yatsenko, S.I., Antipin, E.V., Didkovskiy, O.V. et al. (2020) Evaluation of quality of welded joints of high-strength railway rails of modern production taking into account the requirements of Ukrainian and European standards. *Ibid.*, **7**, 3–11. DOI: <https://doi.org/10.37434/tpwj2020.07.01>
- Rezanov, V.A., Fedin, V.M., Bashlykov, A.V. (2013) Differentiated hardening of rail welded joints. *Vestnik VNIIZhT*, **2**, 28–34 [in Russian].
- Dolgikh, I.Yu., Korolyov, A.N., Zakharov, V.M. (2014) Simulation of thermal processes dynamics under induction heating. *Vestnik ISEU*, **5**, 1–7 [in Russian].
- Pleshivtseva, Yu. E., Popov, A. V., Popova, M. A., Derevyanov, M. Yu. (2019) Optimal inductor design for surface hardening of cylindrical billets based on numerical two-dimensional model. *Vestnik of Astrakhan State Technical University. Series: Management, Computer Science and Informatics*, **1**, 40–50. DOI: <https://doi.org/10.24143/2072-9502-2019-1-40-50>
- Chao, Yu, Hong, Xiao, Zi-chen, Qi, Yun-peng, Zhao (2019) Finite element analysis and experiment on induction heating process of slab continuous casting-direct rolling. *Metallurgical Research & Technology*, **116** (4), 403. doi: <https://doi.org/10.1051/metal/2018117>
- Li, F., Ning, J., Liang, S. (2019) Analytical modeling of the temperature using uniform moving heat source in planar induction heating process. *Applied Sci.*, **9**, 14–45. DOI: <https://doi.org/10.3390/app9071445>
- Takeuchi, H., Yogo, Y. (2019) An induction heating analysis with consideration of temperature dependent B-H curves and change in phase transformation under rapid heating. *ISIJ Int.*, **59**, 551–558. DOI: <https://doi.org/10.2355/isijinternational.isijint-2018-552>
- Javaheri, V., Asperheim, J.I., Grande, B. et al. (2020) Simulation and experimental studies of induction hardening behavior of a new medium-carbon, low-alloy wear resistance steel. *COMPEL — the International J. for Computation and Mathematics in Electrical and Electronic engineering*, **39**(1), 158–165. DOI: <https://doi.org/10.1108/COMPEL-06-2019-0227>
- Gubatyuk, R.S., Rymar, S.V., Prokofiev, O.S. et al. (2021) Simulation of electromagnetic and thermal fields in the process of induction heating on small specimens with the presence of welded joint of high-strength railway rails. *The Paton Welding J.*, **1**, 44–49. DOI: <https://doi.org/10.37434/as2021.01.08>
- Roppert, K., Toth, F., Kaltenbacher, M. (2020) Modeling nonlinear steady-state induction heating processes. *IEEE Transact. on Magnetics*, **56** (3). DOI: <https://doi.org/10.1109/tmag.2019.2957343>
- Venikov, V.A. (1966) *Similarity theory and modeling as applied to the problems of the electric power industry*. Moscow, Vysshaya Shkola [in Russian].
- Paton, B.E., Lebedev, V.K. (1969) *Electrical equipment for resistance welding*. Moscow, Mashinostroenie [in Russian].
- Pentegov, I.V., Rymar, S.V., Levin, M.I., Lavrenyuk, A.V. (2015) Determination of magnetic inductions in the magnetic circuits of power transformers with the combined use of anisotropic and isotropic electrical steels. *Elektrotehnika i Elektromekhanika*, **6**, 31–35 [in Russian]. DOI: <https://doi.org/10.20998/2074-272X.2015.6.05>
- Kutateladze, S.S. (1982) *Similarity analysis in thermal physics*. Novosibirsk, Nauka [in Russian].
- Landau, L.D., Lifshits, E.M. (2006) *Field theory. Theoretical physics*. Moscow, Fizmatlit [in Russian].
- Pentelyat, M.G., Shulzhenko, N.G. (2007) Use of vector magnetic potential in finite element analysis of non-stationary three-dimensional electromagnetic fields in conducting media. *Elektrotehnika i Elektromekhanika*, **5**, 42–47 [in Russian].
- Vladimirov, S.N., Zeman, S.K., Ruban, V.V. (2009) Analytical relations approximating the temperature-field dependence of the magnetic permeability of structural steels. *Izv. TPU*, **315**(4), 100–104 [in Russian].

Received 12.07.2021



## Electron Beam — Physical Vapor Deposition (EB-PVD) Technologies and Equipment



- ◆ Technology for high-rate electron beam evaporation of metals and alloys, using an intermediate «hot» pool of refractory metals
- ◆ Technologies for deposition of functional multilayers and graded protective coatings (oxidation-resistant, corrosion-resistant, thermal barrier, erosion-resistant and damping) for GTE component
- ◆ Design, manufacture and «turn-key» delivery of EB-PVD units (UE-204, UE-207S, UE-210 and UE-211 types), in keeping with customer specification
- ◆ Training customer specialists to operate the EB-PVD units

International Center for Electron Beam Technologies of PWI  
[www.paton-icebt.kiev.ua](http://www.paton-icebt.kiev.ua)

# USE OF CAPACITIVE ENERGY STORAGES TO CREATE HIGH-EFFICIENT MULTISTATION WELDING SYSTEMS

**O.Ye. Korotynskyi and M.I. Skopyuk**

E.O. Paton Electric Welding Institute of the NAS of Ukraine

11 Kazymyr Malevych Str., 03150, Kyiv, Ukraine. E-mail: [office@paton.kiev.ua](mailto:office@paton.kiev.ua)

Analysis of structures of multistation sources for arc welding, designed on the base of capacitive energy storages, was carried out. Their prospects for creation of high-efficient welding-technological systems are shown. The structures of centralized power supply systems of welding stations are considered, in which one powerful electric energy storage is used. A decentralized power supply system of the stations is more flexible, when an individual electric energy storage is installed at each workplace. Its advantage consists in the fact that a standard rectifier of VDGM type can be applied. For shipbuilding, a combined power supply system can be used, which implements the positive qualities of both power supply systems and provides a high quality and power efficiency of the welding process. As an example of the use of multistation power sources, a diagram is given, which is based on the method of charge transfer. 13 Ref., 6 Figures.

*Keywords:* pulsed arc welding, capacitive energy storage, capacitor with double electric layer, charge transfer method, multistation welding systems, step-down converter

It is known that multistation welding systems (MSWS) are widely used in large machine-building enterprises, which is particularly true for shipbuilding. Evolution of these systems followed the path of increase of their energy efficiency. At the first stage these were the studies associated with elimination of ballast rheostats from their design, application of which lowered MSWS efficiency to 40 % in a number of cases. Development of this direction was based, mainly, on designing different types of converters [1, 2], which essentially lowered the power losses and brought the efficiency to 80–85 %.

MSWS application in welding offers a number of advantages to users, such as:

- two-three times lowering of power consumption, compared to welding with single-station welding units [1];
- reduction of no-load losses [3];
- reduction of the expenses for equipment purchasing [1];
- increasing labour safety during welding operations, as power is supplied to the welding station at the voltage of 60–70 V (220 or 380 V at single-station welding) [2]. At the present stage MSWS are implemented by application of semi-conductor step-down converters [3, 4], so that ensuring stable operation of welding stations on maintaining the specified accuracy of technological welding modes under the conditions of external impacts requires a more detailed consideration.

Known is a method of MSWS control, according to which, one welding current source, stabilized by output voltage level, and several unstabilized sources are used to stabilize the voltage level in low-voltage busbars. All the above-mentioned sources are connected to the industrial three-phase current mains (380 V, 50 Hz), their outputs are permanently connected to sections of the low-voltage busbar. The open-circuit voltage in the busbar is created by this summary source, stabilized by output voltage level. At increase of current load in the welding arc the voltage drop in the busbar is compensated by additional connection of unstabilized power sources to the busbar. If current in the common busbar is reduced, switching off of additional unstabilized sources is performed in the reverse order [5, 6]. Thus, voltage stabilization in the common busbar is achieved by increasing the weight and dimensions of welding equipment without maintaining the specified accuracy of the technological welding modes, their programming, as well as in the absence of the possibilities for realization of modulated current welding processes.

More and more attempts to use various electric energy storage devices for stabilization of energy flows in welding processes have been observed recently. In particular, known are devices for conversion of the energy of electrochemical storages into the energy of electric welding arc burning [7, 8] and methods to control the energy flows with the purpose of their stabilization in MSWS, using electrophysical storage devices [9].

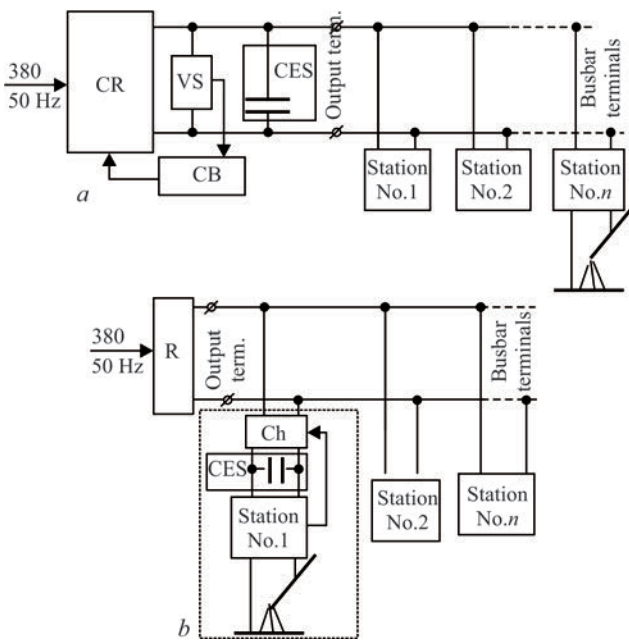


**Figure 1.** Structures of multistation welding systems with capacitive storages: *a* — centralized; *b* — decentralized

However, it should be noted that MSWS have certain disadvantages related to dependence of welding current on voltage fluctuations and change of the arc gap length; mutual influence of welding stations at their simultaneous operation, absence of the possibility of maintaining the specified accuracy of the technological modes of welding or their programming; as well as absence of the possibility of modulated current welding.

Application of high-frequency converters as welding stations, where technological mode stabilization is performed by PWM-controllers does not completely provide the continuity of welding current and voltage at the device output.

A significant disadvantage of such MSWS built using converters, is deterioration of the parameters of electromagnetic compatibility (EMC). And this leads to considerable power losses in enterprises manufacturing welded structures.

In this connection, the objective of this work is development of new approaches to creation of MSWS built, as will be shown later, using capacitive energy storages (CES). MSWS based on capacitive energy storages (CES), can use circuits corresponding to three topological structures. Figure 1, *a* shows a structure with a centralized CES [9]. A decentralized MSWS structure, where an individual storage device is installed at each station, is given in Figure 1, *b*. And finally, a combined supply diagram for the power stations is shown in Figure 2 [10]. Here, common energy storages are used, and additional storages are installed at each station. Such a structure of MSWS ensures

maximum stability of the energy stations, as well as a high quality of welded joint formation.

The centralized power supply system of the stations (Figure 1, *a*) includes a controlled rectifier (CR), voltage control sensor (VS) on the busbar (Figure 1, *a*), to which the capacitive energy storage is connected. The main purpose of the storage is forming a stable supply voltage for the stations. Supply voltage stabilization in this case is performed by control block (CB) which is connected to VS output.

The decentralized structure (Figure 1, *b*) can use a common rectifier (R), without any particularly stringent requirements to output voltage stability. However, you have to pay for it by increasing the complexity of the equipment of the stations, where charge devices (Ch) and station storages (CES/s) are additionally installed. It should be mostly used at development of systems with few stations (2 – 4 stations), for instance, for development of self-sufficient field welding-technological complexes for pipeline welding.

The best is a combined station power supply system (Figure 2), which combines the positive qualities of the above-described multistation welding systems [10]. It has a common storage, with much lower electric capacitance, compared to a centralized power system, and an individual energy storage CES/s is installed at each station, which has the function of additional stabilization of supply voltage. The operation of this MSWS system is described below.

The industrial network voltage (380 V, 50 Hz) is decreased to a safe level by a power step-down transformer included into the controlled rectifier CR. Lower voltage is rectified and converted into charge current of CES storage. Energy level of the storage, which is a capacitor in this case, is controlled by voltage sensor VS (defined as  $U = Q/C_s$ , where  $C_s$  is the storage capacity;  $U$  is the voltage level at its terminals;  $Q$  is the accumulated charge level). Here, the voltage sensor signal which comes to the input of control block CB, sets such a velocity (current) of the charge, at which the following condition is fulfilled  $R_{in}(I_b) \leq R_{tot.imp}(I_b)$ , where  $R_{in}$  is the inner resistance of controlled rectifier CR,  $I_b$  is the busbar current;  $R_{tot.imp}$  is the total impedance of the welding stations connected to the busbar.

The busbar voltage is connected, through the power terminals of the station input key InKs, to station charger WSch. Its outputs are connected to the terminals of station storage CES/s (extra high capacity capacitor bank), where the voltage level is controlled by voltage sensor VSs. The inputs of the block of forming the station volt-ampere characteristics BF/VAChs are connected to the terminals of storage CES/s. Welding current required for conducting the specific technological process of welding, is controlled by WCS, the

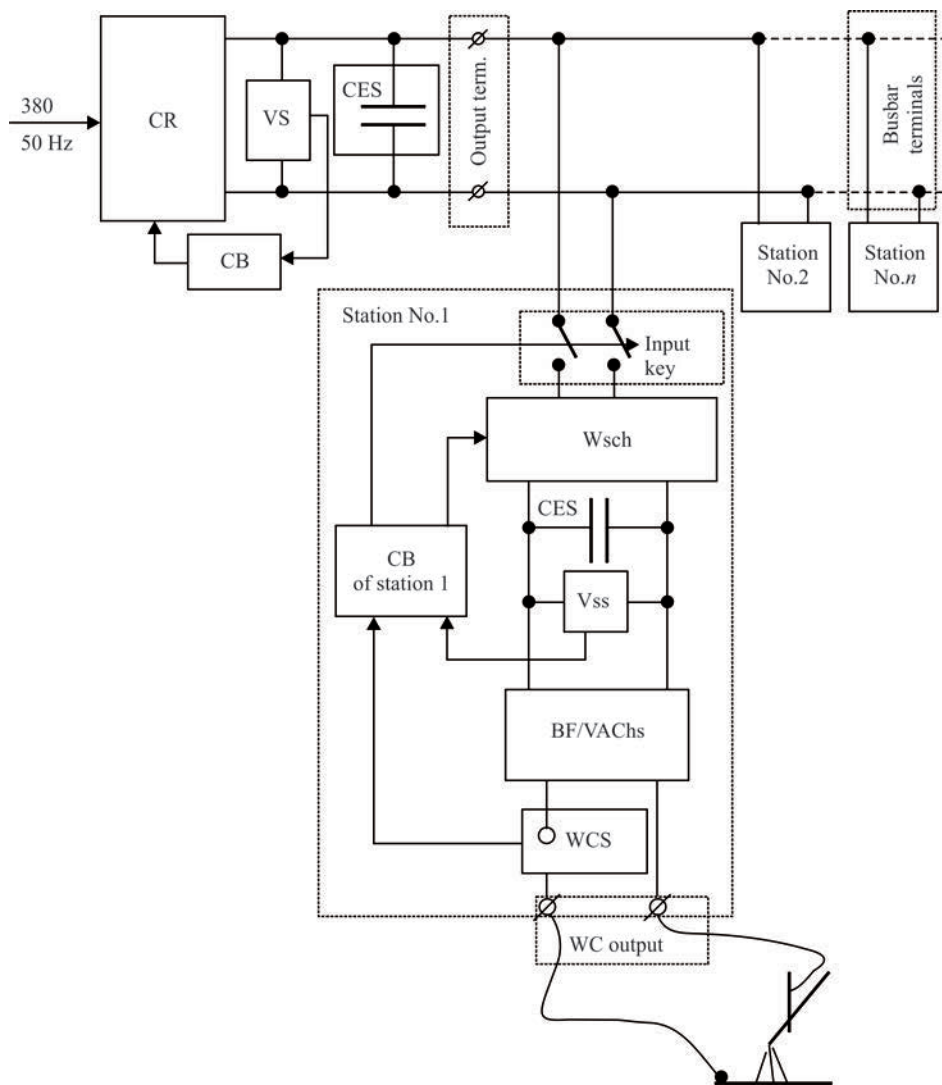


**Figure 2.** Multistation welding system with a combined diagram of station power supply

signal of which controls the switching frequency of input key InKs to maintain the required level of the charge in storage CES/s, which is necessary to perform a specific technological process of welding.

CES based on capacitors with a double electric layer have significant differences from the classical capacitors, which should be taken into account at their application in MSWS. One of such characteristics of supercapacitors (SC) is Coulomb energy efficiency. Its essence consists in that these devices cannot be discharged to a level below a certain preset specified charge level, because of the electrochemical processes, accompanying their operation. Its value, as a rule, is equal to 25–30 % of the charge maximum level.

This is exactly why the energy, transferred to the load, is provided by partial discharging of the storage. We will use a simple example to explain it.

$$W_{ch} = \frac{C_s U_{ch}^2}{2} \text{ and } W_d = \frac{C_s U_d^2}{2}.$$

Energy, which is transferred to load  $\Delta W$ , is defined as the difference between  $\Delta W_{ch}$  and  $\Delta W_d$ :

$$\Delta W = \frac{C_s}{2} (U_{ch}^2 - U_d^2).$$

If we denote  $U_d = \alpha U_{ch}$ , where  $\alpha$  characterizes the voltage level at discharge  $C_s$ , we will have:

$$\Delta W = \frac{C_s U_{ch}^2}{2} (1 - \alpha^2).$$

Considering that the storage charge is equal to  $Q = C_s U_{ch}$ , the latter expression can be presented as follows:

$$\Delta W = U_{ch} Q \frac{(1 - \alpha^2)}{2} = U_{ch} Q K_E,$$

where  $K_E = \frac{(1 - \alpha^2)}{2}$ .

If we introduce parameter  $\gamma_{ch}$  (Figure 3), characterizing the effectiveness of storage charge utilization

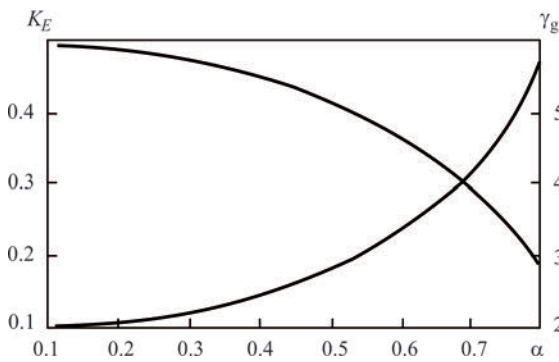


Figure 3. Coulomb energy effectiveness of storages based on capacitors with a double electric layer, depending on  $\alpha$  coefficient

and denote it by ratio  $\gamma_{ch} = \frac{Q}{\Delta Q}$ , as a result we will have:

$$\gamma_{ch} = \frac{1}{K_E} = \frac{2}{1 - \alpha^2}$$

We proposed and experimentally studied the following welding modules as station converters for the above-described MSWS topological structures: a device for powering the nonconsumable welding electrode [11]; a device for transformation of mains alternating voltage of industrial frequency into an alternating voltage of arbitrary frequency [12], or a device for forming welding current pulses of different polarity [13].

Taking the above into account, we will consider in greater detail the realization of the method of charge transfer in station converters.

The topology of the sources, build using converters with charge transfer (CChT) is based on capacitive energy storage (CES), fitted with charger (Ch) with high dynamic parameters and control module (CM).

The latter implements the control algorithms in CES charging circuit, as well as the processes of charge transfer in the welding circuit.

We will use the following reasoning, in order to functionally connect the processes, taking place in the sources with charge transfer. As is known, the charge ( $g_s$ ) in the storage can be determined by the following expression:

$$g_s = C_s U_{ch}$$

where  $C_s$  is the storage capacity;  $U_{ch}$  is its charge voltage.

On the other hand, the charge is consumed in the welding circuit:

$$g = I_w t$$

where  $I_w$  is the welding current;  $t$  is the welding time.

Then, the following ratio will be the condition for existence of continuous welding current:

$$C_s U_{ch} = I_w t$$

Assuming that the process of energy flow conversion runs in each period, i.e.  $t = 1/f$ , i.e. the latter expression can be brought to the following form

$$C_s U_{ch} = I_w / f$$

Therefore, welding current  $I_w$  is defined by the following ratio:

$$I_w = C_s U_{ch} = I_w f$$

The expression for welding current links all the main parameters of CChT-based sources. It is a base for calculation of all the processes and components of this type of arc welding sources.

Realization of the above-described algorithm of welding source operation is shown in Figure 4.

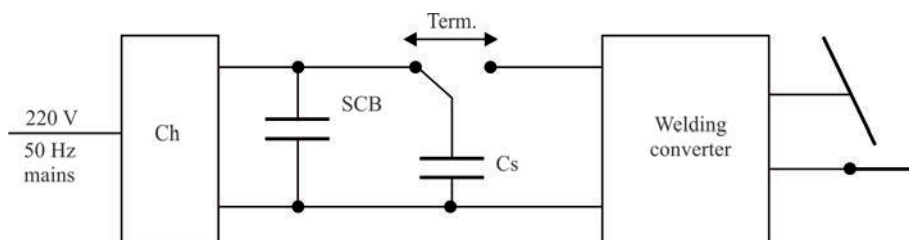


Figure 4. Block diagram of a welding source based on converters with charge transfer

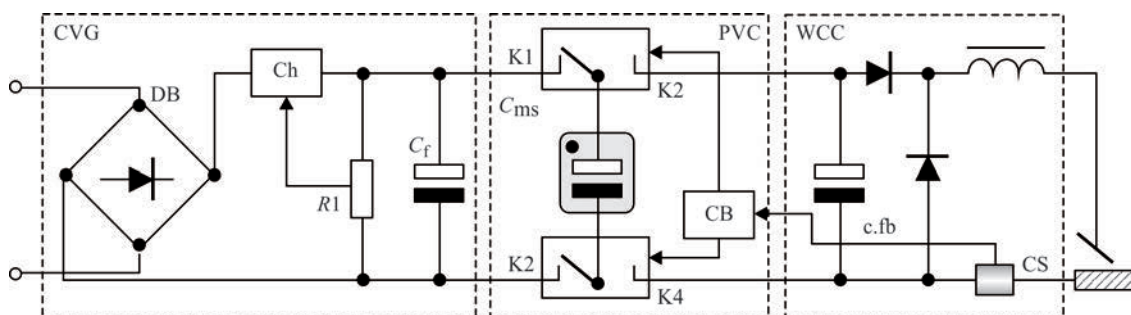


Figure 5. Converter with charge transfer

Its composition includes charger (Ch), supercapacitor bank (SCB), metering energy storage ( $C_s$ ), which actually powers the welding converter. The device operation frequency is set by the switching device.

As an example of practical application of the above approach, Figure 5 shows the diagram of a welding current source, which has the topology of a step-down converter (SDC). The device consists of three main components: constant voltage generator (CVG), pulse voltage converter (PVC) and welding current converter (WCC). CVG includes a rectifier of diode bridge (DB), charger (Ch), the level of actuation of which is assigned by potentiometer  $R1$  and filtering capacitor ( $C_f$ ). Pulse voltage converter consists of molecular storage  $C_{MS}$  and key block K1–K4, the switching algorithm of which is assigned by control block (CB). The operating mode of the latter is determined by feedback signal by welding current c.fb. PVC implements the known mode of a «flying» capacitor, which provides quasi-galvanic decoupling between the input circuit and welding circuit. The operation of WCC block is similar to that of step-down voltage converter, so that we will omit its description. A detailed description of its operation is given in [4]. The method of charge transfer can be implemented similarly in any topologies of the welding current source.

Results of an experimental study of the station converter, made according to the diagram, presented in Figure 5, are shown in Figure 6. Surfacing was performed with electrodes of UONI-13/N1-BK grade, which are usually used for the corrosion-resistant fittings. We used the mode of dynamic arc burning at two fixed frequencies:  $a$  — 10 and  $b$  — 100 Hz. In both the cases, the welding currents were equal and corresponded to the value of 120 A, the meander mode being connected.

## Conclusions

At the conclusion of this work, it should be noted that application of capacitive storages in the structure of multistation welding systems yields a set of positive results. They include, first of all:

- high energy efficiency, which is due to low inner resistance of the supercapacitors;
- possibility of developing different topological structures of multistation welding systems, depending on technological tasks, which differ by the simplicity and reliability of technical realization;



**Figure 6.** Results of an experimental study of a station converter with charge transfer:  $a$  — 10;  $b$  — 100 Hz

- ensuring a high stability of the welding modes due to a quick reaction to destabilizing factors, that is related to a fast response of the station components;
- essentially improved parameters of electromagnetic compatibility, which prevents generation of the high-frequency harmonics into the factory power supply mains.

1. Bunkin, P.Ya., Donskoj, A.V. (1985) *Multistation welding systems*. Leningrad, Sudostroenie [in Russian].
2. (1986) *Arc welding equipment: Refer. Book*. Ed. by V.V. Smirnov. Leningrad, Energoatomizdat [in Russian].
3. Korotynsky, A.E., Makhlin, N.M., Poloskov, S.I. (2009) High-efficient multistation welding systems with extended technological possibilities. *Svarka i Diagnostika*, **1**, 5–8 [in Russian].
4. Korotynsky, A.E., Makhlin, N.M., Bogdanovsky, V.A. (2002) About design of electronic controllers of welding current for multistation welding systems. *The Paton Welding J.*, **12**, 16–24.
5. Androsenko, V.I., Sergevnnin, B.I. (1989) In: USSR author's cert. 1473923. Publ. 23.04.89 [in Russian].
6. Androsenko, V.I., Sergevnnin, B.I. (1989) In: USSR author's cert. 1276453. Publ. 15.12.86 [in Russian].
7. Magerl, K., Binder, Yu., Shtigl'baur, V., Artelsmair, B. (2013) *Method and device for energy conversion and welding apparatus*. Pat. 2495734 RU. Publ. 20.10.2013 [in Russian].
8. Magerl, K., Binder, Yu., Shtigl'baur, V., Artelsmair, B. (2014) *Method and device for energy conversion and welding apparatus*. Pat. 2507043 RU. Publ. 20.02.2014 [in Russian].
9. Paton, B.E., Korotynskyi, O.E., Skopyuk, M.I. (2017) *Control mode of multistation arc welding system with accumulator*. Pat. 116573 UA. Publ. 25.05.2017 [in Ukrainian].
10. Paton, B.E., Korotynskyi, O.E., Skopyuk, M.I. (2019) *Control mode of multistation arc welding system with accumulator*. Pat. 119296 UA. Publ. 25.05.2019 [in Ukrainian].
11. Korotynskyi, O.E., Skopyuk, M.I., Drachenko, M.P., Vertetska, I.V. (2015) *Supply device for nonconsumable welding electrode*. Pat. 99852 UA. Publ. 25.06.2015 [in Ukrainian].
12. Korotynskyi, O.E., Skopyuk, M.I., Drachenko, M.P., Shapka, V.O. (2015) *Device for conversion of alternating voltage of commercial frequency into alternating voltage of arbitrary frequency*. Pat. 103509 UA. Publ. 25.12.2015 [in Ukrainian].
13. Korotynskyi, O.E., Skopyuk, M.I. (2015) *Device for capacitor-discharge spot welding*. Pat. 9657 UA. Publ. 10.02.2015 [in Ukrainian].

Received 13.07.2021

# CHEMICAL EQUILIBRIUM IN Fe–O–H SYSTEM AT HIGH TEMPERATURES

M.M. Gasik<sup>1,2</sup> and M.I. Gasik<sup>2</sup>

<sup>1</sup>Aalto University

00076, Aalto, Espoo, Finland. E-mail: michael.gasik@aalto.fi

<sup>2</sup>National Metallurgical Academy of Ukraine

4 Gagarin Prosp., 49000, Dnipro, Ukraine

The issue of thermodynamic equilibrium in Fe–O–H system at the temperature of steel-making processes (1600 °C) was considered. The historical data array, features of experiments on obtaining them and their drawbacks were analyzed. A new more correct calculation of hydrogen and oxygen concentration in liquid iron and in the gas phase was performed. New coefficients of activity were calculated, proceeding from precise thermodynamic principles, unlike the earlier used artificial models based on interaction parameters. 19 Ref., 6 Figures.

*Keywords:* thermodynamics; iron; hydrogen; oxygen; solutions; activity; equilibrium

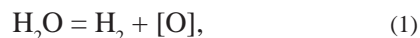
Interaction in Fe–O–H system, together with Fe–O–C system, is fundamental in steel production [1–3]. This system has been studied in great detail for the conditions of reduction of iron oxides in the solid phase and in less detail for interaction of liquid iron with the gas phase. In the latter case, most of the known fundamental studies were focused either on determination of hydrogen solubility in liquid iron, or of oxygen solubility, using a gas mixture of H<sub>2</sub>O–H<sub>2</sub> [3]. Despite the importance of the data on interaction in this system, in publications there is practically no detailed diagram of phase equilibrium at high temperatures (for instance, 1600 °C) or any consistent data on hydrogen or oxygen activities, when they are simultaneously present in liquid iron. The majority of these data (obtained in the previous century) use artificial simplified models of the solutions with application of interaction parameters, which do not have an appropriate and substantiated thermodynamic base [2–4]. The differences in previous experiments and the then applied analytical methods do not allow plotting the respective phase diagrams, based on such data.

In order to develop a thermodynamically substantiated approach to equilibrium in this system, in this work the available data on hydrogen and oxygen concentration in liquid iron were analyzed, and new calculations were performed and respective diagrams were plotted.

**Known experimental data.** One of the first studies of hydrogen and oxygen solubility in iron were the works by Hamilton and Vacher [5, 6]. They used a gas-vapour mixture of H<sub>2</sub>O–H<sub>2</sub> as an auxiliary sub-

stance to study oxygen solubility in parallel with investigations of Fe–O–C system equilibrium. They also took the first measurements of hydrogen content and came to the conclusion that its quantity is quite insignificant, and has no influence on oxygen content. Compared to measurements taken 30–40 years later, it is clear that in these experiments [5, 6] the exact hydrogen content could not be measured, using the methods available in those times.

Development of the theory and technology of steel production was accompanied by a series of investigations of hydrogen and oxygen solubility, due to higher requirements made of the steel quality [2], in particular, for railway transport [7]. More detailed measurements at that time, taken at different temperatures, and, what is important, at different argon and hydrogen ratios in H<sub>2</sub>O–H<sub>2</sub>–Ar gas phase, are given in work [8]. They determined the formal constant of equilibrium of the following reaction



showing that it is not steady, but depends on H<sub>2</sub>O/H<sub>2</sub> and Ar/H<sub>2</sub> ratio [8]. However, the researchers did not pay enough attention to the question of how exactly does the Ar/H<sub>2</sub> ratio influence either the equilibrium of reaction (1), or hydrogen solubility in iron.

In a parallel study [9], the authors noted the influence of Ar/H<sub>2</sub> ratio not only on hydrogen content, but also on oxygen concentration, even though in the conditions of a limited concentration range. In work [10], the authors added more experimental points in this system at higher values of H<sub>2</sub>O/H<sub>2</sub> ratio at Ar/H<sub>2</sub> = 5. Later on in work [11] the limit of hydrogen sol-

ubility in liquid iron was determined at 1600 °C in 25.9 ppm (or 10<sup>-4</sup> %) or in 0.00142 mole fractions, if iron is in equilibrium with pure hydrogen at the pressure of 1 Atm.

In work [12] the authors noted the fact that it is incorrect to consider the thermodynamics of just reaction (1), ignoring hydrogen solubility in iron, simultaneously with oxygen, even if its concentration is low. They synchronously analyzed the content of hydrogen and oxygen in iron in equilibrium with H<sub>2</sub>O–H<sub>2</sub> gas phase, but without argon additives (Ar/H<sub>2</sub> = 0). Figure 1 shows the results of these and other experimental measurements. As one can see from this data, in the experiments in [8] hydrogen concentration in the solution was practically unchanged, despite the variation of partial pressure of water vapour. This does not agree well with other independent data [9, 10, 12], possibly because in work [8], the Ar/H<sub>2</sub> ratio was not kept constant.

Despite all these works, a very simplified approach, based solely on reaction (1) almost without exception, predominated in the theory of steel-melting processes [1, 13] for a long time. In work [4] it is shown that such an approach is incorrect from the viewpoint of the rule of phases, as it ignores the presence of other components in the system. Application of a similar approach to Fe–O–C system showed that taking into account CO<sub>2</sub> and CO simultaneously much better agrees with the experiments, than when it is just CO. It is worth noting that the need to measure CO<sub>2</sub> alongside CO, was shown already in 1930s [5, 6], but this fact was not considered any further in terms of the process thermodynamics.

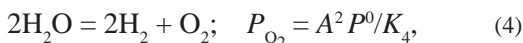
**Formalism of equilibrium in Fe–O–H–Ar system.** Available results can be first described by the balance of masses. We will assume that all the main components of the gas phase are ideal:

$$P_{H_2} + P_{H_2O} + P_{O_2} + P_{Ar} = P^0, \quad (2)$$

where  $P^0$  is the total pressure (1 atm). Introducing designations  $A = P_{H_2O}/P_{H_2}$ ,  $B = P_{Ar}/P_{H_2}$ , we can write (2) as follows:

$$P_{H_2} (1 + A + B) = P^0 - P_{O_2}. \quad (3)$$

As at high temperatures the equilibrium in the gas phase is practically instantaneous, the partial pressure of oxygen can be determined through the constant of the reaction of water vapour dissociation:



which has been assessed in detail many times. At 1600 °C by the data of [1, 12]  $\lg K_4 = 8.000-8.0827$ , and by the new data  $\lg K_4 = 7.97161$  (thermodynamic data base «FactSage 8.0», 2020). Thus, the partial

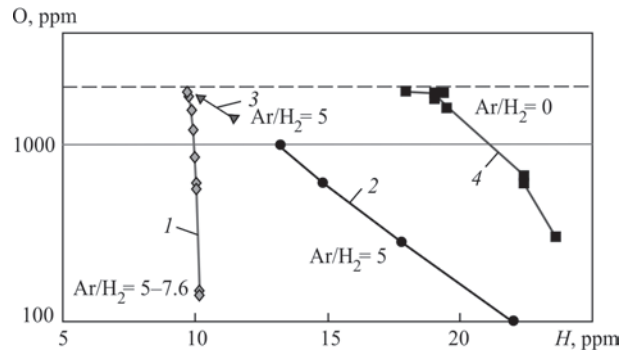


**Figure 1.** Experimental data (1 — [8]; 2 — [9]; 3 — [10]; 4 — [12]) on oxygen and hydrogen content in liquid iron at 1600 °C. Horizontal line shows the limit of oxygen solubility

pressure of hydrogen and oxygen in any mixture will be defined as follows:

$$\begin{aligned} P_{H_2} &= P^0 (1 - A^2/K_4)/(1 + A + B); \\ P_{O_2} &= A^2 P^0 / K_4. \end{aligned} \quad (5)$$

An interesting conclusion can be made from formula (5): partial pressure of oxygen does not depend on  $B$  (Ar/H<sub>2</sub> ratio), unlike partial pressure of hydrogen, which depends both on Ar/H<sub>2</sub> and on H<sub>2</sub>O/H<sub>2</sub>. It accounts for the discrepancies (Figure 1) in the experimental results with argon application.

Hydrogen and oxygen in the gas phase interact with liquid iron in proportion to their concentrations, forming Fe–[H]–[O] solution. In this case we assume that Ar does not dissolve in liquid iron, and then the content of hydrogen and oxygen will be proportional to activities of these components in equilibrium with partial pressures of hydrogen and oxygen. The component activity (or coefficient of activity ( $\gamma_i$ )) is a measure of effectiveness in a particular solution in terms of its reactions with other components. A classical definition of the activity links it with partial pressure of the dissolved component in the solution relative to its reference state, as a pure substance:

$$a_i(X_i) = P_i(X_i) / P_i^0, \quad (6)$$

where  $P_i$  is the partial pressure of this component;  $P_i^0$  is its pressure in the reference state ( $a_i^0 = 1$ ). Many thermodynamic calculations take a default reference state, designed for a pure substance. However, for a metallurgical system at 1600 °C, the pure liquid oxygen is not a reference state, as it cannot exist in such a form. It was shown [16, 17] that such hypothetical reference states, which earlier were used in metallurgical practice for years, lack thermodynamic and mathematical substantiation [14]. In the thermodynamics of metallurgical processes, the Wagner–Lupis–Elliott formalism was traditionally used with expansion of the coefficient of activity into the Taylor series [3, 4, 14], when the reference state was selected to be the

formal composition of the solution with 1 wt.% of the component (even if such a solution did not actually exist). However, the Taylor series expansion is only valid around a point, where the derivative with respect to concentration is taken [17], and it cannot be extrapolated on the whole to a wide concentration range. Work [18] showed that the traditional Wagner–Lupis–Elliott equations are invalid with respect to the basic Gibbs–Duhem equation [19]. The authors of [17] showed the five main principles for correct selection of the reference state and calculation of the chemical potential, and proved that the reference state of a component in a solution is its solubility limit under

these conditions, as all the required thermodynamic and mathematical conditions are fulfilled only there.

Thus, for hydrogen the reference state at 1600 °C is in place at its maximum content in iron (25.9 ppm) at equilibrium with pure hydrogen at the pressure of 1 atm [11], while the reference state for oxygen (maximum oxygen content of approximately 0.20 %) is observed at equilibrium with such a gas mixture, for which the partial pressure of oxygen reaches  $5.11 \cdot 10^{-9}$  atm (contact with pure oxygen would have led to complete transformation of iron into oxides). These maximum concentrations correspond to activities, equal to 1 for hydrogen and oxygen, as:

- Gibb’s energy function is continuous and differentiated by the quantity of substance added to the solution phase, when this solution is present (is not hypothetical);
- component activities are real, measurable and continuous, monotonically growing functions in the solution phase (saturation state is reached within the appropriate concentration range);
- in the saturated state the derivatives for component activity by temperature and by pressure are zero.

Correct determination of the activities and free energy enable calculating the detailed equilibrium in Fe–O–H system.

**Numerical thermodynamic calculation in Fe–O–H system.** Thermodynamic calculation will be performed, using «FactSage 8.0» software and data bases. The formal diagram of phase equilibrium in this system at 1600 °C was first calculated in mole fractions (Figure 2). One can see two phase regions from the iron side: metal-gas or metal-gas-slag (liquid iron oxides). If oxygen content is not high, and that of hydrogen is practically absent, then the third possible phase (iron-slag) can be in equilibrium with iron without any evident gas phase (Figure 2, b). The same diagram was calculated in weight percent (Figure 3). One can see that the line of equilibrium between slag (FeO) and liquid iron is almost horizontal, that points to practically unchanged oxygen solubility limit, despite an increase of hydrogen content to a concentration of approximately 0.0019 % [H]. Further increase of hydrogen in the system leads to an abrupt drop of oxygen content in iron.

The next calculation was made for the case of added argon at  $Ar/H_2 \approx 0.1–0.2$  and 5.0–6.0 under other conditions being equal (Figure 4). As argon concentration has little influence on oxygen content, the dependence of hydrogen content on  $Ar/H_2$  was assessed at different  $H_2O/H_2$  (Figure 5).

This hydrogen content can be approximated by a regression equation in Figure 5, which predicts hydrogen concentration the more accurately, the higher

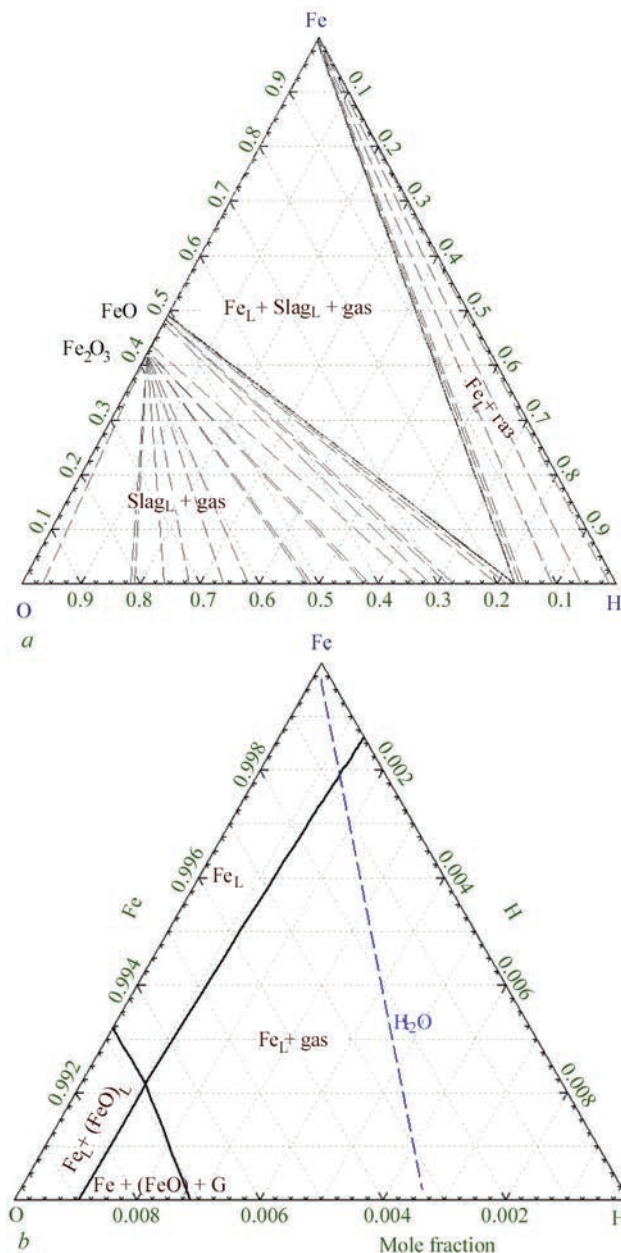


**Figure 2.** Diagram of phase equilibrium in Fe–O–H system at 1600 °C (a) and angle from the iron side, as component (b), using correct chemical potentials [17]. Dash line determines the stoichiometry of water vapour (mole ratio of hydrogen to oxygen is equal to 2)

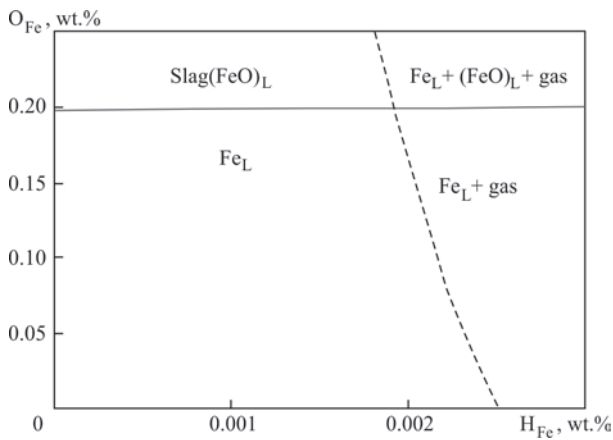


**Figure 3.** Phase equilibrium diagram in Fe–O–H system at 1600 °C. Regions of stability of different phases are shown

is  $B = \text{Ar}/\text{H}_2$  ratio. It is logical, as at low argon content ( $B \rightarrow 0$ ) the quantity of hydrogen in the solution will strongly depend on  $A = \text{H}_2\text{O}/\text{H}_2$  (by expression (5)). At  $B$  increase, particularly at  $B > A$  the hydrogen content will be mostly determined exactly by  $\text{Ar}/\text{H}_2$  ratio (it is rational to note that at 1600 °C the maximum value of  $A < 0.5\text{--}0.75$ , when iron oxides, i.e. slag, still do not form). In previous experiments (see Figure 1) using argon, the values of  $B = 5.0\text{--}7.6$ , that also accounts for considerable differences in the measured hydrogen concentrations at similar  $\text{H}_2\text{O}/\text{H}_2$  values.

The next question was determination of the coefficients of hydrogen and oxygen activity in the solution. The direct approach uses the ratio of component activity to its concentration in mole fractions and does not require any artificial models of the solutions [12, 14, 16, 17]. In keeping with equation (6) in the reference state ( $a_i = 1$ ), the coefficient of activity of any component ( $\gamma_i^0$ ), which will be equal to its reverse saturated concentration ( $X_i^0$ ):

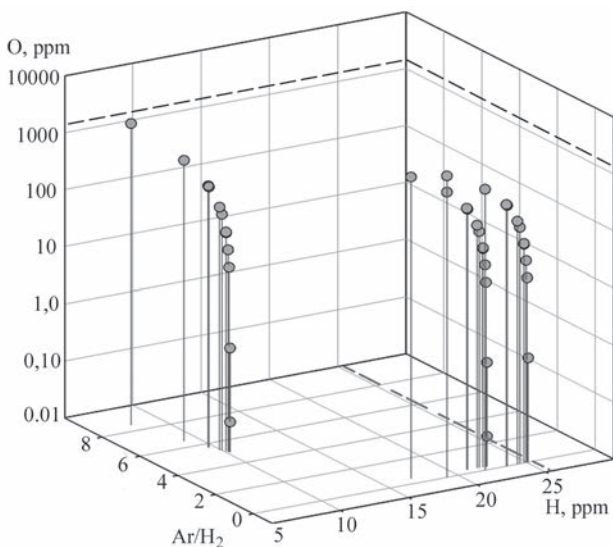


**Figure 4.** Oxygen and hydrogen content in Fe–O–H system at 1600 °C for different  $\text{Ar}/\text{H}_2$  ratios. Dash lines show the solubility limits of hydrogen and oxygen

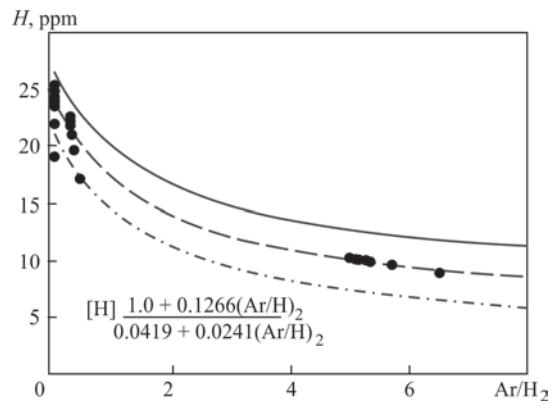


**Figure 5.** Hydrogen content in Fe–O–H system at 1600 °C (Figure 4) for different  $\text{Ar}/\text{H}_2$  ratios. Dash lines show the confidence interval for the regression equation

$$\gamma_i^0 = 1/X_i^0 \tag{7}$$

Coefficients of activity of hydrogen and oxygen change, depending on  $\text{Ar}/\text{H}_2$  and  $\text{H}_2\text{O}/\text{H}_2$  ratios within narrow limits, but nonlinearly (Figure 6). The first ratio has a stronger impact on the coefficient of oxygen activity and much less on the coefficient of

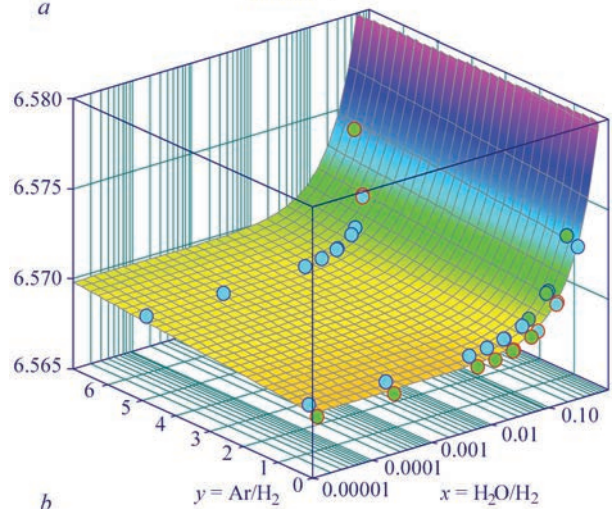
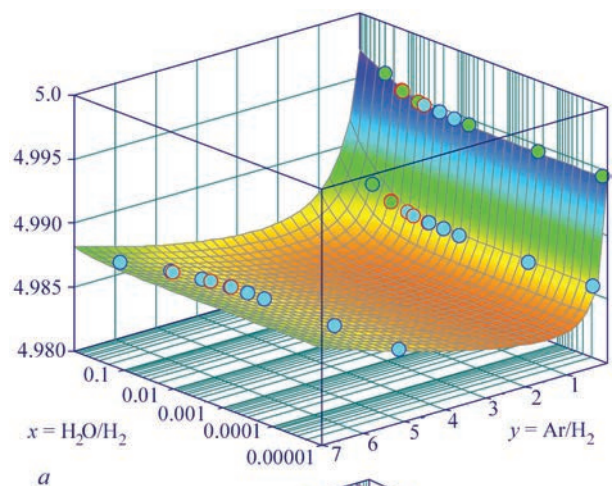


**Figure 6.** Natural logarithms of the coefficients of activity of oxygen  $\ln(\gamma_O) = (a + bx + cy + dy^2)/(1 + ex + fy + gy^2)$ :  $a = 4.9944208$ ;  $b = 11.13995$ ;  $c = 32.451068$ ;  $d = -0.88011301$ ;  $e = 2.2286863$ ;  $f = 6.515328$ ;  $g = -0.17770942$  (a) and hydrogen  $\ln(\gamma_H) = a + bx + cy$ :  $a = 6.5685561$ ;  $b = 0.016389753$ ;  $c = 0.00018215654$  (b) in liquid iron from  $\text{Ar}/\text{H}_2$  and  $\text{H}_2\text{O}/\text{H}_2$  ratios at 1600 °C

hydrogen activity. The second has an opposite effect: has a stronger influence on the coefficient of activity of hydrogen, and not oxygen, as it could have been anticipated. One can see from regression equations in Figure 6, that the influence of  $y = \text{Ar}/\text{H}_2$  and  $x = \text{H}_2\text{O}/\text{H}_2$  ratios on the coefficient of activity of hydrogen, is independent on the other, i.e. there is no correlation between the influence of these ratios (Figure 6, *b*). For oxygen, contrarily, the simultaneous impact of these ratios of the coefficient of activity is in place (Figure 6, *a*). Approximating the surfaces and equations, a nonlinear regression was plotted by points, calculated in this work.

Thus, we can note that hydrogen content in liquid iron, which is controlled by  $\text{Ar}/\text{H}_2$  and  $\text{H}_2\text{O}/\text{H}_2$  ratios simultaneously, influences the coefficient of activity of oxygen and its concentration stronger that it was earlier believed. A similar influence on the coefficient of activity of hydrogen is smaller, and it depends more on  $\text{H}_2\text{O}/\text{H}_2$ , as does hydrogen concentration at smaller  $\text{Ar}/\text{H}_2$  values.

### Conclusions

1. Analysis of the known experimental data on interaction of Fe–O–H–Ar system was performed, as well as calculations of phase equilibrium diagram, using new data, allowing for correct determination and calculation of the component activity.

2. It is shown that partial pressure of oxygen in the gas phase is independent on  $\text{Ar}/\text{H}_2$  ratio, unlike partial pressure of hydrogen, which depends both on  $\text{Ar}/\text{H}_2$ , and on  $\text{H}_2\text{O}/\text{H}_2$ . It accounts for the available discrepancies in the results of historical experiments, using argon.

3. Hydrogen content in liquid iron can be approximated by a regression equation, which predicts hydrogen concentration the more accurately, the higher is the  $\text{Ar}/\text{H}_2$  ratio. At a low content of argon the quantity of hydrogen will strongly depend on  $\text{H}_2\text{O}/\text{H}_2$ , and in the opposite case the hydrogen content will be mostly determined exactly by  $\text{Ar}/\text{H}_2$  ratio.

4. The coefficients of activity of hydrogen and oxygen change depending on  $\text{Ar}/\text{H}_2$  and  $\text{H}_2\text{O}/\text{H}_2$  ratios in narrow ranges, but nonlinearly. The first ratio has a stronger influence on the coefficient of activity of oxygen and a much weaker one on that of hydrogen. The second has an opposite effect: it influences the

coefficient of activity of hydrogen more than that of oxygen, as one might have foreseen.

5. Investigation results are of practical importance for controlling the hydrogen and oxygen content at steel treatment by argon-based gas mixtures in the presence of water vapour. This approach can be extended to alloyed steels and alloys of different composition.

1. Filippov, S.I. (1967) *Theory of metallurgical processes*. Moscow, Metallurgiya [in Russian].
2. Velichko, A.G. (2005) *Out-of-furnace steel treatment*. Dnepropetrovsk, Sistemnye Tekhnologii [in Russian].
3. Okhotsky, V.B., Kostyolov, O.L., Simonov, V.K. (1997) *Theory of metallurgical processes*. Kyiv, IZMN [in Ukrainian].
4. Knyuppel, G. (1973) *Deoxidation and vacuum treatment of steel*. Moscow, Metallurgiya [in Russian].
5. Vacher, H.C. (1933) The system liquid iron–carbon oxides. *US Bureau of Standards J. Res.*, **11**, 541–551.
6. Vacher, H.C., Hamilton, E.H. (1931) Carbon–oxygen equilibrium in liquid iron. *Transact. AIME*, **95**, 124–140.
7. Kozlovsky, A.I., Medovar, B.I., Projdak, Yu.S. et al. (1999) Application of methods of special electrometallurgy and out-of-furnace treatment in production of wheel steel. *Problemy Spets. Elektrometallurgii*, **2**, 31–38 [in Russian].
8. Sakao, H., Sano, K. (1960) Equilibrium between dissolved oxygen in liquid iron and  $\text{H}_2$ – $\text{H}_2\text{O}$  gas mixtures. *Transact. JIM*, **1**, 38–42.
9. Schenck, H., Wunsch, H. (1961) Über die Gleichgewichtslöslichkeit des Wasserstoffs im flüssigen reinen Nickel und Eisen und die Beeinflussung im Eisen durch Sauerstoff. *Arch. Eisenhüttenw.*, **32(11)**, 779–790.
10. Gasik, M.I., Khitrik, S.I. (1965) Interaction of liquid iron with vapor-hydrogen mixture. *Metallurgiya i Koksokhimiya*, **3**, 5–16 [in Russian].
11. Ban-ya, S., Fuwa, T., Ono, K. (1967) Solubility of hydrogen in liquid iron alloys. *Tetsu-to-Hagane*, **53**, 13–28.
12. Kubaschewski, O., Alcock, C.B. (1979) *Metallurgical thermochemistry*. 5<sup>th</sup> Ed. Pergamon Press, Oxford.
13. Sanbongi, K. (1981) Thermodynamics of ironmaking and steelmaking processes. *Transact. JIM*, **22**, 663–676.
14. Lupis, C.H.P. (1983) *Chemical thermodynamics of materials*. North-Holland, NY.
15. Gasik, M.M., Gasik, M.I. (1985) Thermodynamic investigation of hydrogen–oxygen equilibrium in liquid iron. *Izv. AN SSSR. Metally*, **3**, 22–30 [in Russian].
16. Gasik, M. (2013) *Handbook of Ferroalloys: Theory and Technology*, Elsevier. Butterworth-Heinemann, Oxford, UK.
17. Gasik, M.M., Gasik, M.I. (2020) Chemical potentials and activities in metallurgical processes. *Suchasna Elektrometallurhiya*, **4**, 39–43 [in Ukrainian].
18. Hillert, M. (1998) *Phase equilibria, phase diagrams and phase transformations: Their thermodynamic basis*. Cambridge Univ. Press, Cambridge, UK.
19. Schuhman, R.Jr. (1955) Application of Gibbs–Duhem equations to ternary systems. *Acta Metall.*, **3**, 219–226.

Received 26.04.2021

# THREE-DIMENSIONAL VISUALIZATION OF THE DETECTED DEFECTS BY EDDY CURRENT COMPUTING TOMOGRAPHY

O.O. Vertiy<sup>1</sup> and V.M. Uchanin<sup>2</sup>

<sup>1</sup>National Aerospace University «Kharkiv Aviation Institute»  
17 Chkalov Str., 61070, Ukraine. E-mail: alexey.vertiy@gmail.com

<sup>2</sup>G.V. Karpenko Physico-Mechanical Institute of NASU  
5 Naukova Str., 79060, Lviv, Ukraine. E-mail: vuchanin@gmail.com

Nondestructive computing tomography methods based on different physical phenomena are reviewed as an effective tool to solve many NDT problems in the context of NDE 4.0 revolution. Eddy current (EC) tomography principle and experimental set-up are presented to demonstrate the possibility to reconstruct tomography images related to the distribution of material electric conductivity. A riveted joint of two aluminium alloy sheets with 2 mm long artificial crack-like defects was selected as an example of complex enough inspected structure. Investigations were carried out with two types of eddy current probes (ECP) application: the first one — the traditional EC probe of absolute type with coaxial driving and sensing coils, and the second — low-frequency double differential EC probe of MDF 1201 type. The set of vertical (orthogonal to the inspected surface) slices for the rivet zone were obtained to demonstrate the effectiveness of EC tomography. The horizontal slices were analyzed to demonstrate the possibility to produce tomography images at different depths. Two-layer structures, consisting of upper sheets with thicknesses from 0 to 8 mm and 5 mm thick lower sheath with a cracklike defect were applied to reconstruct the vertical tomography slices using double differential EC probes. The latter results demonstrate the great depth of evaluation with application of ECP of double differential type and the possibility to estimate the detected defect size and distance from the inspected surface. 34 Ref., 8 Figures.

*Keywords:* eddy current (EC) tomography, eddy current probe (EC probe), double differentiation EC probe, electric conductivity, tomography images, slices, riveted joints

The fourth industrial revolution gradually acquires real meaning, as indicated by numerous publications [1, 2]. Fully automated plants, built on Industry 4.0 principles with real-time control of all the processes, are already in operation. The respective government programs are in place in the majority of industrialized countries. Unfortunately, Ukraine is still far behind this global trend, even though some leaders do appear here too [3].

It is obvious that the coming restructuring of industry cannot avoid the need to form new approaches in nondestructive evaluation (NDE) and the world NDE community is already actively discussing this topic, proclaiming formation of the 4<sup>th</sup> revolution in NDE under the abbreviation of NDE 4.0 (Nondestructive evaluation 4.0) [4, 5]. Reviewing these studies is not the objective of this paper. We will only note that one of the directions in development of NDE 4.0 technologies is automation of testing operations (also using robots) and intellectualization of the control means. We will state with cautious optimism that local specialists on eddy current evaluation have certain achievements in this direction [6–8]. A series of automated systems (including robotic system) have been designed, and new approaches have been developed to processing signals from eddy current probes (ECP) [6–9].

NDE methods, based on tomographic principles of data processing and presentation, can be definitely regarded as NDE 4.0 technologies. The most widely accepted NDE methods, based on probing the evaluated object (EO) by external fields of different nature, are gradually getting tomographic realizations.

The first mathematical tomographic algorithms were used in X-ray radiation range, characterized by an exponential decay law. X-ray computer tomography (CT) allows realization of NDE of OC inner structure by multiple X-ray transmissions in different directions with subsequent processing of the projection data and plotting a 3D distribution of the degree of radiation attenuation. X-ray CT for medical applications was invented for the first time by Godfrey Hounsfield, British inventor, who was granted the respective patent [10] in 1972, and already in 1979, together with Alan Kormak he won the Nobel Prize in physiology and medicine for «Development of computer tomography». And industrial tomography, as an NDE method, emerged already as a projection of the success of medical CT. At present, X-ray CT is the most widely used method of tomographic plotting of images of the internal structure in medicine and industrial NDE [11–14]. This development led to that application of X-ray CT at NDE is regulated by

a series of international standards (EN 16016-1(2,3)-1(2,3):2011), starting from 2011.

Achievement in ultrasonic CT became the next tomographic «stronghold», where we can mention the results obtained by scientists of G.V. Karpenko Physico-Mechanical Institute of NASU [15–18]. With time, it was the turn of electric (resistive) and electromagnetic (including eddy current) methods [19–28]. Here, the priority belongs to the results of the representatives of Ukraine, obtained in the Turkish-Ukrainian International Laboratory of High Technologies of «Marmara» Research Center (Hebze, Turkey). Here, theoretical approaches were used, developed earlier for UHF range [20–22]. It is important that in addition to formulation of the theoretical principles, a series of experimental results were derived [19, 23–24], which showed that practical implementation of eddy current tomography (ECT) approaches will allow raising the eddy current NDE method to a fundamentally new level. Note that foreign studies on ECT are still of a theoretical stage, and have not reached the experimental level [28].

The objective of this paper is presentation and generalization of developments on eddy current computational tomography.

**Principle of eddy current tomography.** Restoring the distribution of specific electric conductivity (SEC) in any EO cross-slice is based on an integral equation of tomography [19–22]:

$$\frac{\hat{\psi}(v, y_1) \exp(i\gamma_1 y_1)}{c_1(v)} = \iint_S K(x', y') \exp[-2\pi i(\alpha x' + \beta y')] dx' dy', \quad (1)$$

where  $\hat{\psi}(v, y_1)$  is the Fourier-transformation of a complex scattered field  $\psi(x, y)$ , measured above the surface of the studied environment on the scanning line  $y = y_1$ ;  $v$  variable is the spatial frequency;  $c_1[\gamma_1(v), \gamma_2(v)]$  is the complex function of  $v$ ;  $\gamma_1$ ;  $\gamma_2$ , and  $\beta$  are the complex functions of  $v$  in the general case;  $\alpha$  is the real-valued function of  $v$ ;  $K(x', y')$  is the unknown (sought) normalized distribution of current in  $S$  domain (EO transverse slice) that is the scattered field source. The studied domain was limited, so that the

integral in equation (1) can be considered in unlimited boundaries. Here, it is taken, that Fourier transformation of the scattered field does exist, as this field is considered in a limited space domain.

Solution of this integral equation allows defining  $K(x', y')$  function that describes the normalized current distribution in the studied transverse slice, perpendicular to the metal surface, and including the scanning line (vertical slice).  $K(x', y')$  function depends on operational frequency (frequency of the probing electromagnetic field). In tomography measurement and reconstruction of  $K(x', y')$  function are performed for a certain set of operational frequencies in a specified range. The tomographic image function is the module of the sum of these functions. It enables detecting the inhomogeneity of metal SEC in the vertical slice, including that associated with the presence of defects. Application of tomographic algorithm allows obtaining sufficiently high-quality images of the transverse slices of local (pore type) and extended (cracklike) defects. A set of images in different vertical (orthogonal relative to the surface of the object of inspection) transverse slices allows reconstruction of a 3D image of the studied EO zone.

**Experimental set-up for automatic evaluation by the principle of eddy current computing tomography.** Experimental set-up (Figure 1) consists of personal computer 1, eddy current block 2 to determine the signal components in the operational frequency range, control unit 3 with stepping motors 4 and 7 of scanning of ECP 6 along coordinates  $X$  and  $Y$ , which are a component of two-coordinate scanner 8, and studied specimen 5. Appearance of the set-up with a two-coordinate scanner, installed on the evaluated specimens, is shown in Figure 2.

Personal computer controls the operation of stepping motors of the two-coordinate scanner and eddy current block, records and stores the parameters (amplitude and phase) of ECP signals in discrete points of the evaluated zone at sixteen operational frequencies in the selected range, performs discretization and processing of signals by the developed tomographic algorithm and forms a colour presentation of the obtained results, which reproduces the two-dimensional distribution of SEC in the selected EO slices. Eddy current block functions as a conventional multifrequency flaw detector, which operates ECP of different types (absolute, differential, etc.). Its feature is fast switching of operational frequencies, required for realization of tomographic algorithms, and an improved compensation scheme, which allows widening the dynamic range during processing of ECP output signals. In the reconstructed tomographic images the EO homogeneous region was reproduced by blue colour, the zone of anomaly (defect) — by red colour and the transition zones — by green colour.

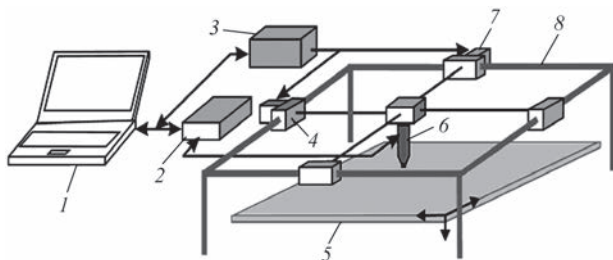


**Figure 1.** Diagram of experimental set up for eddy current tomography

Two types of ECP were used for experimental studies. The first is the traditional ECP of absolute type produced by Nortec Company, which consisted of two (driving and sensing) coaxial windings. The features of ECP of this type are described in a review [29], and those of spatial distribution of ECP signal from cracks of different length were analyzed in work [30]. Another, low-frequency double differentiation ECP of MDF-1201 type was developed at G.V. Karpenko Physico-Mechanical Institute of NASU [31]. ECP of double differentiation consists of two excitation windings connected in series and placed side by side, and two differentially connected sensing windings. Sensing windings are located in the neutral plane, where the electromagnetic field of excitation windings flows in the opposite direction, so that the total electromagnetic field of both the windings is absent, and eddy currents are added, contrarily. Such an ECP has four sensitivity zones for a local defect. Elongated defects form a «quasiabsolute» signal with maximum amplitude directly above the defects, as in the standard ECP of absolute type. A feature of this ECP is the great depth of testing that was reported in a series of publications [31, 32].

**Tomographic visualization of defects in the riveted joint.** Rivets are the most widely used element of multilayer aircraft structures, which are used for joining the connected skins, reinforcing plates, stringers, etc. At the same time, rivet welds of aircraft structures create the greatest number of stress raisers and thus require greater attention in service. Note that during detect detection in the riveted joint it is necessary to eliminate the effect of the rivet itself, which, essentially also is an admissible, in terms of design, large-sized defect and which creates additional interference signals. Therefore, the task of detecting fatigue cracks (particularly, internal), that form in operation in the riveted joint, is a real challenge for eddy current method developers. Nonetheless, we showed in our research that it is possible to create a range of no-alternative NDE technologies for riveted components on

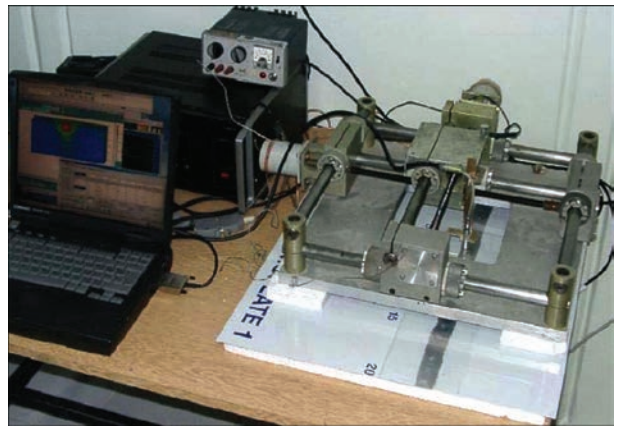


**Figure 2.** Appearance of an experimental set-up for eddy current tomography

the base of eddy current method, particularly when it is necessary to detect fatigue cracks in the rivet inner layers or under its head [33, 34]. In our experiment, a rivet with a defect was selected to show the capabilities in difficult cases.

A fragment of an aircraft two-layer skin was used for investigations, which has SEC value equal to 35.4 mS/m, with rows of rivets with artificial cracklike defects, made by electric erosion method. The thickness of each layer of the structure was equal to 2.5 mm. Rivet head diameter was 6 mm, and that of the rivet hole was 5 mm. The scheme of scanning zone of the selected rivet is shown in Figure 3, *a* (side view) and Figure 3, *b* (top view). Rectangular slice of two-dimensional scanning (frame) for an individual rivet was selected equal to 10 mm along coordinate *X* and 15 mm along coordinate *Y* (marked by gray colour in Figure 3). Figure 3, *a* shows that in the selected design the rivets were placed in special recesses, so that a slot formed between the sheath material and the rivet body.

**Results obtained with application of traditional ECP of an absolute type.** The process of obtaining tomographic images in different slices, corresponding to different scanning lines, and different ECP positions relative to the rivet, respectively, is shown in Figure 4. The numbers denote the coordinates on axes *X* and *Y*. The re-

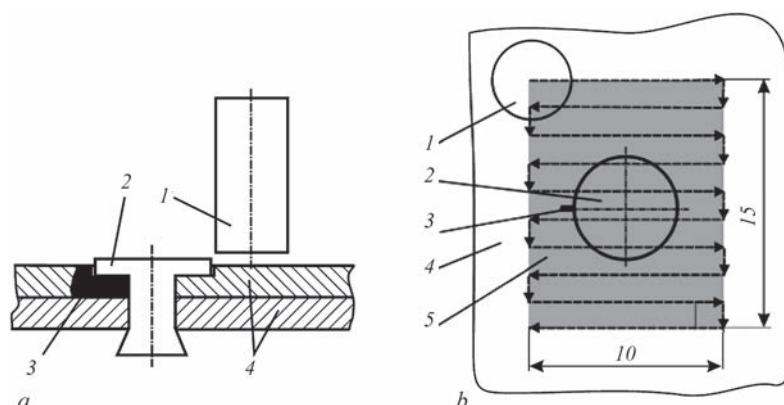


**Figure 3.** Scheme of riveted joint scanning: 1 — ECP; 2 — rivet; 3 — defect; 4 — two-layer structure; 5 — scanned region

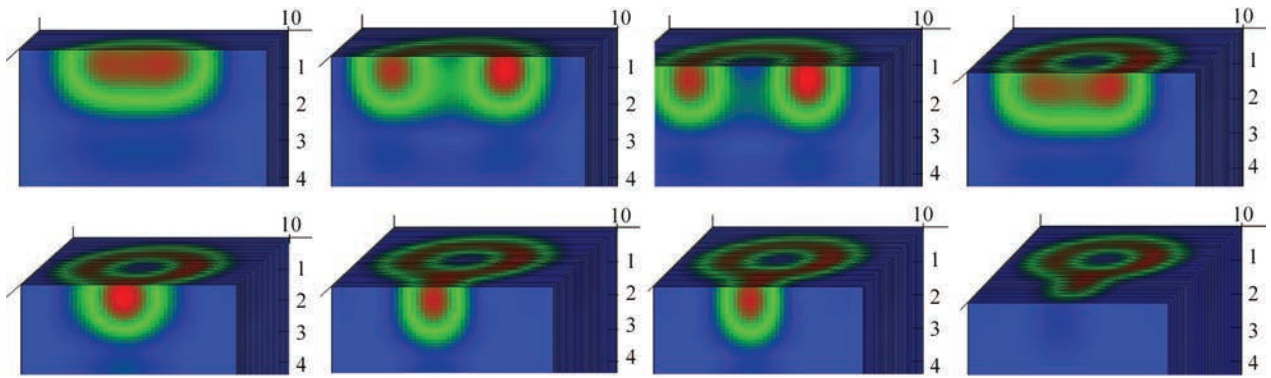


**Figure 4.** 3D tomographic images of the riveted joint with a defect in different vertical slices

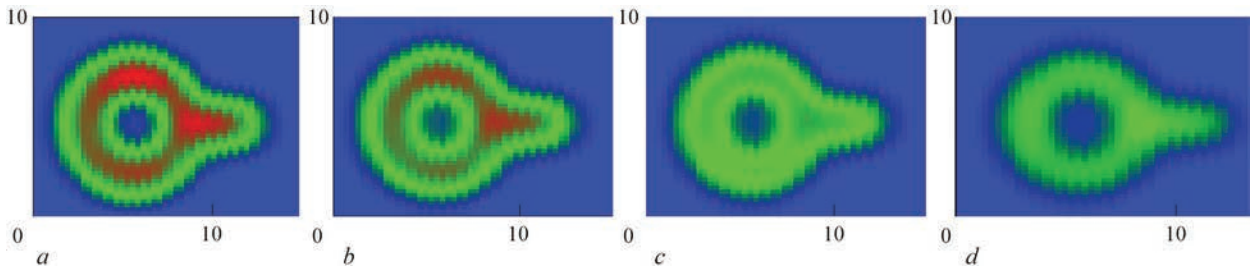


**Figure 5.** Tomographic reconstruction of the horizontal slice of the riveted joint with a defect at the depth of: 0 (a); 0.9 (b); 1.2 (c), 1.5 mm (d), using traditional ECP of an absolute type

sults were obtained by calculation of the amplitude and phase of ECP signal in sixteen operational frequencies in the range from 5 to 50 kHz. The coordinates in the direction normal to the surface (in-depth of the sample) are shown on the right in each image.

After completion of scanning of the selected region, horizontal slices were obtained, which correspond to SEC distribution at different depth. The reconstructed tomographic images are shown in Figure 5.

Developed algorithms allow studying and analyzing different slices of the evaluated zone after completion of the scanning process. As an example, Figure 6 gives a 3D tomographic image of the riveted joint, when the control zone slice was selected along the defect.

The given results also show that when applying the traditional ECP of absolute type in the operational frequency range from 5 to 50 Hz, horizontal tomographic images can be obtained at the depth down to 1.5 mm. Note that similar studies conducted in the operational frequency range from 100 kHz to 1.0 MHz,

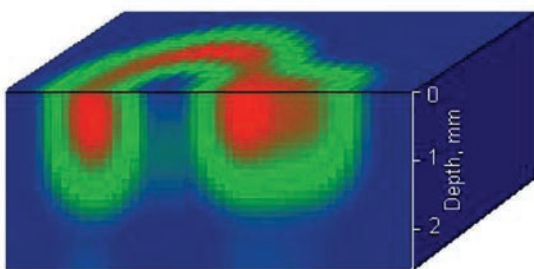


**Figure 6.** 3D tomographic image of the riveted joint with a vertical slice along the defect

allow reaching the control depth of just 0.2 mm, that can be readily attributed to a stronger skin-effect.

**Results of control of the riveted joint, obtained using low-frequency ECP of double differentiation.** In the next experiment, a low-frequency ECP of MDF 1201 type was used [31]. Obtained results that characterize the horizontal slices at different depths to 3 mm for defectfree (above) and defective (below) rivets are given in Figure 7. Operational frequencies at application of this ECP were varied in the range of 0.9–10 KHz.

Tomographic images of horizontal slices for a defectfree rivet (Figure 7, a, b, c) have a characteristic four-lobe form, corresponding to the four sensitivity zones of ECP of double differentiation type [31]. Presence of a cracklike defect distorts the four-lobe image, characteristic for a defectfree rivet. The image becomes asymmetric and one lobe disappears. Such distortions were observed during traditional visualization of the results of riveted joint testing, when the 2D distribution of ECP signal was recorded on electrochemical paper [33]. Note that the testing depth here reached 3 mm that confirms the great depth of testing with application of this ECP.

**Vertical slices of electric conductivity distribution from subsurface defects of different depth.** Low-frequency ECP of MDF 1201 type was also used to conduct experiments with layered specimens with cracklike defects in the internal layers. Recall that for elongated defects of the type of cracks the signal from ECP of double differentiation type is of a

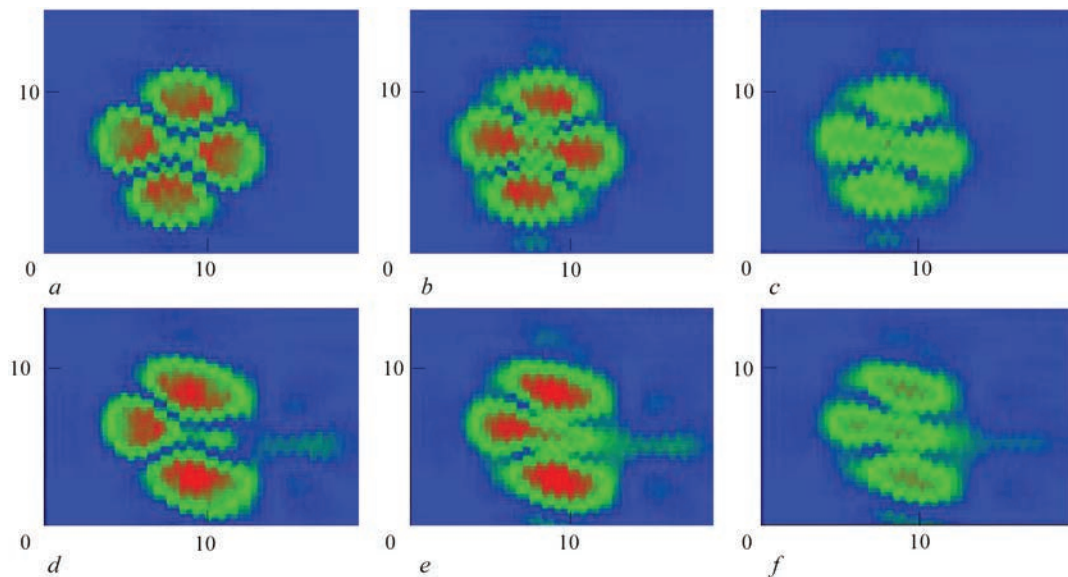


**Figure 7.** Tomographic image of a horizontal slice at different depths: 0 (*a, d*); 2.0 (*b, e*); 3.0 mm (*c, f*) during eddy current scanning of the zone of defectfree rivet (*a, b, c*) and rivet with a crack (*d, e, f*)

«quasiabsolute» nature that affects the obtained tomographic images. The crack was simulated by a butt of two aluminium plates 5.0 mm thick, which were placed on a base aluminium plate 5.0 mm thick. The specimen was covered from above by plates 1.5; 2.5; 5.0; 6.5 and 8.0 mm thick to change the defect depth. Layered specimens were scanned by ECP parallel to the surface by a linear trajectory 39.6 mm long. In order to reconstruct the vertical (normal to the surface) specimen slice, ECP signals were recoded in sixteen operational frequencies in the range of 0.9–10 KHz in each point every 0.6 mm along the scanning line. In the tomographic reconstructed images the homogeneous region was reproduced by blue colour, anomalous zone — by the red colour and the transition zones were shown by green colour. In the tomographic im-

ages of vertical slice of the layered specimens (Figure 8) the coordinates along the line of scanning over the specimen surface are shown on top in mm, and on the right are the coordinates in the direction normal from the surface (in-depth of the sample).

In the tomographic images of vertical slice, the anomalous zones that correspond to the defect, are marked by the red colour, their upper edge corresponding to the defect depth (upper plate thickness), which is counted by the right scale. The length of the red anomalous zone along the vertical in-depth of the metal corresponds to defect height (5.0 mm). An exception is the tomographic image of the specimen slice with the surface defect (without upper plate) (Figure 8, *a*), in which the anomalous zone separated into two regions. It is attributable to existence of side maximums for large-sized defects in

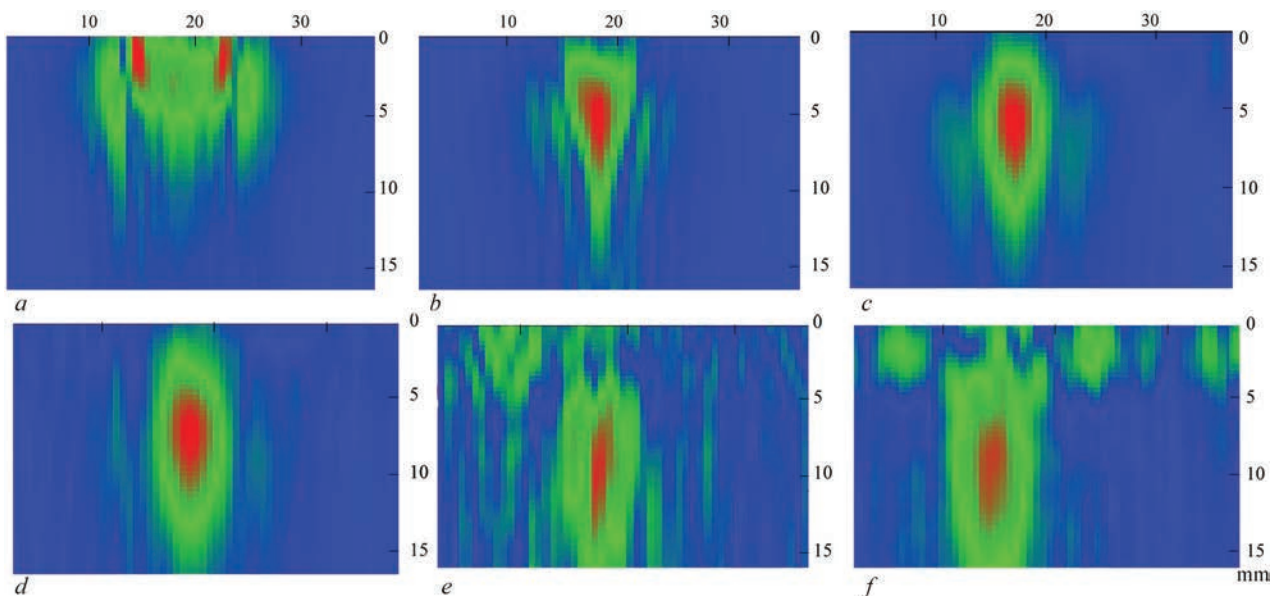


**Figure 8.** Reconstructed vertical slice of a sample for surface defect (*a*) and defects located at the depths of 1.5 (*b*), 2.5 (*c*), 5.0 (*d*), 6.5 (*e*), 8.0 mm (*f*)

ECP of double differentiation type. However, the vertical boundary of the red region in the image starts from the specimen surface, as could be anticipated. With increase of the defect depth, large green regions appear in the tomographic images that is related to greater sensitivity of inspection system, and interference level, accordingly. However, the red anomalous zone allows reliably identifying the defect, which is located at down to 8.0 mm depth. Moreover, the position of the defect lower edge is clearly visible, which for the deepest-lying defect corresponds to 13 mm distance from the surface.

The given results are indicative of the principal possibility of quantitative eddy current evaluation with assessment of the detected defect parameters, based on tomographic approaches. Moreover, the great depth of testing using ECP of MDF 1201 type was confirmed.

### Conclusions

1. A brief review of nondestructive methods of computer tomography is given, based on different physical phenomena, as an effective technique to solve numerous NDE problems in the context of NDE 4.0 revolution.

2. ECT principle and experimental set-up are presented for reconstruction of tomographic images, related to distribution of material electric conductivity.

3. Two ECP types were used for investigations: the first is a traditional ECP of absolute type with a coaxial sensing and driving windings, and the second is a low-frequency ECP of double differentiation.

4. ECT studies were performed on a two-layer specimen that consists of two plates of an aluminium alloy with rivets and 2 mm cracklike defects. A set of vertical slices (orthogonal relative to the inspected surface) were obtained for the riveted joint, which demonstrated ECT effectiveness. Tomographic images of horizontal slices at different depth were also analyzed.

5. Reconstruction of vertical tomographic slices with application of ECP of double differentiation was performed, using a multilayered structure, which consisted of an upper skin 0–8 mm thick and cracklike defects in the lower layer. Obtained results showed the great inspection depth at application of ECP of this type and possibility of assessment of the size of the detected defect and its distance to the inspected surface.

6. Application of ECT principles will allow raising the eddy current evaluation to a fundamentally new level. Resuming ECT investigations and developments can be regarded as a national priority.

*The authors would like to express their gratitude to academician Z.T. Nazarchuk, who promoted organization of joint research and cooperation of the authors.*

- Liao, Y., Deschamps, F., Loures, E.F.R., Ramos, L.F.P. (2017) Past, present and future of Industry 4.0 — a systematic literature review and research agenda proposal. *Intern. J. of Production Research*, **55**(12), 3609–3629. <http://doi.org/10.1080/00207543.2017.1308576>.
- Drath, R., Horch, A. (2014) Industrie 4.0: Hit or Hype. *IEEE Industrial Electronics Magazine*, **8**(2), 56–58. <http://doi.org/10.1109/mie.2014.2312079>.
- Yurchak, A. (2019) Far from the neighbours: why Ukraine lags behind in the sphere of industrial development 4.0. *Ekonomichna Pravda*. <https://www.epravda.com.ua/rus/columns/2019/11/5/653346>.
- Singh, R. (2019) The next revolution in nondestructive testing and evaluation: What and how. *Materials Evaluation*, **77**(1), 45–50.
- Vrana, J. (2020) NDE Perception and emerging reality: NDE 4.0 value extraction, *Materials Evaluation*, **78**(7), 835–851.
- Naida, V.L., Uchanin, V.N., Mozhukhin, A.A. et al. (2008) Development of elements of a system of automated eddy current testing of collector bridges in nuclear power plants. *Tekhn. Diagnost. i Nerazrush. Kontrol*, **3**, 21–24 [in Russian].
- Lutcenko, G., Uchanin, V., Mischenko, V., Opanasenko, A. (2012) Eddy currents versus magnetic particles. In: *Proc. of 18<sup>th</sup> World Conf. on Nondestructive Testing*, Durban, www.ndt.com.
- Dolinenko, V.V., Shapovalov, E.V., Skuba, T.G. et al. (2017) Robotic system of non-destructive eddy-current testing of complex geometry products. *The Paton Welding J.*, **5–6**, 60–67. <http://doi.org/10.15407/as2017.06.10>.
- Lysenko, Ju., Eremenko, V., Kuts, Yu. et al. (2020) Advanced signal processing methods for inspection of aircraft structural materials. *Transact. on Aerospace Research*, **2**(259), 27–35. <http://doi.org/10.2478/tar-2020-0008>.
- Hounsfield, G. N. (1972) *A method and apparatus for examination of a body by radiation such as X-ray or gamma radiation*. British Pat. 1283915. British Patent Office, London.
- Vajnberg, E.I., Klyuev, V.V., Kurozaev, V.P. (1986) *Industrial X-ray computed tomography*: Book. Devices for non-destructive testing of materials and products: Refer. book. Ed. by V.V. Klyuev. 2<sup>nd</sup> Ed., Moscow, Vol. 1 [in Russian].
- Vajnberg, E.I., Kazak, I.A., Kurozaev, V.P. (1981) Reconstruction of internal space structure of objects by integral projections in real time. *DAN SSSR*, **257**(1), 89–94 [in Russian].
- Reimers, P., Goebbels, J. (1983) New possibilities of non-destructive evaluation by X-ray computed tomography. *Materials Evaluation*, **42**(6), 732–737
- Maire, E., Buffiere, J., Salvo, L. et al. (2001) On the application of X-ray microtomography in the field of materials science. *Advanced Engineering Materials*, **3**(8), 539–546.
- Nazarchuk, Z.T., Koshovy, V.V., Krivin, E.V., Romanishyn, I.M. (1999) Ultrasonic tomography, technologies for NDT and monitoring of material degradation. In: *Proc. Joint EC IAEA Specialists Meeting on NDT Methods for Monitoring Degradation*. Petten, The Netherlands, 79–89.
- Koshovy, V. V., Nazarchuk, Z. T. (2001) Estimating the pre-defective state of a material using methods of ultrasonic computerized tomography. *Materials Sci.*, **37**(2), 279–293.
- Koshevoj, V.V., Romanishin, I.M., Romanishin, R.I., Sharamaga, R.V. (2010) Ultrasonic computer tomography based

- on recording of a signal scattered by material structure. Pt 1. *Tekh. Diagnost. i Nerazrush. Kontrol*, **2**, 37–42 [in Russian].
18. Koshevoj, V.V., Romanishin, I.M., Romanishin, R.I., Sharamaga, R.V. (2010) Ultrasonic computer tomography based on recording of a signal scattered by material structure. Pt 2. *Tekh. Diagnost. i Nerazrush. Kontrol*, **3**, 19–24 [in Russian].
  19. (2011) *Subsurface sensing*. Ed. by A.S.Turk, A.K., Hocaoglu, A.A. Vertiy, John Wiley & Sons, Inc.
  20. Vertiy, A., Gavrilov, S., Voynovskyy, I., Stepanyuk, V. (2002) The millimeter wave tomography application for the subsurface imaging. *Int. J. of Infrared and Millimeter Waves*. **23**(10), 1413–1444.
  21. Gavrilov, S.P., Vertiy, A.A. (1997) Application of tomography method in millimeter wavelengths band: I. Theoretical. *Int. J. Infrared Millimeter Waves*, **18**(9), 1739–1760.
  22. Vertiy, A.A., Gavrilov, S.P. (1997) Application of tomography method in millimeter wavelengths band: II. Experimental. *Int. J. Infrared Millimeter Waves*, **18**(9), 1761–1781.
  23. Vertiy, A., Gavrilov, S., Voynovskyy, I. et al. (2004) Subsurface imaging by deep penetrating eddy current tomography. *Fizychni Metody ta Zasoby Kontrolyu Seredovyshch, Materialiv ta Vyrobov*, **9**, 123–127 [in Russian].
  24. Vertiy, A.A., Gavrilov, S.P., Voynovskyy, I.V. et al. (2004) Deep penetrating eddy current tomography for subsurface imaging. In: *Proc. of 10<sup>th</sup> Int. Workshop on Electromagnetic Evaluation*. Michigan, USA. 91–92.
  25. Tamburrino, A. Rubinacci, G. (2002) A new non-iterative inversion method for electrical resistance tomography. *Inverse Problems*, **18**(6), 1809–1829.
  26. Tamburrino, A., Soleimani, M. (2006) Shape reconstruction in magnetic induction tomography using multifrequency data. *Int. J. of Informaton and Systems Sci.*, **2**(3), 343–353.
  27. Tamburrino, A., Rubinacci, G., Soleimani, M., Lionheart, W. (2003) Non iterative inversion method for electrical resistance, capacitance and inductance tomography. In: *3<sup>rd</sup> World Congress on Industrial Process Tomography*, Banff, Canada, 233–238.
  28. Tamburrino, A., Rubinacci, G. (2006) Fast methods for quantitative eddy-current tomography of conductive materials. *IEEE Transact. on Magnetics*, **42**(8), 2017–2028.
  29. Uchanin, V.N. (2010) Eddy current surface probes: Expanded classification, comparative analysis and characteristic examples of realization. (Review). *Tekh. Diagnost. i Nerazrush. Kontrol*, **4**, 24–29 [in Russian].
  30. Uchanin, V.M. (2007) Specific features of the space distribution of the signal of an eddy-current converter caused by cracks of different lengths. *Materials Sci.*, **43**, 591–595. <http://doi.org/10.1007/s11003-007-0068-2>.
  31. Uchanin, V.M. (2013) *Eddy-current surface probes of double differentiation type*. Lviv, Spolom [in Ukrainian].
  32. Mook, G., Hesse, J., Uchanin, V. (2007) Deep penetrating eddy currents and probes. *Materials Testing*, **49**(5), 258–264. <http://doi.org/10.3139/120.100810>.
  33. Uchanin, V. (2006) Eddy current methods of detection of defects in the zone of rivets of multilayer aircraft structures. *Tekh. Diagnost. i Nerazrush. Kontrol*, **2**, 3–12 [in Russian].
  34. Uchanin, V. (2020) Detection of the fatigue cracks initiated near the rivet holes by eddy current inspection techniques. *Transact. on Aerospace Research*, **1**(258), 47–58. <http://doi.org/10.2478/tar-2020-0010>.

Received 18.03.2021

# XX INTERNATIONAL INDUSTRIAL FORUM - 2021

## INTERNATIONAL TRADE FAIRS

# November 16-19

METAL-WORKING

UKRWELD

HYDRAULICS PNEUMATICS

BEARINGS

UKRUSEC TECH

UKRFOUNDRY

UKRPOWER AUTOMATIZATION

PATTERNS, STANDARDS AND INSTRUMENTS

HOISTING AND TRANSPORTING STOREHOUSE EQUIPMENT

INDUSTRIAL SAFETY

**ORGANIZER:**  
International Exhibition Centre

General Information Partner:  
**ОБОЗНАЧЕННЯ ІНСТРУМЕНТІВ**

Exclusive Media Partner:  
**ЖУРНАЛ ГОЛОВНЕРА ІНЖЕНЕРА**

Technical Partner:  
**RestMedia**

**IEC**  
International Exhibition Centre  
15 Brovarskyi Ave., Kyiv, Ukraine  
“Livoberezhna” underground station  
☎ +38 044 201 11 65, 201 11 56, 201 11 58  
e-mail: alexk@iec-expo.com.ua  
[www.iec-expo.com.ua](http://www.iec-expo.com.ua)  
[www.tech-expo.com.ua](http://www.tech-expo.com.ua)



## INTERVIEW WITH A.I. PANFILOV, PRESIDENT OF APIS HOLDING LLC

Andriy Panfilov, founder of Steel Works LLC, President of APIS HOLDINGS LLC, spoke about the crisis in the industrial sector and company activities during the period of fighting the coronavirus COVID-19 infection.



*Andrii Ivanovich, what steps are you taking now to keep the business afloat?*

Business is stable only, when it is able to adapt quickly, change its processes and models in a significantly variable environment. We also understand that today it will not be as it was yesterday, our market in Ukraine will be falling, and it is difficult to predict by how much — 10–20–30 %. We are taking anticrisis measures, which consist in an abrupt reduction of the expenses, optimization of the organizational structure and increase of operational efficiency.

*What about the team now: working in a regular mode, unpaid leaves or layoff?*

We continue working. In view of the quarantine, the protective measures for personnel have been significantly enhanced. Our main objective is to preserve the core of the team, those staff members, who create the base of our product. We believe that starting from autumn an unfavourable situation formed in all the markets for our industry. That is why we are considerably reducing the expenses, conducting optimization of the organizational structure, which is necessary under the current conditions. But we are not considering a shutdown.

*What losses are incurred by your company because of quarantine? How much has the demand dropped?*

Our main clients are mining and metallurgical works, mines and cement plants. At present we cover practically the entire line of equipment parts, which

are exposed to wear, and we often act as the general contractor — from design to turn-key project delivery.

Now we feel both a drop in demand by 40–50 %, and an unsatisfactory payment discipline, everybody is in the standby mode as regards overhauling and investment projects. We waited for spring, but the new «black swan» introduced even more uncertainties, market outlook is rather value. And few can foresee when it will end in our country. Based on the forecasts, the virus will be active in Ukraine till the summer, and then we assume work in the mode of less stringent quarantine restrictions up to one to two years. We are assessing the losses now.

*How do you manage to keep the sales markets in difficult economic conditions? Which markets are more important for you?*

For us the priority always is the domestic market of Ukraine. At the same time, we are actively developing our positions in the EC countries. The priority export directions are Poland, France, and Germany. We are, primarily, focused on the metallurgical and mining industries. We have extensive experience of development and implementation of solutions as regards addressing the problems of improvement of wear resistance in the enterprises of Ukraine, and know what our foreign clients need and how to achieve it. We are also constantly looking for partners, suppliers of surfacing materials, alternative wear-resistant products for joint projects, both in Ukraine and in the foreign markets.

*What would you recommend as a business manager and owner under the conditions of this quarantine and crisis?*

Despite all that is happening, we have to work and continue planning our activity. We are now forming a strategy for the next 3–5 years, taking new circumstances into account. Our business is conservative, it will not go digital, but we know that it is necessary to improve our work as regards cultivating our relations with clients, rebuilding our business-model to suit their urgent tasks, going ahead of the market in some aspects, creating prerequisites for formation of new trends in our market.

We in our business have been in the market for more than 20 years, and have experienced more than one crisis, but we regard it as the next manifestation, and do not make a disaster of it. We focus on what we can influence, what is in our power to change, what exactly depends on us. And for our part, we try to communicate this philosophy to our partners.